THE FORMATION OF MOLECULAR CLOUDS IN SPIRAL GALAXIES

Clare Louise Dobbs

A Thesis Submitted for the Degree of PhD
at the
University of St Andrews

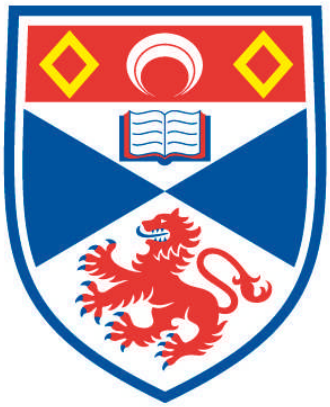

2007

The Formation of Molecular Clouds in Spiral Galaxies

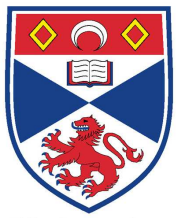

Clare Louise Dobbs

University of St Andrews

Submitted for the degree of Ph.D.

February 15, 2007

DECLARATION

I, Clare Louise Dobbs, hereby certify that this thesis, which is approximately 45,000 words in length, has been written by me, that it is the record of work carried out by me and that it has not been submitted in any previous application for a higher degree.

February 15, 2007

I was admitted as a research student in October 2003 and as a candidate for the degree of PhD in October 2003; the higher study for which this is a record was carried out in the University of St Andrews between 2003 and 2006.

February 15, 2007

In submitting this thesis to the University of St Andrews I understand that I am giving permission for it to be made available for use in accordance with the regulations of the University Library for the time being in force, subject to any copyright vested in the work not being affected thereby. I also understand that the title and abstract will be published, and that a copy of the work may be made and supplied to any bona fide library or research worker, that my thesis will be electronically accessible for personal or research use, and that the library has the right to migrate my thesis into new electronic forms as required to ensure continued access to the thesis. I have obtained any third-party copyright permissions that may be required in order to allow such access and migration.

February 15, 2007

I hereby certify that the candidate has fulfilled the conditions of the Resolution and Regulations appropriate for the degree of Ph.D. in the University of St Andrews and that the candidate is qualified to submit this thesis in application for that degree.

February 15, 2007

THE UNIVERSITY OF ST. ANDREWS

Clare Louise Dobbs

Submitted for the degree of Ph.D.

February 15, 2007

University of St Andrews

ABSTRACT

Molecular clouds are imperative to astronomy as the sites of all known star formation. The problem of how molecular clouds are formed in spiral galaxies is approached numerically, by modelling the response of a gas disk to a spiral potential. The importance of spiral shocks is highlighted as a dominant formation mechanism for molecular clouds in grand design galaxies, where a strong density wave is present. The spiral shock both increases the density of the interstellar gas significantly, and produces structure in the spiral arms. The gas evolves into discrete clumps, which are shown to contain substantial densities of molecular hydrogen, and are therefore identified as molecular clouds. The formation of these clouds requires that the interstellar medium (ISM) is cold and inhomogeneous. The passage of an inhomogeneous gas distribution through a spiral potential further shows that supersonic velocities are induced as the gas shocks. This can explain the velocity dispersion relation observed in molecular clouds. Finally, the shearing of clumps of gas in the spiral arms leads to the formation of inter-arm structures, which are commonly observed in spiral galaxies.

THE UNIVERSITY OF ST. ANDREWS

Submitted for the degree of Ph.D.

February 15, 2007

ABSTRACT

ACKNOWLEDGMENTS

My thanks go mostly to my supervisor, Ian Bonnell. His help over the last 3 years, remarkable enthusiasm and constant encouragement have been invaluable. I would also like to thank Jim Pringle, who collaborated on some of this work, and clarified much of the discussion of the dynamics in Chapter 4. I further acknowledge UKAFF (UK Astrophysical Fluids Facility) for granting me large amounts of computer time to run many of these simulations.

I have enjoyed getting to know all those I've shared an office with, in particular Paul Clark, who introduced me to SPH, clump-finding algorithms, and whose 'endless questions and ranting' have been missed over the last few months.

"Sure it's beautiful, but I can't help thinking about all that interstellar dust out there."

ScienceCartoonsPlus.com

CONTENTS

CHAPTER 1

Introduction

1.1 Overview

The problem of molecular cloud formation has been central to research in star formation and the interstellar medium (ISM) for the last 30 years or so. The benefits of studying molecular cloud formation are fundamental to both. Any theory of star formation depends on the physical properties of molecular clouds. Consequently the outcome from theoretical or numerical results, such as the initial mass function, is related to the initial conditions assumed. The ideal way to investigate star formation, in particular with numerical simulations, is thus to explicitly include molecular cloud formation and continue calculations to star forming scales. Then both the properties of molecular clouds, and their influence on star formation, can be monitored as the clouds evolve. Understanding molecular cloud formation will also provide a clearer indication of the nature and physics of the ISM. Is gas in the ISM on the verge of forming molecular clouds spontaneously or are triggering events usually required? This will depend on the dominant physics e.g. gravity, turbulence, spiral shocks, feedback, which governs molecular cloud formation. Does a significant fraction of the ISM need to be cold HI or even pre-existing molecular gas for molecular cloud formation to occur? Finally, the process(es) of molecular cloud formation could also explain the spiral structure of galaxies, most clearly identified by the youngest star forming regions. What is the relation between spiral structure and molecular clouds? Does spiral structure decide the location of molecular clouds, or does self regulating star formation produce spiral structure?

Some recent attempts have been made to accommodate the ISM, star formation and spiral structure into a self consistent theory (Elmegreen, 2002; Krumholz & McKee, 2005). Turbulence and self gravity are prevalent in current ideas, following the leading theoretical work of the last 2 or 3 decades by Elmegreen and others, and the results of numerical simulations of interstellar turbulence (Elmegreen & Scalo, 2004). These theories aim to predict the star formation rate from the large scale properties of the galaxy, in particular to find a theoretical explanation for the observed Kennicutt (Kennicutt, 1989) law

$$SFR \propto \Sigma^{\alpha} \tag{1.1}$$

where Σ is the average surface density. According to recent observations, this relation arises through dependence of the star formation rate on the local molecular gas surface density (Wong & Blitz, 2002; Heyer et al., 2004). From a theoretical approach, the form

of Equation 1.1 depends on the molecular cloud properties which determine how much of the ISM will be unstable to star formation.

Observationally, molecular clouds were first detected in the early 1970s (e.g. Solomon et al. 1972; Scoville & Solomon 1973) and surveys since the 1980s have analysed their properties and distribution in the Galaxy. Until recently, there has been little numerical work on molecular cloud formation, largely because of the computational requirements and complex chemistry involved. Numerical studies have predominantly focused on star formation, following the evolution of a molecular cloud (e.g. Bate 1998; Stone et al. 1998; Klessen & Burkert 2001; Bate et al. 2003; Dobbs et al. 2005). Some authors are now taking a step back and modelling the condensation of molecular clouds (Glover & Mac Low, 2006b) or cold HI regions (Audit & Hennebelle, 2005; Heitsch et al., 2005) in turbulent gas. Accurately simulating molecular cloud formation on galactic scales is still some way off. However this thesis makes one of the first attempts to model this problem. Hydrodynamical simulations of a galactic disk are described, which reveal the formation of dense clouds in the ISM. A criterion based on the chemistry of interstellar shocks is applied to show when they will contain molecular gas.

The rest of the introduction provides a brief summary of the properties and environment of the ISM before concentrating on molecular clouds. The main results from observational surveys and theories regarding molecular clouds are discussed.

1.2 The Interstellar Medium

The interstellar medium consists predominantly of neutral atomic (HI), molecular (H_2) and ionized (HII) hydrogen. In our own Galaxy, approximately 70% of the ISM is hydrogen, 1% dust and the rest mostly helium. Overall the ISM is thought to contain 1/10 of the total mass present in stars and gas. Galaxies can contain varying degrees of molecular gas - with substantial HI and very little H_2, or vice versa. For radii between 1.7 kpc and 8.5 kpc in the Galaxy, the mass of HI is $1 - 1.5 \times 10^9$ $M_\odot$ (Dame, 1993; Wolfire et al., 2003) and the mass of H_2 is 6×10^8 $M_\odot$ (Bronfman et al., 2000). Figure 1.1 shows the variation in the HI and H_2 (azimuthally averaged) surface density with radius for the Galaxy (Wolfire et al., 2003), which is qualitatively typical of spiral galaxies. Though not included in Figure 1.1, nearly all of the gas in the centre of spiral galaxies is molecular. With increasing radius, the H_2 surface density decreases exponentially, although Heyer et al. (1998) find that there is a sharp cut-off beyond the Perseus arm (at galocentric radii $\gtrsim 12$ kpc). There is some controversy as to whether undetected H_2 lies in the outer regions of galaxies (Allen, 2004), in which case there may be a substantial amount of H_2 which is not currently observed. The density of dust, on which the formation of H_2 is dependent (Chapter 6), is largely proportional to the total gas density.

The components of the ISM span a wide range of temperatures and densities, but the distribution of atomic hydrogen is usually described by a 3 phase medium, following the model of McKee & Ostriker (1977). The different components have temperatures of approximately $T = 100$ K (the cold neutral medium (CNM)), $T = 10^4$ K (the warm neutral medium (WNM) or warm ionized medium (WIM)), and $T = 10^6$ K (hot ionized medium (HIM)). The phases coexist in pressure equilibrium, regulated by photoelectric,

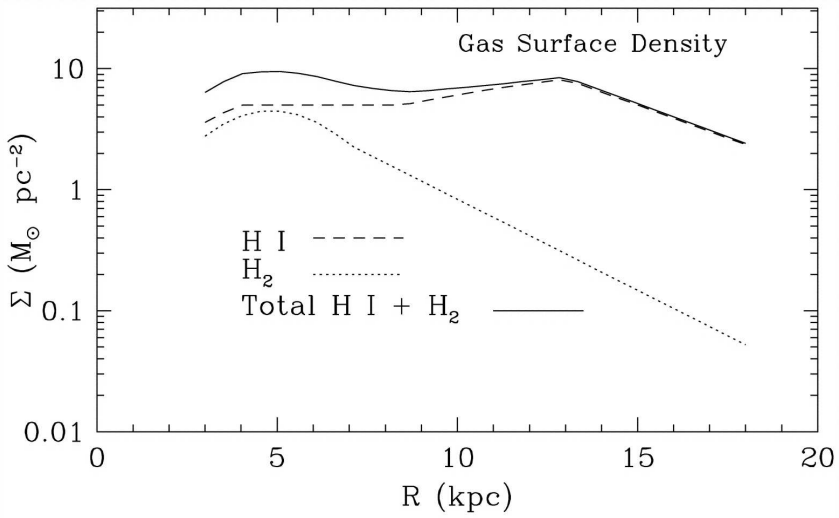

Figure 1.1: The surface column density of HI, H_2 and total HI + H_2 are shown for the Galaxy (Wolfire et. al., 2003). For comparison, the surface density of HII at 8.5 kpc is 0.3 $M_\odot$ pc^{-2}.

cosmic ray and photoionization heating and collisional cooling with metals such as CII, OI and CI. Presumably gas outside these regimes is undergoing a transition from one phase to another, or is the result of dynamical interaction between different phases. Simulations of the ISM suggest up to 1/3 of the gas is in the unstable regime between the CNM and WNM (Piontek & Ostriker, 2005; Audit & Hennebelle, 2005). Supernovae eject the hot diffuse gas into the ISM, which fills large regions between the colder clouds. The amount of gas present in each component is not easy to determine observationally, however estimates of the filling factors, densities and scale heights are shown in Table 1.1 using the values in Cox (2005) (the WNM was split into 2 different density components). The last column is a simple estimate of the percentage by mass of each component. As the filling factors only add up to 0.46, there appears to be considerable 'empty space', possibly permeated by an even more diffuse, hotter component of gas (Cox, 2005). The cold HI contains most of the mass but occupies a very small fraction of the volume. At present, this gas is the most likely precursor to molecular clouds, which, located within CNM clouds, have an even smaller filling factor.

In the McKee & Ostriker (1977) model, the hot diffuse gas pervades much of the galactic disk, embedded with cold clouds. However, in addition the ISM contains many remarkable structures such as supershells, cavities and tunnels, of which some may be linked to supernova remnants or OB associations, whilst others remain unexplained. The ISM is now recognised as highly turbulent (Elmegreen & Scalo, 2004) since average velocity dispersions in the gas exceed the thermal sound speeds (Boulares & Cox, 1990). These two observations have lead to an alternative view that the distribution of the ISM is essentially fractal in nature (Elmegreen, 1997).

Molecular clouds are the coldest, most dense regions of the ISM. The typical density of molecular clouds is $100 - 10^5$ cm^{-3} and their temperature is usually 10-20 K, although locally regions may be much denser or hotter. They are distinct in the ISM, and integral to astronomy, as the regions in which all known star formation occurs. Stars form in

Component	Scale height (pc)	Density (cm^{-3})	Filling Factor	Estimated % of ISM by mass
CNM	120	30	0.013	58
WNM (a)	300	1	0.194	29
WNM (b)	400	0.36	0.174	9
HIM	1000	0.3	0.083	3

Table 1.1: Table showing properties in relation to the distribution of the different components of atomic hydrogen in the ISM. The scale heights, densities and filling factors are taken from Cox (2005).

dense cores embedded in the molecular clouds, usually of order 1 pc or less in size and containing several $M_\odot$ or more. The vast majority of star formation takes place in Giant Molecular Clouds[1] (GMCs), of mass $> 10^4$ $M_\odot$ (Blitz & Williams, 1999). The range of observed masses of molecular clouds nevertheless extends from < 10 $M_\odot$ to 10^7 $M_\odot$, with sizes of < 1 pc (Heyer et al., 2001) to 100 pc or more (Dame et al., 1986). As sites of star formation though, GMCs are considered of most relevance. The majority of GMC's are thought to contain star formation; the cloud G216-2.5 is one of the only GMCs that have been observed locally without star formation (Maddalena & Thaddeus, 1985).

1.3 Molecular clouds: Observations

1.3.1 Tracers of molecular gas and HISA

The H_2 molecule, of which molecular clouds predominantly consist, is extremely stable, and cannot be detected directly in a cold molecular cloud. Over 100 more complex molecules have been detected in the ISM, formed on dust grains in a similar way to H_2, but with much lower abundances. These include HCN, SiO, C_2, H_20 and CS, but most observations measure CO (J=1-0) emission, since ^{12}CO is easily excited and the most abundant of molecules after H_2. Other molecular tracers are sometimes used to study the denser regions and internal structure of molecular clouds where ^{12}CO becomes optically thick e.g. CS observations to trace parsec-scale molecular cloud structure (Greaves & Williams, 1994), or HCN to detect starless cores (Yun et al., 1999). The estimated abundance of the tracer molecule is usually used to determine a conversion factor between the integrated luminosity and the H_2 column density.

^{12}CO has been used most extensively for observations of molecular clouds, although it is now argued that ^{12}CO may not accurately trace H_2. ^{12}CO is in fact so abundant that the densest cloud cores become saturated in ^{12}CO emission (Lada et al., 2006). Consequently, calculations of the mass of molecular clouds with the assumption of a constant H_2 to CO conversion factor may be inaccurate. The most recent surveys e.g. the FCRAO Galactic Ring Survey (Jackson et al., 2006), have instead used the ^{13}CO isotope, which is believed to be a better tracer of the H_2 column density, but an analysis of molecular

[1]There is no actual definition of a GMC, but the convention used in this thesis is that GMCs have a mass of H_2 greater than $> 10^4$ $M_\odot$. 'Molecular clouds' may have lower masses.

clouds from these surveys is not available yet. There are also concerns that CO may not trace H_2 in low density regions. Allen & Lequeux (1993) examine dust clouds in M31 away from ongoing star formation. These clouds emit faint CO, but are expected to have masses of 10^7 $M_\odot$. They conclude that the molecular gas is too cold to be able to detect higher levels of CO emission, and further suggest cold molecular gas is abundant in the outer regions of the Galaxy (Lequeux et al., 1993). High latitude molecular clouds are found in the Galaxy without CO emission (eg. Blitz et al. (1990)), but these tend to be lower mass (10 $M_\odot$) diffuse clouds.

The main observational technique with which to compare molecular emission is dust extinction mapping. The extinction can be measured from star counts, by comparing the number of stars in a region of a molecular cloud to those in an unobscured part of the sky, below a certain magnitude threshold (e.g. Bok 1956; Encrenaz et al. 1975; Dickman 1978a; Lada et al. 1994). More recently the extinction has been measured from near IR color excess, the change in color of background stars due to extinction. The column density is assumed proportional to the extinction, so density profiles of molecular cloud cores can be found (Alves et al., 2001, 1998). This process is now starting to be applied to Galactic and extragalactic molecular clouds (Lada et al., 2006). HI can also be used to compare the densities of molecular clouds determined from CO observations. Photodissociation regions (PDRs) lie on the edge of molecular clouds where molecular gas is being converted to atomic gas by photodissociation from young stars. By equating the photodissociation rate with the formation rate of molecular hydrogen, the overall density of atomic and molecular gas can be ascertained (Allen et al., 2004).

The observations of HISA (HI self absorption) clouds of cold atomic hydrogen are likely to be very relevant for future studies of molecular cloud formation. The HISA clouds are denser and colder than usual for atomic hydrogen in the ISM, suggesting they may represent a transition from atomic to molecular gas (Klaassen et al., 2005; Kavars et al., 2005; Gibson et al., 2005). These features are revealed when cold (< 100 K) atomic hydrogen is situated in front of a background HI medium ($100 - 150$ K) and dips are observed in the HI emission. The difficulty lies in distinguishing real features from changes in the background emission, as well as requiring the geometry that both the HISA and the background emission lie along the line of sight. The Canadian Galactic Plane Survey (Taylor et al., 2003) has provided mapping of HISA in the Perseus arm (Gibson et al., 2000, 2005) and 70 HISA complexes have been analysed in the Southern Galactic Plane (Kavars et al., 2005). Some, but not all of the HISA clouds are also associated with CO emission and therefore molecular hydrogen, although again a significant fraction of the gas may be molecular without producing CO emission (Klaassen et al., 2005).

1.3.2 Molecular cloud surveys in the Milky Way

The main large-scale CO surveys of the Galaxy include the Massachusetts-Stony Brook CO Galactic Plane Survey (Solomon et al., 1985), Columbia CO survey (Cohen et al., 1986), the FCRAO Outer Galaxy Survey (Heyer et al., 1998) and Bell Laboratories ^{13}CO Survey (Lee et al., 2001), indicated on Figure 1.2. The FCRAO Survey (Figure 1.3) provides the most complete sample of molecular clouds, with 10,156 objects and masses as low as 10 $M_\odot$. The Columbia CO survey mapped all 4 quadrants, but only with sufficient resolution

to map the most massive clouds ($> 10^5$ $M_\odot$). Collaborators have since mapped the entire Galaxy in CO (Dame et al., 2001).

The CO emission is measured by the antenna radiation temperature, T_R^*, recorded in 3 dimensional coordinates (l, b, v_{lsr}), the galactic longitude (l), galactic latitude (b) and velocity with respect to the local standard of rest (v_{lsr}). Molecular clouds are identified as topologically closed surfaces above a threshold temperature, T_R^*. Whilst the coordinates (l, b) determine the direction of the molecular cloud, the distance to the cloud is measured using l and v_{lsr}. The distance is usually calculated assuming a flat rotation curve. The cloud is assumed to be at a distance along the line of sight where the observed v_{lsr} is the same as the v_{lsr} from the rotation curve. As discussed in Chapter 4, velocities depart significantly from circular rotation in the spiral arms due to spiral shocks. Including a modified rotation curve can give significantly different distance measurements (Kothes et al., 2003).

Assuming circular velocities, for a line of sight outside the solar circle, there is one possible distance for observed coordinates (l, b, v_{lsr}), whilst within the solar circle, their are 2 possible solutions. Other information, such as the proximity to HII regions or the size of the cloud are then necessary to determine the most likely distance for clouds in the inner regions of the Galaxy (Dame et al., 1986). For a line of sight roughly tangent to the solar circle, e.g. along the Sagittarius arm, the v_{lsr} of the clouds are likely to be similar, leading to velocity crowding. Consequently larger values of T_R^*, $\sim 3-4$ K are necessary to identify features from the background emission for the inner Galaxy and only larger molecular clouds (e.g. $> 10^3$ $M_\odot$ (Lee et al., 2001) or $> 10^4$ $M_\odot$ (Solomon & Rivolo, 1989)) can be detected. The FCRAO survey on the other hand maps a region beyond the solar circle so velocity crowding does not occur (asuming circular velocities). With $T_R^* = 1.4$ K (Heyer et al., 1998), clouds as low as 10 $M_\odot$ can be detected. However there are fewer high mass clouds towards the Outer Galaxy where there is much less molecular gas, the largest in their survey $\sim 2 \times 10^5$ $M_\odot$.

The mass can be calculated from the CO luminosity, by

$$M_{CO} = \frac{\mu X S D^2}{M_\odot} \tag{1.2}$$

with M_{CO} in solar masses, μ the mean molecular weight, S the apparent CO luminosity (integrated over velocity and solid angle) in K km s $^{-1}$ sr and D the distance to the cloud in cm. X is the conversion factor to determine the column density of H_2 from the CO luminosity $N(H_2)/W(CO) \sim 2 \times 10^{20}$ cm^{-2} K^{-1} km^{-1} s. An average value of X has been calculated from various techniques; star counts (Dickman, 1978b), color excess (Lombardi et al., 2006), radiative transfer models (Plambeck & Williams, 1979) and γ rays (Bloemen et al., 1984; Strong et al., 1988). However the underdetection of CO at both low densities, where CO is dissociated more readily than H_2, and in high density cores, where ^{12}CO is saturated, suggests that X will vary in different environments. PDR models find X varies over orders of magnitude for different column densities, UV field strengths and metallicities (Kaufman et al., 1999; van Dishoeck & Black, 1988). A comparison of CO observations with other techniques will provide better estimates of cloud masses, e.g. Lombardi et al. (2006) find the mass of the Pipe nebula approximately 1.5 times higher from color excess measurements than from CO emission. The size scale of the clouds may be calculated by an effective radius $r_e = (Area/\pi)^{1/2}$ (Heyer et al., 2001) or from the dispersion in

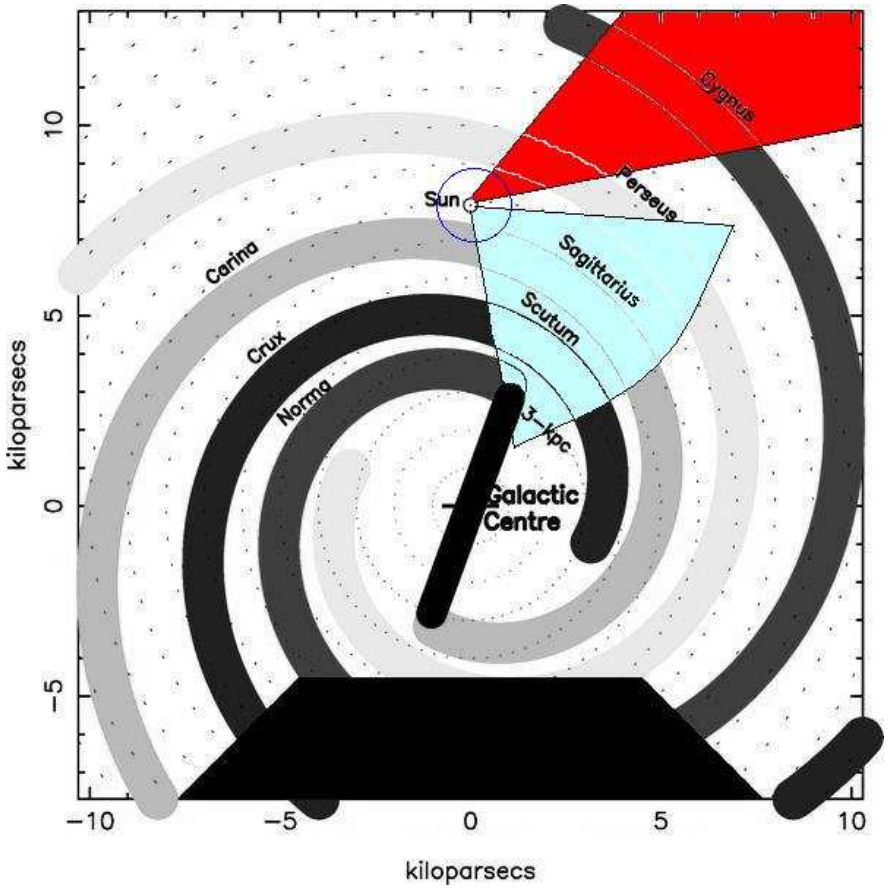

Figure 1.2: The main spiral arms in the Galaxy, as mapped by Vallee (2005). The range of 2 molecular cloud surveys are shown, the Massachusetts-Stony Brook survey (blue) and the FCRAO outer galaxy survey (red). The Bell Labs CO Survey also maps the first quadrant. The circle shows a 1 kpc ring which contains the Orion, Moneceros, Ophiculus, the Coalsack, Taurus, Chamaeleon, Lupus and Perseus clouds selected for most studies of molecular clouds and star formation. These are generally located in the Orion arm, a shorter section of spiral arm in which the Sun is located. There is some uncertainty in the distances to the spiral arms, and the black trapezium represents a section of the Galaxy where the structure is unknown.

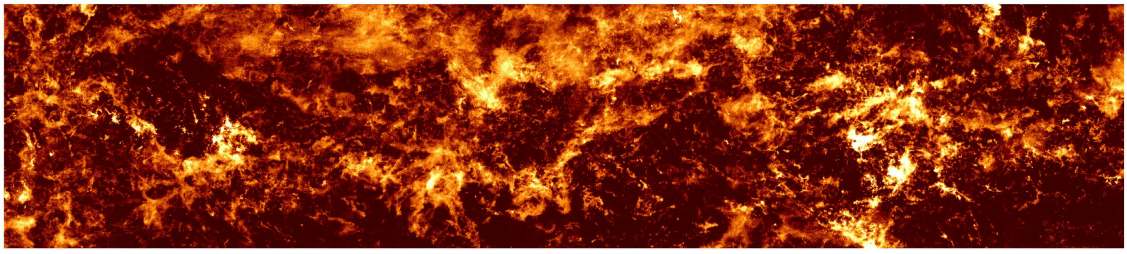

Figure 1.3: ^{12}CO emission from the FCRAO Outer Galaxy Survey (Heyer et. al., 1998).

the cloud coordinates (Solomon et al., 1985). Principal component analysis (PCA) has also been used, which extracts more spatial and velocity information from the complex structure of molecular clouds (Heyer & Schloerb, 1997).

Bearing in mind the uncertainties in detemining molecular cloud data, and the different techniques applied by observers, these surveys have revealed similar properties of molecular clouds. The rest of this section provides an overview of the distribution and main features of molecular clouds.

Since spiral arms are generally defined by the presence of star formation, molecular clouds are expected to be located in the spiral arms of a galaxy. There are 2 notable differences apparent in the distribution of molecular clouds in relation to the spiral structure: 1. The GMCs appear more concentrated in the spiral arms than smaller clouds; 2. Clouds in the Outer Galaxy are more concentrated in the spiral arms. Dame et al. (1986) detect GMCs of masses $> 5 \times 10^5$ $M_\odot$, which clearly trace the Sagittarius arm. The GMCs appear more randomly distributed towards the inner Scutum and 4 kpc spiral arms, although there are few objects in their survey. Stark & Lee (2006) compare the distance of clouds of $> 10^5$ $M_\odot$ and $< 10^5$ $M_\odot$ from the spiral arms, showing that the smaller clouds are systematically less confined to the spiral arms. The arm-interarm ratios of molecular clouds vary from 5:1 in the Inner Galaxy (Solomon & Rivolo, 1989) to 13:1 towards the Carina arm (Grabelsky et al., 1987) and over 25:1 towards the W3, W4, W5 complex (Digel et al., 1996; Heyer & Terebey, 1998). The strong concentration of molecular clouds to the spiral arms in the Outer Galaxy may be related to the decrease in the fraction of molecular gas with radius.

Two major characteristics of molecular clouds are the velocity dispersion relation and the mass power spectrum. These properties appear remarkably consistent from the different surveys, as well as for external molecular clouds (Section 1.3.3). The velocity dispersion varies with the size of the molecular cloud according to $\sigma \propto r^{0.5}$ for the Inner Galaxy clouds (Dame et al., 1986; Solomon et al., 1987), and is observed for clouds down to sizes of 10 pc (below which the velocity dispersion is approximately constant with size) in the FCRAO survey (Heyer et al., 2001). The velocity dispersion size-scale relation for the clouds observed by Solomon et al. (1985) is plotted in Figure 1.4. This relation is also observed over size-scales down to < 0.1 pc within individual molecular clouds (e.g. Larson (1981); Myers (1983)). The consistency of this law over many scales (Heyer & Brunt, 2004), and comparison with the relation $\sigma \propto L^{1/3}$ for Kolmorogov turbulence, has prompted the view that the molecular clouds are turbulent (Larson, 1981).

The mass power spectra $dN/dM \propto M^\gamma$ is also similar for molecular clouds in the Milky Way, with γ in the range 1.5-1.8 (Solomon et al., 1987; Heyer et al., 1998). The steepness of the power law indicates that the bulk of the molecular gas lies in the larger GMCs. Again the consistency of this law down to smaller scales has implied that the formation of molecular clouds may be hierarchical or fractal in nature. Further discussion of the internal structure and dynamics of molecular clouds is included in Chapter 3.

The virial mass, M_{vir}, of the molecular clouds can also be calculated from their velocity dispersion (Solomon et al., 1987; Grabelsky et al., 1988; Heyer et al., 2001). These surveys have generally inferred that since the gravitational parameter, $\alpha_G = M_{vir}/M_{CO}$ is approximately 1, the molecular clouds are in virial equilibrium. The exception is the

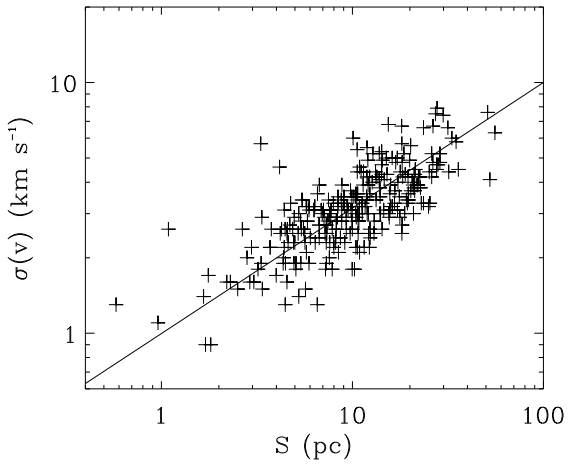

Figure 1.4: The velocity dispersion is plotted as a function of size scale, using data for 273 molecular clouds from Solomon et. al., 1987. The fitted line shows the relation $\sigma(v) = S^{0.5}$ km s^{-1}.

Outer Galaxy survey clouds of $< 10^3$ M$_\odot$, where $M_{vir} >> M_{CO}$. However, molecular clouds are becoming increasingly viewed as turbulent transient features which, with feedback from young stars, are far from equilibrium (Section 1.4.1). Computer simulations of cloud collapse show that the gravitational, kinetic, magnetic and thermal energies may be similar although the cloud itself is not in equilibrium (Ballesteros-Paredes & Vazquez-Semadeni, 1995). A GMC may even be unbound overall, with star formation occurring in gravitationally bound clumps within the cloud (Williams et al., 1995; Ballesteros-Paredes, 2004; Clark & Bonnell, 2004).

1.3.3 CO observations in external galaxies

Data sets of molecular clouds are now available for several galaxies in the local group, including the spirals M31 and M33. Further CO measurements indicate the distribution of molecular gas in M51, M81 and M83, and several of the largest GMCs can be resolved. External GMCs are much easier to distinguish spatially than in the Galaxy, where molecular clouds are observed only in the Galactic plane. Although only a small number of molecular clouds have been resolved in external galaxies, and only the largest molecular clouds can be observed, the first comparative studies are starting to be made (Blitz et al., 2006).

A comparison of GMC properties in different galaxies shows that generally the GMCs show more similarities than differences. The $\sigma \propto L^{0.5}$ velocity dispersion law appears to be consistent for M31, M33 and the Magellanic Clouds (Blitz et al., 2006), although the constant (corresponding to the magnitude of the velocities) is required to vary by a factor of 2. In M81 the velocity dispersions for GMCs are lower than would be expected in the Galaxy (Brouillet et al., 1998), although there are very few objects for a useful comparison. Further comparisons of the luminosity versus line width show good agreement with the Milky Way (Blitz et al., 2006). The properties of molecular clouds in

the Magellanic Clouds appear to be similar to M31, M33 and the Milky Way, although they are very different types of galaxies. The mass spectra of GMCs are very similar in the Milky Way, M31 and the Magellanic Clouds, with γ in the range if 1.5 to 1.8 (Blitz et al., 2006). There is some evidence for variation though, as M33 has a steeper mass spectrum of $\gamma \sim 2.5$ (Engargiola et al., 2003), and from dust extinction measurements, $\gamma \sim 2.3$ for NGC5128 (Lada et al., 2006).

M51, the Whirlpool Galaxy, is probably the most studied of external spiral galaxies. M51 is a grand design galaxy with a high molecular gas content, well defined spiral arms and a strong density wave. Approximately 85% of the total mass is found to lie in the spiral arms (Aalto et al., 1999), and at least 75% of the total gas mass is molecular (Garcia-Burillo et al., 1993). The molecular emission in M51 shows density wave streaming motions (Chapter 4) and is coincident with dust lanes associated with a spiral shock (Vogel et al., 1988). This strongly suggests that the density waves trigger the formation of GMCs from pre-existing molecular gas (since there is no time delay between the shock and the formation of H_2), and subsequently the formation of stars. The Hα emission, a product of recent star formation, is generally observed downstream from the molecular gas (Vogel et al. (1988) estimate an offset of 300pc), implying a time delay between the formation of GMCs and the formation of stars. GMCs are observed in M51 with masses of well over 10^7 $M_\odot$, although the largest GMCs, are often termed GMAs (Giant Molecular Associations) as these may consist of several smaller GMCs. Rand & Kulkarni (1990) identify 26 GMAs in M51, of which 20 lie on the arms - though there is a good possibility that interarm GMAs may be associated with spurs (Aalto et al., 1999) connected with the spiral arms (Chapter 4). The atomic hydrogen, which is observed to trace the spiral arms downstream from the molecular gas, may be present in the ISM entirely as a by-product of photodissociation (Tilanus & Allen, 1989).

The galaxy M33 shows very different behaviour. As little as 2% of the total gas mass in M33 is molecular, and there are no GMCs of mass $> 5 \times 10^5$ $M_\odot$ (Engargiola et al., 2003). The lack of larger clouds leads to a steeper mass spectra than observed in the Galaxy. The GMCs are observed to lie on filaments of dense HI, which mainly trace irregularly shaped spiral arms (Figure 1.5). Interestingly, approximately 1/4 of GMCs in M33 do not contain active star formation (Engargiola et al., 2003), a fraction which appears large when compared with molecular clouds in the local vicinity.

M83, M81, M31 and the Milky Way appear to lie in between these two different cases, in terms of molecular gas content, mass of GMCs and spiral arm pattern. There is evidence in M83 of CO emission coincident with the dust lanes whilst the HI may be photodissociated downstream in a similar scenario to M51 (Tilanus & Allen, 1993). CO emission associated downstream from the dust lanes in M81 (Brouillet et al., 1991) instead suggests that the preshock material is more likely to be atomic hydrogen which assembles into GMCs after passing the shock (Tilanus & Allen, 1993). More observations from a larger sample of galaxies will be essential for explaining molecular formation in different environments. Using dust extinction mapping in conjunction with CO observations may also assist future progress.

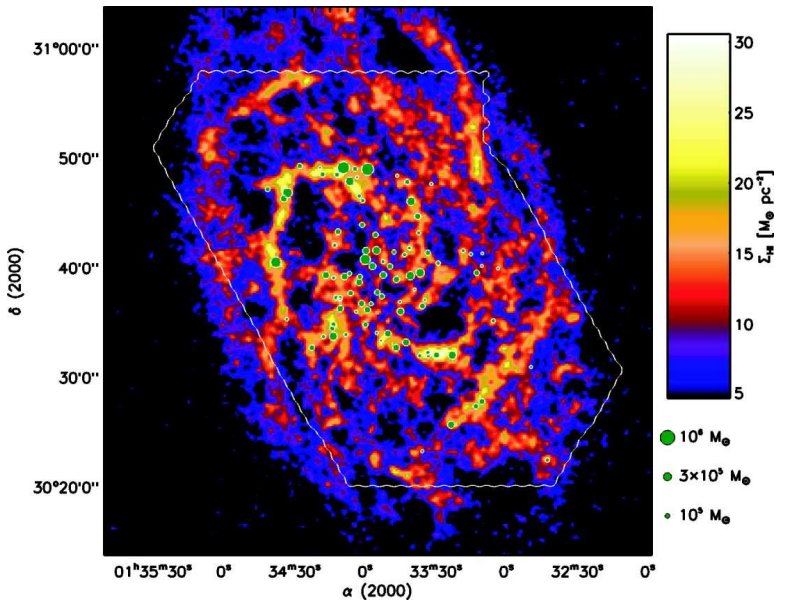

Figure 1.5: Colour image of H I 21 cm emission in M33 from Deul & van der Hulst (1987) with molecular clouds from Engargiola et. al., 2003. The areas of the molecular clouds have been scaled to represent the relative masses of the clouds. This image is taken from Engargiola et. al., 2003

1.4 Molecular clouds: Theories

The formation of GMCs can occur in essentially 3 different ways (see also reviews in Elmegreen (1990, 1996) and references therein):

- Agglomeration of smaller cloudlets through random collisions

The collisional model was first proposed by Oort (1954), and a theoretical analysis followed in Field (1965). GMCs are conceived to form through the agglomeration of smaller clouds, which are in hydrodynamical equilibrium in the ISM. The clouds are more dense than the ambient ISM and therefore collisions between them are regarded as ballistic. Assuming that clouds are most likely to coalesce as a result of a collision, the mass spectrum of the clouds is $dn/dM \propto M^{-1.5}$ in equilibrium (Field & Saslaw, 1965; Field & Hutchins, 1968; Taff & Savedoff, 1972; Handbury et al., 1977), similar to observations. The long lifetime determined for these clouds (Scoville & Hersh, 1979; Kwan, 1979) corresponded with the supposed longevity of molecular clouds from observational results at the time (Section 1.4.1).

One of the main problems that has become apparent with this model is that collisions are likely to result in fragmentation rather than coalescence, especially with the large velocity dispersions expected for molecular clouds. Hausman (1982) found a steeper mass spectrum when allowing for fragmentation and the likely outcome from the collision of 2 clouds appears to be fragmentation (Lattanzio et al., 1985; Kimura & Tosa, 1996; Miniati et al., 1997). Recently, a higher resolution SPH simulation of many interacting clouds (Gittins et al., 2003) showed that significant merging of clouds does not occur, although star formation is induced where the clouds collide (Kimura & Tosa, 1996).

Colliding flows or a spiral shock potentially provide situations where the agglomeration of GMCs from molecular gas could occur (Pringle et al., 2001; Clark & Bonnell, 2006). Rather than random collisions between clumps, the clumps interact more frequently according to a potential or the Mach number of the shock. Cloud collisions subject to shear forces in a gravitational potential are found to produce a mass spectrum more similar to observations (Das & Jog, 1996). Recent simulations (Clark & Bonnell, 2006) also indicate that the mass spectrum of colliding clumpy flows produces a Salpeter type mass spectrum, consistent with star forming clumps, although slightly steeper than currently observed for molecular clouds.

- Instabilities in the ISM: Gravitational, thermal and magnetic

For a thin disk to be gravitationally stable against axisymmetric perturbations requires the Toomre parameter (Toomre, 1964) Q to be > 1. For a gaseous disk,

$$Q_g = \frac{\kappa\sigma}{\pi G\Sigma} \tag{1.3}$$

where κ is the epicyclic frequency, σ is the velocity dispersion and Σ is the surface density. Usually galaxies are found to have $Q_g \sim 1$ (Kennicutt, 1989; Martin & Kennicutt, 2001; Boissier et al., 2003), whilst lower values of Q_g are expected to produce vigorous star formation (Li et al., 2005). There are 2 scenarios for gravitational collapse in spiral galaxies: In one case, transient instabilities in the gas and stars lead to simultaneous star and spiral arm formation (Goldreich & Lynden-Bell, 1965), typical of multi-arm flocculent galaxies. The second is that gas compressed to higher densities behind a spiral shock becomes gravitationally unstable (Elmegreen, 1979; Cowie, 1980, 1981; Balbus & Cowie, 1985; Balbus, 1988; Elmegreen, 1994b). The latter was first proposed by Elmegreen (1979), who considered a magnetic cylinder parallel to a spiral arm. Comparisons with the observed properties of dust lanes behind shocks indicated that such a cylinder would be unstable. Subsequent analysis determined a Toomre-type parameter for a gas disk subject to a spiral potential, inclusive of the density enhancement in the spiral arms (Balbus & Cowie, 1985). The growth of density perturbations occurs in the compressed gas providing $\sigma \leq 7$ km s^{-1}.

The above gravitational instabilities predict the formation of $10^6 - 10^7$ M$_\odot$ complexes, with a regular spacing of 0.5-2 kpc along the spiral arms, assuming a sound speed of several km s^{-1} (Elmegreen, 1979; Balbus & Cowie, 1985; Elmegreen, 1994b). This agrees with the largest clouds observed in galaxies (Elmegreen & Elmegreen, 1983; Garcia-Burillo et al., 1993).The formation of low mass clouds from this model is unclear though. One possibility is to include cooling during cloud collisions, which reduces the sound speed of the gas and thereby length scale of the collapse (Elmegreen, 1989). Many authors also discuss the condensation of 'cold' clouds through thermal instabilities in uniform gravitationally stable gas (e.g. Field 1965; Parravano 1987).

The magnetic Rayleigh-Taylor, or Parker instability (Parker, 1966) has also been cited as a mechanism for molecular cloud formation (Shu, 1974; Woodward, 1978; Blitz & Shu, 1980; Hanawa et al., 1992) predicting cloud masses and separations similar to those given above for the gravitational instability (Mouschovias et al., 1974), but longer formation timescales (Zweibel & Kulsrud, 1975; Elmegreen, 1982). Although likely to facilitate molecular cloud formation, numerical simulations suggest the Parker instability alone is unable to form molecular clouds, and is of secondary importance compared to the

gravitational Jeans instability (Kim et al., 2002, 2001). Theoretical analysis also concludes that gravitational collapse will dominate magnetic pressure in cloud formation (Elmegreen, 1982).

- Forced compression of the ISM by supernovae, turbulence or spiral wave shocks

Observations of bright stars situated on the edge of bubbles or arcs are often associated with the triggering of star formation by supernovae or HII regions (e.g. Oey & Massey 1995; Deharveng et al. 2003; Oey et al. 2005). This star formation is often attributed to the compression of an *existing* molecular cloud by shock waves from ionization fronts from OB stars (Elmegreen & Lada, 1977; Elmegreen, 1998). However giant rings and supershells formed by supernovae, which extend 100 pc or more over a galactic disk, may be able to sweep up atomic gas in the ISM to form a new generation of molecular clouds (McCray & Kafatos, 1987; Tenorio-Tagle & Bodenheimer, 1988; Efremov & Elmegreen, 1998). The massive shells may fragment into clouds by gravitational (McCray & Kafatos, 1987; Elmegreen, 1994a; Whitworth et al., 1994) or thermal (Koyama & Inutsuka, 2000) instabilities. Observations of the region LMC4 support this scenario, where shocks from supernovae appear to be propagating into HI clouds (Dopita et al., 1985; Efremov & Elmegreen, 1998) (it is also suggested that the local clouds have been triggered in a similar manner). The models for spiral structure by Mueller & Arnett (1976) and Gerola & Seiden (1978) (Chapter 4) assume that such self propagating star formation in galaxies is widespread. However the contribution of triggered molecular cloud formation is relatively unknown.

It is also conceivable that turbulent compression in the ISM results in molecular cloud formation (Vazquez-Semadeni et al., 1995; Elmegreen, 1996; Ballesteros-Paredes et al., 1999; Glover & Mac Low, 2006b). Ballesteros-Paredes et al. (1999) advocate Taurus as an example of this mechanism, since there is no evidence of triggering from supernovae, and the HI data indicates that Taurus lies between colliding flows of gas. The advantage with this scenario is that if turbulence regulates the ISM from galactic scales down to molecular cloud cores, the structure should appear self similar for each size scale, in agreement with observations (Elmegreen, 2002; Elmegreen et al., 2003).

Finally, the triggering of star formation by spiral waves follows the model of Roberts (1969) and is described in more detail in Chapter 4. The spiral triggering process is usually coupled with one of the mechanisms above; thermal (Koyama & Inutsuka, 2000) and/or Parker instabilities lead to fragmentation in the compressed gas forming clouds, whilst spiral shocks may lead to enhanced interactions between clouds (Roberts & Hausman, 1984; Scoville et al., 1986; Cowie, 1980). Star formation by spiral arm triggering has recently been modelled by Bonnell et al. (2006). These simulations show that spiral shocks can also explain the turbulent motions that are observed in GMCs, which are induced by the spiral shock on all scales simultaneously.

It is apparent from the discussion above, that a combination of processes may be involved for the formation of a single cloud. The task facing astronomers is to evaluate which processes are the most relevant, and how they determine the morphology and properties of the resulting molecular clouds. From the observations described in Section 1.3.3, it also seems probable that the formation process varies in different environments. Where

the content of molecular gas is high, e.g. M51 or the centres of galaxies, GMCs could form through the agglomeration of pre-existing molecular clouds. In this scenario, the ISM may be predominantly molecular (or cold HI), but GMCs are only observed where the gas has coalesced into larger structures heated by star formation (Pringle et al., 2001). However this is unlikely to occur in the outskirts of galaxies or for example, M33, where little molecular gas is thought to exist aside from GMCs (Engargiola et al., 2003). Then other processes, most commonly gravitational/magnetic instabilities or compression from shocks (Shu et al., 1972; Aannestad, 1973; Hollenbach & McKee, 1979; Koyama & Inutsuka, 2000; Bergin et al., 2004) must be required to convert atomic to molecular gas. An alternative view is that the formation process is unique, and the molecular content of the gas is determined by the pressure of the ISM (Blitz & Rosolowsky, 2004).

1.4.1 Lifetimes of molecular clouds

It was previously believed that the lifetimes of GMCs were relatively long, of the order 100 Myr. This was based on early observations of CO which did not show any spiral structure, implying that molecular clouds must last for at least the interarm crossing time. Furthermore the star formation rate appears too low compared with the Galactic mass of H_2 unless the formation timescale is sufficiently long (Zuckerman & Evans, 1974). However recent observations have implied that the onset of star formation is much more rapid, occurring over a dynamical timescale of the cloud (Elmegreen, 2000; Hartmann et al., 2001). Elmegreen notes that the distribution of stars appears to be 'frozen out' in the gas, resembling a hierarchical system of clusters embedded within the cloud, and preserving the turbulent conditions of the gas in which star formation takes place. The spread of ages in the stellar cluster is small, of order a dynamical time, and the separation of the clusters correspondingly small, and finally, as noted in the introduction, the fraction of clouds without star formation is very low. Then the total lifetime of a GMC, including disruption, is $\sim 3 \times 10^7$ yr (Elmegreen, 2000; Pringle et al., 2001). In this hypothesis, the low galactic star formation rate is explained by the low star forming efficiency, with only a small fraction gas in a molecular cloud undergoing collapse at any particular time, due to the highly structured, turbulent nature of molecular clouds.

The consequences of a shorter molecular cloud lifetime have been expanded by Pringle et al. (2001). They analyse shock formation of H_2 and find that in order for such rapid formation of molecular clouds to occur, the pre-shock gas must be relatively dense, $\sim 10^2$ cm^{-3}. This is sufficiently dense that the pre-shock gas will already be predominantly molecular. Consequently they propose that molecular clouds form by the agglomeration of dense gas in the ISM, of which much is already molecular. Another implication of a short cloud lifetime is that a continued injection of turbulence is no longer required in molecular clouds, since the decay time of the turbulence is comparable to the cloud lifetime (Bonnell et al., 2006). Thirdly, there is no longer any requirement that the clouds are in virial equilibrium, since they are not in a steady state. This then explains the low star formation efficiency, since most of the molecular cloud remains gravitationally unbound.

1.5 Previous numerical work

The simulations presented here consider the hydrodynamics of the gas and the response of the gas to a spiral potential. Without instabilities from self gravity or cooling, the formation of discrete clouds in the spiral arms at first seems unlikely. Calculations by Dwarkadas & Balbus (1996) showed that a gas flow subject to a spiral potential is stable against purely hydrodynamical i.e. Rayleigh-Taylor or Kelvin-Helmholtz type instabilities, for the parameters chosen in their model. Thus one would predict continuous spiral arms traversing the disk roughly coincident with the minimum of the potential (Roberts, 1969). Likewise several simulations of gas flow in a spiral potential show smooth symmetirc spiral arms (Patsis et al., 1997; Chakrabarti et al., 2003), although the branching of spiral arms occurs at radii corresponding with resonances in the disk. The 2D disk simulations of Wada & Koda (2004) and Gittins (2004) do show structure along the spiral arms, although this structure is not particularly extensive. Spurs form perpendicular to the arms, but the length of these is much less than the interarm width.

These previous simulations of gaseous disks all assume a single phase, isothermal medium, generally in a non self-gravitating disk without magnetic fields. The sound speed is usually 10 km s^{-1} corresponding to the warm neutral phase of the ISM. Gómez & Cox (2002) include magnetic fields, but the large scale structure is similar to purely hydrodynamic calculations (e.g. those of 10^4 K in Chapter 4). Other numerical analysis of disks has investigated the location of the spiral shock (Gittins & Clarke, 2004), and the dependence of the spiral morphology on the pattern speed of the potential and sound speed of the gas (Slyz et al., 2003). Kim et al. (2002) take a section of the disk and include a spiral potential with periodic boundary conditions, magnetic fields and self gravity. Their results show the collapse of gas in spiral arms due to gravitational and Parker instabilities, and the formation of prominent spurs perpendicular to the spiral arms (Kim & Ostriker, 2002). The ISM is again assumed to be isothermal with a similar sound speed to the simulations described above. Bonnell et al. (2006) model the passage of a region of cold gas through a spiral arm, the formation of GMCs and the triggering of star formation. Although gravitational instabilities induce star formation in the gas, they find that the dynamics of the gas are primarily dependent on the clumpy initial distribution of the ISM and the spiral shock.

Numerical simulations which investigate more detailed physics of the ISM have become more widespread over the last decade, following Vazquez-Semadeni et al. (1995), who model a section of the galactic plane and Rosen & Bregman (1995), who model the vertical structure of the disk. A review of numerical analysis of the ISM is given in Vázquez-Semadeni (2002). The distribution of the ISM from numerical results appears consistent with observations but a significant proportion of gas is present which lies outside the regimes described by the traditional 3 phase model. Most of the simulations are 2D and typically represent a 1 kpc by 1kpc area of the disk. Those of Vazquez-Semadeni et al. (1995) assume a turbulent, self gravitating medium with heating and cooling, and further results include shear rotation and magnetic fields (Passot et al., 1995). More recent simulations have considered the generation of turbulence in the ISM from thermal instabilities (Audit & Hennebelle, 2005; Heitsch et al., 2005) and the magnetorotational instability (Piontek & Ostriker, 2005). Heitsch et al. (2005) also propose the formation of molecular clouds through thermal instabilities in HI flows. Glover & Mac Low (2006a,b) have

recently produced models of the ISM which include the transition of atomic to molecular hydrogen.

The localised ISM simulations generally ignore galactic scale processes such as spiral shocks or rotational shear. Simulations to include a comprehensive treatment of the ISM on galactic scales have been performed in 2D (Wada & Norman, 1999, 2001) and recently 3D (Tasker & Bryan, 2006). These calculations do not include a spiral potential - instead gravitational instabilities induce flocculent structure. Gravitational instabilities and cooling of the ISM contribute to a cold (≤ 100 K) phase of gas associated with molecular cloud formation (Wada & Norman, 1999). Star formation is predicted where the Toomre instability criterion is satisfied in the disk (Li et al., 2005; Tasker & Bryan, 2006). The inclusion of feedback, whilst adding a hot phase to the ISM does not appear to be necessary for complex structure to occur in the plane of the disk (Wada & Norman, 2001). Simulations of supernovae in a localised region of a galactic disk (de Avillez & Breitschwerdt, 2005) show that supernovae are however required to reproduce the vertical structure of the disk and can compress gas into high-latitude clouds, above the plane of the disk.

As yet, there are no simulations of grand design spirals with a detailed treatment of the ISM or stellar energy feedback. Simulations which include magnetic fields and self gravity are now commencing. As will become apparent in this thesis, the dynamics of the spiral shock alone are complicated, without including additional physics. However some discussion of expected future work is included in Chapter 7.

1.6 Outline of Thesis

This thesis describes numerical models of the formation of molecular clouds in spiral galaxies. Although the simulations presented here represent a simple model, of a gaseous disk subject to a spiral potential, the results shown in this thesis indicate that discrete clouds of gas with a high degree of structure can form in the spiral arms. This was a surprising outcome and not expected before the simulations commenced. This thesis attempts to analyse their formation, structure and correspondence with observations. The conditions required for the formation of these clouds are discussed, and why they have not been reported in other models or simulations.

Chapter 2 describes the Smoothed Particle Hydrodynamics (SPH) code used to perform these simulations. Various tests are performed to establish how well SPH, and recently suggested modifications to SPH, are able to model shocks. Chapter 3 follows on from Bonnell et al. (2006), who propose the generation of a velocity dispersion in clumpy shocks. This chapter analyses shocks using different initial gas distributions to determine the velocity dispersion relation of the gas. The motions of the gas are compared with the usual view of turbulence in molecular clouds.

The rest of the thesis is primarily concerned with molecular cloud formation. Chapter 4 describes the initial conditions for the simulations and the theories and observations on which they are based. The growth of structures in the spiral arms is described and the mechanism for formation of this structure are explained. Chapter 4 also includes a more detailed analysis of interarm spurs, a clear feature in these simulations. Chapter 5 then

explains the formation of molecular hydrogen in the ISM and calculates the molecular gas content of the galactic disk. It is shown that the clouds formed in the spiral arms contain a significant fraction of molecular gas. Chapter 6 examines the dynamics and formation of molecular clouds in a 2 phase medium.

CHAPTER 2

Smoothed Particle Hydrodynamics

The simulations described in this thesis use the Smoothed Particle Hydrodynamics method (SPH). SPH is a 3D Lagrangian hydrodynamics code that has been successfully applied to a variety of astrophysical problems. An advantage of SPH is that it is highly adaptable, and computational simulations can be set up with any distribution of particles, over many scales. As the code is Lagrangian, SPH uses an interpolation method to determine physical quantities such as density and pressure. The code has been subject to major modifications since the version of Benz (1990). In particular particles now evolve with individual timesteps and gravitational forces are calculated using a hierarchical tree (Benz et al., 1990). Recent modifications include magnetic fields (Price & Monaghan, 2004, 2005) and radiative transfer (Whitehouse & Bate, 2004; Stamatellos & Whitworth, 2005; Whitehouse & Bate, 2006; Viau et al., 2006), but these are beyond the scope of this thesis.

A major criticism of SPH is the handling of shocks. This chapter includes a discussion of 2 methods to improve the treatment of shocks by SPH and their implementation. These methods are applied to simple shock tube tests and the results compared with the original SPH code and analytic solutions. Since much of this thesis concerns spiral density wave shocks, the ability of SPH to handle shocks is highly relevant.

2.1 The SPH equations

SPH was developed independently by Lucy (1977) and Gingold & Monaghan (1977). The derivation of the SPH equations is described in previous papers (Monaghan, 1982; Benz, 1990) and is not included here. However the main equations and components of the code are introduced below.

Any continuous function $f(\mathbf{r})$, defined over a space V, can be approximated by a smoothed function

$$< f(\mathbf{r}) >= \int_{\mathbf{V}} \mathbf{W}(\mathbf{r}-\mathbf{r}',\mathbf{h})\mathbf{f}(\mathbf{r}')\mathbf{dr}'. \tag{2.1}$$

The function W is known as the kernel and satisfies the following properties:

$$\int_V W(\mathbf{r},\mathbf{h})\mathbf{dr}' = 1 \qquad \text{and} \tag{2.2}$$

$$W(\mathbf{r}-\mathbf{r}',\mathbf{h}) \rightarrow \delta(\mathbf{r}-\mathbf{r}') \qquad \text{as} \qquad \mathbf{h} \rightarrow \mathbf{0}. \tag{2.3}$$

The parameter h, the smoothing length, represents the width of the kernel and thereby determines the degree of space over which the function f is smoothed. By choosing a kernel highly peaked at $\mathbf{r} = \mathbf{r'}$, $< f(\mathbf{r}) >$ approximates $f(\mathbf{r'})$ to second order in h. A variety of kernels have been tested in SPH, but typically a spline kernel is used (Monaghan & Lattanzio, 1985).

SPH is a particulate code and so uses a discrete form for the smoothing function. For N particles, Equation 2.1 becomes

$$< f(\mathbf{r}) >= \sum_{\mathbf{j=1}}^{\mathbf{N}} \frac{\mathbf{m_j}}{\rho(\mathbf{r_j})} \mathbf{f}(\mathbf{r_j}) \mathbf{W}(|\mathbf{r} - \mathbf{r_j}|, \mathbf{h}). \tag{2.4}$$

This is the central equation in SPH, since f can be replaced by any desired variable. For example, inserting $f(\mathbf{r}) = \rho(\mathbf{r})$ gives the density

$$< \rho(\mathbf{r}) >= \sum_{\mathbf{j=1}}^{\mathbf{N}} \mathbf{m_j} \mathbf{W}(|\mathbf{r} - \mathbf{r_j}|, \mathbf{h}). \tag{2.5}$$

The format of Equation 2.4 also allows the gradient and divergence of variables to be written as smoothed quantities. The continuity equation is automatically satisfied through Equation 2.5, and the SPH momentum equation can be determined by applying Equation 2.4 to the Eulerian momentum equation. Hence the momentum equation becomes

$$\frac{d\mathbf{v_i}}{dt} = -\sum_{j \neq i} m_j \left(\frac{P_i}{\rho_i^2} + \frac{P_j}{\rho_j^2} + \Pi_{ij} \right) \nabla_i W_{ij} \tag{2.6}$$

where Π_{ij} is the artificial viscosity and ∇_i denotes gradient with respect to particle i. The viscosity term allows for an artificial treatment of shocks in SPH and is described further in Section 2.2. The SPH equations for energy conservation, radiation transport and Poisson's equation are described in Benz (1990). These are not applied in this work though since the gas is assumed to be isothermal and non self-gravitating.

In addition to the physical variables, SPH particles also exhibit individual smoothing lengths and timesteps. This allows greater flexibility with the code, as typical length scales and densities can vary without the computational time increasing extensively. The smoothing length for each particle can be scaled to vary with the density, as

$$h = h_0 \left(\frac{\rho_0}{\rho} \right)^{1/3}, \tag{2.7}$$

so the number of neighbours of each particle remains similar (usually ~ 50). Following Benz (1990), the time derivative of the smoothing length is

$$\frac{dh}{dt} = -\frac{1}{3} \frac{h}{\rho} \frac{d\rho}{dt}. \tag{2.8}$$

Then using the continuity equation to replace $d\rho/dt$ gives

$$\frac{dh_i}{dt} = \frac{1}{3} h \nabla . \mathbf{v_i}. \tag{2.9}$$

The SPH equations are integrated using a second order Runge-Kutta integrator. The particles evolve on individual timesteps, with each particle integrated over a timestep of $1/2^n dt$ where $0 \leq n \leq 20$. Thus particles in denser regions can evolve on much shorter timesteps than those in less dense regions.

2.2 SPH and shocks

One of the difficulties in SPH, compared to other methods, is the handling of shocks. In the derived SPH equations there is no dissipative process to convert kinetic to thermal energy when gas shocks. This leads to the problem of particle penetration, where colliding streams of particles are able to pass through each other. Consequently, variables such as the velocity may become multivalued where the gas shocks. To remove this problem, an artificial viscosity term is introduced into the SPH momentum equations which acts like a pressure term.

The artificial viscosity commonly used (Monaghan & Gingold, 1983) is

$$\Pi_{ij} = \begin{cases} -\frac{\alpha h \mathbf{v_{ij}} \cdot \mathbf{r_{ij}}}{\bar{\rho}_{ij} |\mathbf{r_{ij}}|^2} \left(\bar{c}_{ij} - \beta \frac{h \mathbf{v_{ij}} \cdot \mathbf{r_{ij}}}{|\mathbf{r_{ij}}|^2} \right) & \text{if } \mathbf{v_{ij}} \cdot \mathbf{r_{ij}} < \mathbf{0} \\ 0 & \text{otherwise} \end{cases} \tag{2.10}$$

where h is the smoothing length, $\mathbf{v_{ij}} = \mathbf{v_j} - \mathbf{v_i}$, $\mathbf{r_{ij}} = \mathbf{r_j} - \mathbf{r_i}$, $\bar{c}_{ij} = (c_i + c_j)/2$, and $\bar{\rho}_{ij} = (\rho_i + \rho_j)/2$. This is based on a bulk velocity term and the von Neumann-Richtmyer artificial pressure:

$$\begin{array}{cc} \text{bulk} & \Pi = -\alpha \rho l c \nabla \cdot \mathbf{v} \\ \text{von Neumann-Richtmyer} & \Pi = -\beta \rho l^2 (\nabla \cdot \mathbf{v})^{\mathbf{2}} \end{array}$$

Typically $\beta = 2\alpha$ in SPH simulations, hence the deceleration in Equation 2.6 due to the viscosity is determined by the constant α. Tests (Bate, 1985) indicate that $\alpha \gtrsim 0.8$ is required to prevent inter-particle penetration and accurately reproduce a Mach 2 shock, but larger viscosities are required for stronger shocks.

Values of $\alpha = 1$ and $\beta = 2$ are shown to be adequate for most SPH simulations (Monaghan & Gingold, 1983). Very high viscosities are not desirable as the shocks will be too dissipative. For high Mach number shocks however, this artificial viscosity is not always sufficient to produce sharp accurate shocks. Instead shocks show smearing as particles are able to penetrate through the shock. Several suggestions have been made to improve the accuracy of modelling shocks in SPH. The 3 main possibilities considered are:

- allowing the viscosity to vary with time, and increase to larger values if required
- XSPH, which uses a smoothed velocity to update particle positions and prevent particle penetration
- Gudonov SPH, which uses a Riemann solver to include the analytical results of shock tube tests

The first two of these improvements are described next.

2.2.1 Viscosity switch

Morris & Monaghan (1997) propose a variable α viscosity parameter. In this method particles exhibit individual viscosities, which allows the viscosity to increase upon approaching

a shock and then decay. The parameter α evolves with time according to

$$\frac{d\alpha}{dt} = -\frac{\alpha - \alpha^*}{\tau} + S. \tag{2.11}$$

The first term on the right is a decay term which allows the viscosity to return to α^* over a time period τ, dependant on the sound speed and smoothing length. The parameter α^* is set to 0.1, which represents the default viscosity of the particles away from shocks. The second term on the right is a source term, chosen to increase the viscosity as a particle approaches a shock. Morris & Monaghan (1997) use the velocity divergence, $S = max(-\nabla \cdot \mathbf{v}, \mathbf{0})$, so overall Equation 2.11 becomes

$$\frac{d\alpha}{dt} = -(\alpha - \alpha^*)\frac{C_1 c}{h} + max(-\nabla \cdot \mathbf{v}, \mathbf{0}). \tag{2.12}$$

C_1 is a constant, set to 0.2 for α to decay back to α^* over ~ 2 smoothing lengths (see Morris & Monaghan (1997)) and c is the sound speed.

2.2.2 XSPH

XSPH was suggested by Monaghan (1989, 2002) to prevent particle penetration by velocity smoothing. Monaghan (1989) defines the smoothed velocity $\widehat{\mathbf{v}}_i$ as the average over the velocities of the neighbouring particles:

$$\widehat{\mathbf{v}}_i = \mathbf{v_i} + \epsilon \sum_{\mathbf{j} \neq \mathbf{i}} \frac{\mathbf{m_j}}{\rho_\mathbf{j}} \mathbf{v_{ij}} \mathbf{W_{ij}}. \tag{2.13}$$

This is equivalent to Equation 2.4, where $\mathbf{f}$ is replaced by $\mathbf{v}$. The parameter $0 < \epsilon < 1$ determines the degree of velocity smoothing, $\epsilon = 0$ for SPH and $\epsilon = 1$ for full XSPH. A value of $\epsilon = 0.5$ is suggested in Monaghan (1989).

The smoothed velocity is then used to update the particles positions instead of the individual particle velocities, according to

$$\frac{d\mathbf{r}}{dt} = \widehat{\mathbf{v}}_i. \tag{2.14}$$

Then, for example, the smoothed velocity in the centre of a shock is determined by the average of the incoming velocities and will be 0, as required, and the velocity cannot become multivalued. It can further be shown (Monaghan, 2002) that XSPH conserves angular and linear momentum, and is non-dissipative.

2.3 Shock tube tests

Shock tube tests are carried out for SPH and these modified versions of SPH. To summarize, the different codes investigated are

- SPH: standard version of SPH
- XSPH: particle positions are updated with smoothed velocities

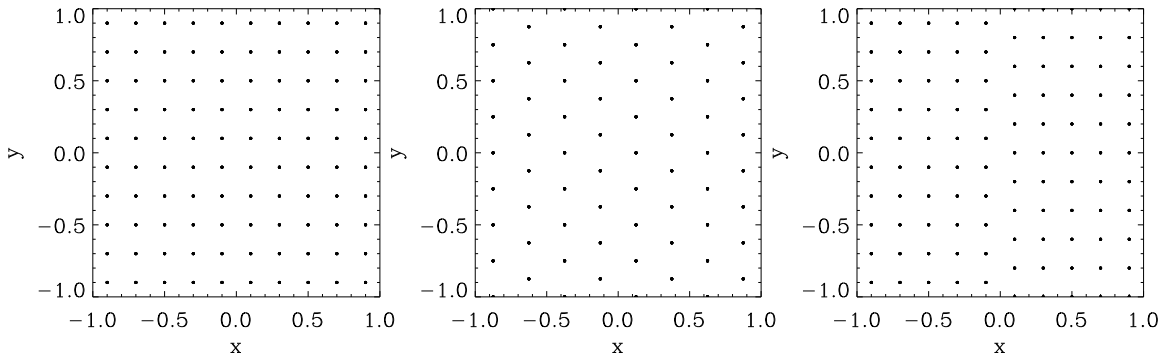

Figure 2.1: The different particle distributions used: cubic lattice (left), unaligned lattice (centre) and offset distribution (right).

- αSPH: particles have individual values of α
- αXPSH: uses both XSPH and αSPH

The notation of the latter two is not standard, but is used here for convenience.

The shock tests themselves consist of two colliding flows and are set up with velocities allocated in the x direction, $v_x = v_0$ for $x < 0$ and $v_x = -v_0$ for $x > 0$. All the tests in this chapter are in 3D, so the shock occurs in the yz plane. These tests use 3 different particle distributions - the unaligned lattice, cubic lattice and offset distribution (Figure 2.1). The offset distribution is used primarily to test for particle penetration, since this will be the worst case scenario, although unlikely to occur in real simulations. The unaligned lattice is more likely to resemble simulations. Reflective (cubic lattice) or periodic (unaligned lattice and offset distribution) boundary conditions are used, so ghost particles continue the distributions of particles in Figure 2.1.

The α and β values are set as fixed parameters in SPH and XSPH, or as arrays for individual particles in αSPH and αXSPH. Here, as common in SPH, the β parameter is set as twice α. The viscosity is described in terms of α, although as shown by Bate (1985), the bulk term determined by β is of more consequence in shock simulations than the α term in Equation 2.10. For αSPH and αXSPH, the initial array of α is set to 0.1, the same as the minimum viscosity in the decay term in equation 2.12. Since the viscosity increases relatively quickly as gas approaches a shock, the initial value of α is not expected to be of particular importance. Boundary particles are also allocated individual values of α.

Both isothermal (polytropic index of $\gamma = 1$) and adiabatic tests ($\gamma = 5/3$) are investigated. The problem of particle penetration is first considered before a comparison between shocks produced by the different codes and analytical solutions (Section 2.3.5).

2.4 Particle penetration

The problem of particle penetration is investigated for the 4 different codes, although primarily to investigate the difference of the XSPH velocity smoothing included specifically to prevent this problem (Monaghan, 1989). Tests are first carried out with an offset distribution, for which particle penetration will be most problematic. All the shocks in this section are isothermal, but particle penetration generally occurs less for adiabatic shocks (Bate, 1985). The particles take initial velocities of $v_0 = 1c_s$. For the early stages of the shock, which are used for these results, the Mach number is 2. The particles are initially distributed in a cube $-4 < x < 4$, $-1 < y < 1$, $-1 < z < 1$ and the resolution of the grid is 8 particles per unit length.

Figure 2.2 shows the distribution of particles over the xy plane, comparing XSPH and codes with different artificial viscosity parameter α. For an ideal shock, the shock location lies at $x = 0$ and particles should stop as they reach the yz plane at $x = 0$. The top two figures show results where the artificial viscosity is switched off, i.e. $\alpha = 0$. For standard SPH, the opposing streams of particles fully penetrate through each other. By contrast, the particles are completely stopped on their approach to the shock front for full XSPH (where the XSPH parameter ϵ is set to 1), even though there is no artificial viscosity. The further plots show results when $\alpha = 1$, since this is typically used in SPH calculations, and the αSPH code. There is very little particle penetration for the $\alpha = 1$ case, with only one layer of particles penetrating the opposing stream. The fourth diagram shows the particle distribution for the αSPH code, which produces a higher degree of particle penetration. The reason for this can be seen from looking at the values of α for the particles. As shown in Figure 2.3, the value of α increases to a maximum of 0.8, lower than the SPH run and insufficient to completely prevent particle penetration.

2.4.1 Particle penetration with different Mach number shocks

Shock tests are performed to investigate the degree of particle penetration for different Mach number isothermal shocks. These tests use the 4 different codes, SPH XSPH, αSPH and αXSPH. For the XSPH and αXSPH codes, the XSPH parameter (ϵ in Equation 2.13) is set to 0.5, as suggested (Monaghan, 1989). For the αSPH and αXSPH tests, the variable α is initially set to 0.1 for all the particles, whilst the standard viscosity $\alpha = 1$ is used for SPH and XSPH. Again the offset lattice distribution of particles is used, of dimensions $-4 < x < 4$, $-1 < y < 1$ and $-1 < z < 1$. Previous analysis (Bate, 1985) shows that particle interpenetration is not halted for isothermal shocks of Mach numbers ≥ 4 for the offset distribution. The particle penetration is thus quantified by recording the number of layers of particles which cross into the opposing stream of particles, and compared for the different codes at a certain time. An example of a case where there are 4 layers of penetration is shown in Figure 2.4. A smaller number of layers indicates that less particle penetration is occurring and the shock is more accurately treated by the code.

The number of layers for different Mach numbers is shown in Table 2.1 at 2 different times. The times are given in terms of the initial velocity, so the same number of particles are expected to approach the shock for each Mach number. With no pressure or viscosity, the number of layers penetrated at $t = 2/v_0$ is 9 and at $t = 4/v_0$ is 18. For the $v_0 = c_s$ and

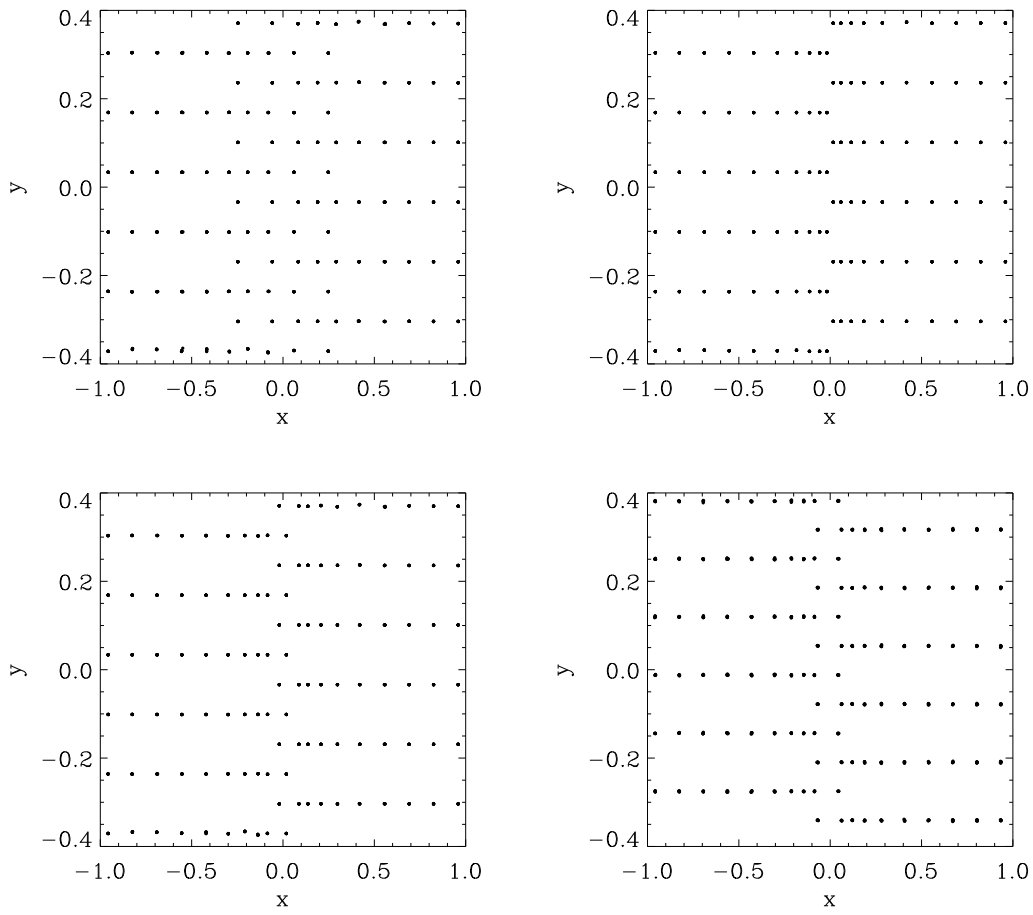

Figure 2.2: Comparison of particle penetration for the SPH, XSPH and αSPH codes. The SPH (top left) and XSPH (top right) examples do not use any artificial viscosity terms. Also shown is SPH with $\alpha = 1$ (bottom left) and the αSPH code (bottom right). The figures are shown at $t = 1/v_0$ and the initial velocity is $v_0 = 1c_s$.

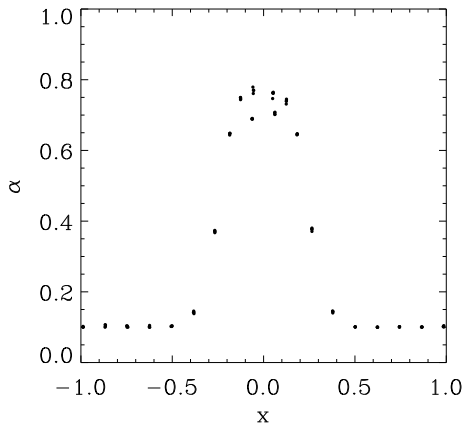

Figure 2.3: The values of α for the particles in the αSPH simulation shown in Figure 2.2.

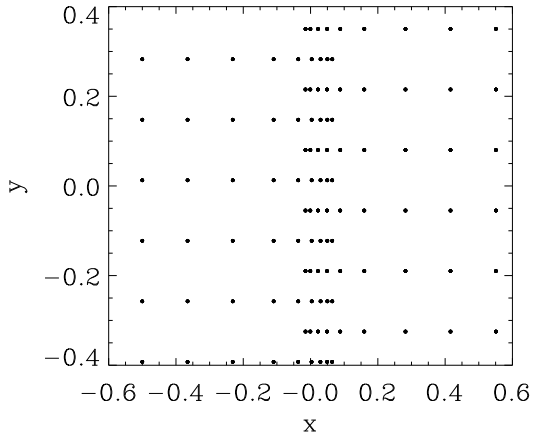

Figure 2.4: Example showing 4 layers of particle interpenetration. This is taken from an XSPH simulation with Mach number 10. The time of the simulation is $t = 2/v_0$

v_0	No. layers at $t = 2/v_0$				No. layers at $t = 4/v_0$			
	SPH	XSPH	αSPH	αXSPH	SPH	XSPH	αSPH	αXSPH
1	1	0	2	0	1	0	2	0
2	3	2	3	2	9	5	8	4
5	5	4	5	3	10	8	9	7
10	5	4	5	3	10	9	9	7
20	5	4	5	4	10	9	10	8

Table 2.1: Table showing the number of particles for each layer which cross into the opposing stream for SPH, XSPH, αSPH and αXSPH codes. The offset particles distribution is used, for different Mach number shocks.

$v_0 = 2c_s$ shocks, penetration is halted by $t = 4/v_0$. However for the higher Mach number shocks further penetration is still ongoing.

Figure 2.5 shows the growth of α with time for the Mach 2, 4 and 40 shocks corresponding to the tests of αSPH and αXSPH in Table 2.1. Again the time is scaled so that for each initial velocity (v_0), the number of particles reaching the shock is the same. The maximum value of α peaks at approximately 0.8 and 1.4 for the Mach 2 and 4 shocks respectively. Although not plotted, α peaks at ~ 2.3 and 2.6 for the Mach 10 and 20 shocks. The value of α does not stabilise until after $t = 4/v_0$ for the Mach 40 shock, eventually reaching a maximum of ~ 3.5. The values of α obtained for the αXSPH code are generally greater than for αSPH. This is because the increase in viscosity is dependent on a source term, proportional to the divergence of the velocity. XSPH works by smoothing the velocities of the incoming particles and thus the particles decelerate more (in comparison to standard SPH) as they approach the shock. Consequently the source term is larger when the XSPH is included.

For the offset lattice distribution, Table 2.1 indicates that XSPH provides a significant reduction in particle penetration for low Mach number shocks and a slight improvement at high Mach number shocks. The αSPH code does not fare so well, although

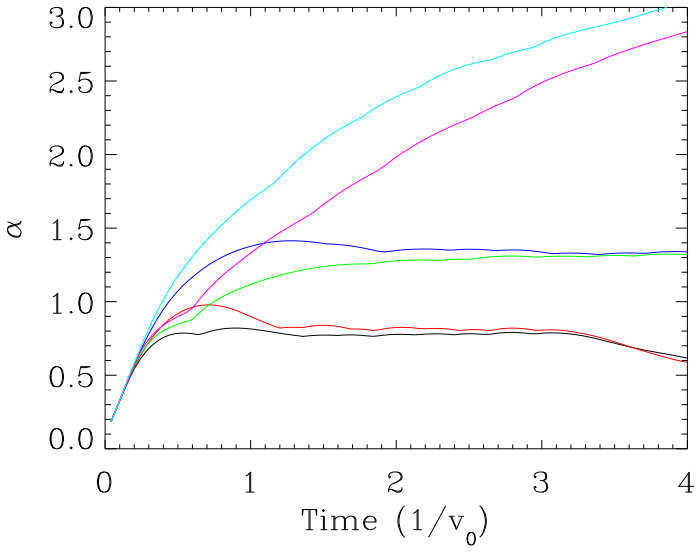

Figure 2.5: Plot showing values of the maximum value of α with time, obtained for the αSPH and αXSPH codes, using results from the same simulations as given in Table 1. Lines are given for the αSPH code with $v_0 = 1c_s$ (black), $v_0 = 2c_s$ (green), $v_0 = 20c_s$ (magenta) and the αXSPH code with $v_0 = 1c_s$ (red), $v_0 = 2c_s$ (blue) and $v_0 = 20c_s$ (cyan).

unlike XSPH, the viscosity switch was not introduced explicitly to prevent particle penetration. The viscosity parameter α increases to 0.8, when $v_0 = c_s$, slightly less than the standard value of 1, but sufficient to prevent most particle penetration. For the highest Mach numbers, the increase in particle penetration at $t = 2/v_0$ is likely due to α not increasing sufficiently quickly to prevent penetration. However α can be set to a higher value initially, which would ensure that αSPH would perform at least as well as SPH for low Mach number shocks.

The αXSPH code is most effective for high Mach number shocks, reducing particle penetration by 20%. However Table 2.1 does not fully represent the effectiveness of αXSPH, since the distance of particles travelling through the shock into the opposing stream was greatly reduced, e.g. for $v_0 = 10$, particles had reached distances of $x = \pm 0.08$ into the opposing streams for αXSPH, half that of standard SPH and some improvement on XSPH or αSPH alone.

2.4.2 Increasing the source term

For the higher Mach number shocks, α does not peak until a later time, after several particles have entered the shock ($t = 2/v_0$ corresponds to 9 particles entering the shock). This suggests that using an higher initial α may improve the variable α codes, but tests with the initial and decay values of α set to 1 for the α XSPH code show the same degree of penetration as indicated in Table 2.1. However, the source term could also be increased in order that higher values of α are obtained. The degree of particle pentration is shown when

Increase in source term	No. layers at $t = 2/v_0$		No. layers at $t = 4/v_0$	
	αSPH	αXSPH	αSPH	αXSPH
1	5	3	9	7
2	4	2	8	7
4	2	1	6	4
10	1	0	3	2

Table 2.2: Table showing the number of particles for each layer which cross into the opposing stream for αSPH and αXSPH codes. The offset particles distribution is used, and v_0=5c_s for all the shocks. The source term (Equation 2.11) is increased by a constant factor.

the source term is increased in Table 2.2, when $v_0 = 5c_s$. In each case, the maximum value of α increases by the same factor as the source term is increased. As indicated by Table 2.2, increasing the source term greatly reduces the degree of penetration, so that if the source term is increased by a factor of 10, there is very little penetration. The disadvantage is that the width of the shock increases, since α becomes high earlier as particles approach the shock, and consequently the density of the shock is underestimated. When the source term is doubled, there is very little difference in the densities. For an increase in the source term by a factor of 4, the density decreases by 15%, and when the source term is increased by a factor of 10, the density in the shock is reduced by over one third.

2.4.3 Particle penetration dependence on the XSPH parameter ϵ

The XSPH velocity equation (Equation 2.13) includes the variable parameter ϵ which can be varied to give different degrees of smoothing. The number of layers of penetrating particles is shown in Table 2.3, when $v_0 = c_s$ and $v_0 = 5c_s$ (for the XSPH code). The number of particles is given for the case where there is no viscosity ($\alpha = 0$) and where the standard viscosity $\alpha = 1$ is used. The degree of particle penetration shows a small decrease for larger values of ϵ when $\alpha = 1$. A similar dependence on ϵ is likely for αXSPH, if an initial α of 1 is applied. The suggested value of $\epsilon = 0.5$ in XSPH is just sufficient to prevent penetration for the $v = 1c_s$ case (Table 2.1). As expected, the effect of changing ϵ is much more significant when there is no viscosity, since the ability of the gas to shock depends solely on the XSPH term.

2.4.4 Varying the initial distribution

The results so far have only used the offset particle distribution to measure particle penetration. This is clearly the most disadvantageous distribution for shocks in SPH, and unlikely to correspond to most simulations. This section looks at particle penetration when different distributions of particles are used. Firstly an unaligned lattice distribution (Figure 2.1) is tested. The simulations are otherwise the same as in Table 2.1 - the SPH code takes $\alpha = 1$, XSPH and αXSPH use $\epsilon = 0.5$ and the initial value of α is 0.1 for the variable SPH codes. The same range of initial velocities is applied and reflective boundary conditions are used.

ϵ	No. of layers ($v_0 = c_s$)		No. of layers ($v_0 = 5c_s$)	
	$\alpha = 0$	$\alpha = 1$	$\alpha = 0$	$\alpha = 1$
0.0	9	1	9	4
0.2	7	1	8	4
0.4	4	1	8	4
0.6	2	0	6	4
0.8	1	0	5	3
1.0	0	0	4	3

Table 2.3: The number of particles crossing into the opposing stream is tabulated for different values of ϵ. All these simulations use the XSPH code with the offset lattice distribution. Two different initial velocities are compared, $v = 1c_s$ and $v_0 = 5c_s$. The effectiveness of XSPH is shown for the case where there is no artificial viscosity, and where $\alpha = 1$.

Table 2.4 indicates that particle interpenetration is minimal for the unaligned lattice. For most of the tests, 0 or 1 particles pass the shock boundary, and in all cases, none of the particles continue to pass through the shock, as happened with the offset distribution. The standard SPH code allows a few particles to penetrate the shock boundary. The XSPH and variable α codes reduce this. In a couple of cases, the first layer of particles initially passed across the shock boundary (and thereby past the first layer of particles immediately above or below for the unaligned lattice), but subsequently pass back as pressure forces act on the shocked region. Longer tests for the Mach 40 shock with αSPH, XSPH and αXSPH showed no further penetration than indicated in Table 2.4.

Tests were also carried out for the cubic lattice, but no particle interpenetration occurred for the Mach 40 shock. This is not surprising since this is the optimum distribution for preventing particle interpenetration. Similar tests by Bate (1985) showed that for shocks of Mach 10 or less, there is no particle interpenetration for the unaligned or cubic lattice with SPH for viscosity parameters similar to those applied here.

The values of α were also recorded for the runs with different distributions. As would be expected, there is minimal variation of α for the different distributions. Figure 2.6 shows the variation of α with time for a Mach 10 shock, for the 3 different distributions.

Simulations at higher resolution are also used to investigate whether the resolution has any effect on the values of α, or particle interpenetration. Figure 2.7 shows the variation of α with time for different resolution tests. These tests use the unaligned lattice and take $v_0 = 5c_s$. Figure 2.7 indicates that the peak value of α does not depend on the resolution The only difference is that for the higher resolution runs, α increases slightly more rapidly, which may help to prevent penetration. However, for these tests, no difference in the degree of particle penetration was found.

2.5 Comparison with analytical solutions

Isothermal and adiabatic shocks are performed for the 4 different codes described, and the results are compared with analytic solutions. These solutions are provided using the

v_0	No. layers at $t = 2/v_0$				No. layers at $t = 4/v_0$			
	SPH	XSPH	αSPH	αXSPH	SPH	XSPH	αSPH	αXSPH
1	0	0	1	0	0	0	1	0
2	1	0	1	0	1	0	1	0
5	1	0	1	1	1	1	1	1
10	1	0	1	1	2	1	1	0
20	1	0	1	1	3	1	1	0

Table 2.4: Table showing the number of particles for each layer which cross into the opposing stream for SPH, XSPH, αSPH and αXSPH codes. The unaligned particle distribution is used, for different Mach number shocks.

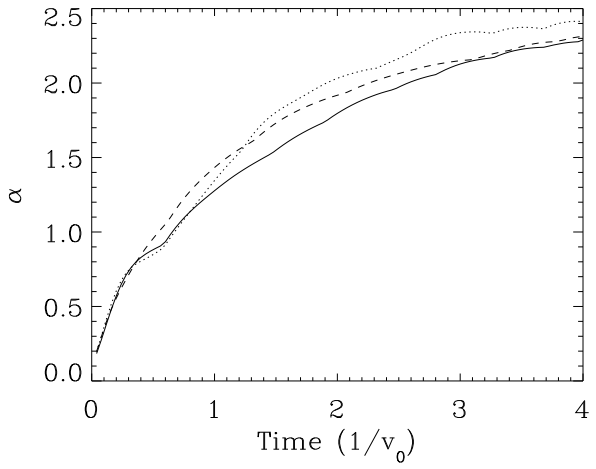

Figure 2.6: Plot showing the variation of the maximum value of α with time for the unaligned lattice (solid), cubic lattice (dotted) and offset (dashed) distributions. All shocks are Mach 10 and use the αSPH code.

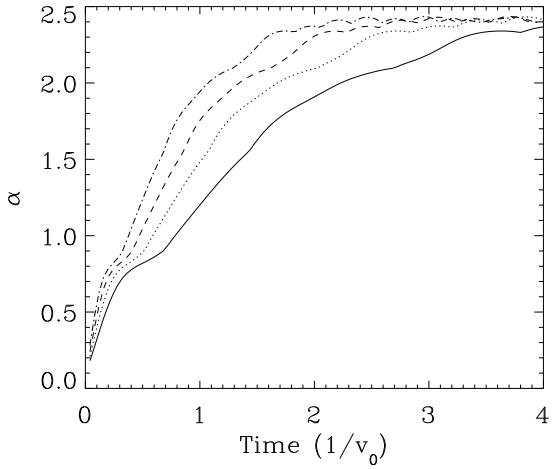

Figure 2.7: Plot showing the variation of the maximum value of α with time, for a resolution of 6 (solid), 8 (dotted), 10 (dashed) and 12 (dot-dash) particles per unit length. The unaligned lattice distribution is used. All shocks are Mach 10 and are performed with the αSPH code.

Hugoniot relations (Zel'dovich & Raizer, 1966). The shock is assumed to be of initial density ρ_0, pressure p_0, internal energy u_0 and with the opposing streams of gas travelling at v_0. The general solutions are given for the density of the shock ρ_1, velocity of the shock wave v, internal energy u_1 and pressure p_1. An ideal gas is assumed with sound speed $c_s = \sqrt{\gamma p/\rho}$. The shocks performed here are isothermal, ($\gamma = 1$), and adiabatic ($\gamma = 5/3$). For the adiabatic case, $p_0 = 1$, $\rho_0 = 1$, $u_0 = 1/(\gamma - 1)$, $c_s = \sqrt{\gamma}$ and the shock solutions are

$$v = \frac{(\gamma - 3)v_0 + \sqrt{\gamma + 1)^2 v_0^2 + 16\gamma}}{4}, \tag{2.15}$$

$$\frac{\rho_1}{\rho_0} = 1 + \frac{v_0}{v}, \tag{2.16}$$

$$\frac{u_1}{u_0} = \frac{\rho_0}{\rho_1} + v_0 v, \tag{2.17}$$

$$\frac{p_1}{p_0} = 1 + v_0(v + v_0). \tag{2.18}$$

where v and v_0 are in units of the sound speed c_s. For the isothermal case, with $\rho_0 = p_0 = c_s = 1$, the solutions simplify to

$$v = \frac{-v_0 + \sqrt{v_0^2 + 4}}{2}, \tag{2.19}$$

$$\frac{\rho_1}{\rho_0} = \frac{p_1}{p_0} = 1 + \frac{v_0}{v}. \tag{2.20}$$

The shock tests are set up in a similar way to described in Section 2.3. The unaligned lattice distribution is chosen as more representative of simulations compared with the cubic lattice and offset distributions. The resolution of the lattice is 11 particles per unit length. For the XSPH runs, the XSPH parameter ϵ is set to the standard value of 0.5, and for the variable α codes, α is initially set to 0.1. Otherwise, for SPH and XSPH $\alpha = 1$.

2.5.1 Isothermal shocks

Isothermal shocks of Mach 2 are performed for the 4 codes, and the results are displayed in Figure 2.8. For low Mach number shocks, SPH handles the shock relatively well, so the XSPH and variable α modifications do not make a significant improvement. Figure 2.8 shows that all 4 codes reproduce densities and velocities comparable with the analytical solutions. Values for the actual particles are plotted with different symbols, using particles from 1 layer of the lattice. The smoothed densities and velocities are also shown. For the density, the XSPH and αXSPH codes produced results closest to the analytical solutions. The density of the XSPH particles entering the shock is slightly lower than for the other codes. The particles are decelerated more with XSPH as they enter the shock compared to the other codes. The width of the shock is represented reasonably well for the different codes and does not vary between the codes for the Mach 2 shock.

The velocity of the particles is very similar for the 4 codes, and there is a barely noticeable difference in the smoothed velocities. Where the actual particle velocities are compared, there is a reduced degree of scatter for the SPH and XSPH compared with the variable α codes. This is most likely because, as described in Section 2.3, the value of α

reaches ~ 0.7 compared to the value of 1.0 assumed for SPH and XSPH. Previous tests (Bate, 1985) have demonstrated that larger viscosities reduce the density and velocity oscillations in the shock and thereby the velocity dispersion of gas in the shock.

Figure 2.9 shows a comparison between the different codes for a Mach 20 shock. This provides a better opportunity to compare the codes, since the SPH code does not reproduce the shock particularly well. The particle densities and velocities for a few layers are shown in Figure 2.9. The density for the SPH code is significantly underestimated, whilst the width of the shock is overestimated. There is a considerable degree of scatter, both in the densities and velocities of the particles, with the variation in the velocities corresponding to particle interpenetration in the shock. All the other codes show an improved treatment of the shock compared with standard SPH, with a reduced degree of scatter in both the densities and velocities. XSPH increases the density nearer to the analytical solution, and narrows the shock. XSPH produces a stronger deceleration of particles entering the shock compared with standard SPH. Streams of particles are still able to penetrate each other, as described in Section 2.2, and as can be seen by the velocity plot for XSPH in Figure 2.9. However, the particles in the XSPH velocity plot have velocities of ~ 0 in the shock indicating that they do not pass through the shock, as can occur for standard SPH. The width of the shock indicated in the density and velocity plots is still an overestimate compared to the analytical solutions.

The αSPH code shows the least degree of scatter in both the densities and velocities, since the viscosity increases to ~ 2.5 compared with the value of 1 assumed for the SPH and XSPH codes. The shock width is also more accurate, although the density is still underestimated. The αXSPH code combines the effects of XSPH and the variable α to increase the density and narrow the shock width. The smoothed density represents the analytic shock solution fairly well, and the velocity of the particles also shows good agreement. However there is some variation in the densities of particles in the shock, with some particles now overestimating the density. It may be possible for further improvement in the XSPH and αXSPH results by modifying the kernel, as suggested (Monaghan, 1982) to reduce the velocity dispersion. Also a larger increase in α (and therefore β) may be preferable.

2.5.2 Adiabatic shocks

Figure 2.10 shows the results for a Mach 2 adiabatic shock. The density, velocity and thermal energy (u) are compared with the analytic solutions for each of the 4 codes. There is not a significant difference between each of the 4 codes. The SPH and XSPH results are very similar, the XSPH code just giving slightly higher densities and thermal energies at the edge of the shock. This is similar to the XSPH code producing higher densities in the isothermal shocks, and corresponds to the greater deceleration of XSPH particles as they enter the shock. The overestimate of the thermal energy at the centre is due to wall heating (Monaghan, 1982). The oscillations in density, velocity and thermal energy apparent for the αSPH and αXSPH codes are again due to the lower value of α compared to the value of 1 for standard SPH. The viscosity parameter α inreases to ~ 0.55 at the edge of the shock, but is less in the centre (Figure 2.10). Since the width of the shock is relatively wide, the velocities and therefore divergence of particles in the centre

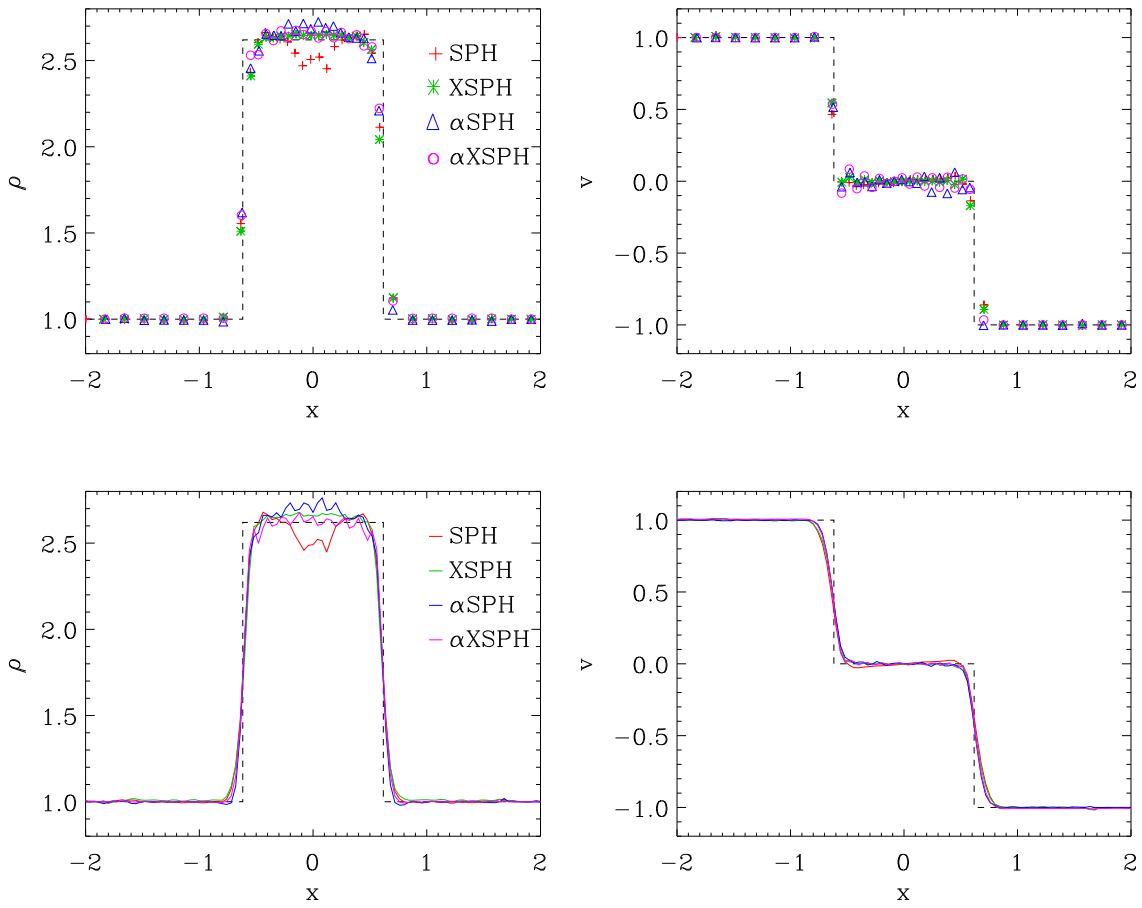

Figure 2.8: Comparison of Mach 2 isothermal shock for SPH , XSPH, αSPH and αXSPH at $t = 1$. The density (left) and velocity (right) are shown for a layer of particles (top) and the smoothed densities / velocities are shown as solid lines below. The dashed black lines show the analytic solution.

tends to 0. Hence the source term in Equation 2.12 is 0 and α decreases. The oscillations of the shock are larger, although as mentioned before, the default value of α can be set to 1 to improve the performance of αSPH.

The actual particles are not plotted, but the particles showed less scatter for SPH and XSPH compared with the αSPH and αXSPH codes. This is true for the density, velocity and thermal energy.

Similar plots are shown in Figure 2.11 for a Mach 20 adiabatic shock. The results show a similar degree of accuracy compared to the Mach 2 shock. Again the oscillations in the density, velocity and thermal energy are larger for the variable α codes. The SPH and XSPH results are almost the same. The value of α increases significantly more compared to the Mach 2 shock, and again α is very similar for the αSPH and αXSPH codes. Tests were carried out using αSPH and αXSPH with a default value of $\alpha = 1$, and the results were very similar to the standard SPH case. Including the XSPH velocity smoothing for the adiabatic shocks therefore has very little effect. Increasing the viscosity decreases the oscillations of the density and velocity across the shock front but increases the effect of

'wall heating' at the centre of the shock.

2.6 Summary of SPH, XSPH, αSPH and αXSPH

The XSPH codes perform shock tests at least as well as standard SPH. For a Mach 2 shock, the value of α for the variable α codes increases to a value comparable with that required to prevent penetration (Bate, 1985). However it is suggested that the initial and decay values of α are set to 1, the standard value, to ensure that the variable viscosity codes are optimised for treating shocks. The XSPH code was shown to reduce particle penetration compared with standard SPH, although for shocks of Mach number > 10 with an offset lattice, significant penetration still occurred. However, with a more typical distribution such as the unaligned lattice, XSPH largely prevents particle penetration. The αXSPH consistently gave the best results, even with the default value of $\alpha = 0.1$.

For the isothermal shocks, XSPH and αSPH both show improvements over the standard SPH code compared to the analytic solutions. These become more apparent for larger Mach number shocks. The combination of the 2 modifications, αXSPH produces the most successful code for modelling shocks. The adiabatic shocks, on the other hand showed little difference between the 4 codes, although XSPH is likely to reduce particle penetration for higher Mach numbers than those performed, or simulations with a different particle distribution.

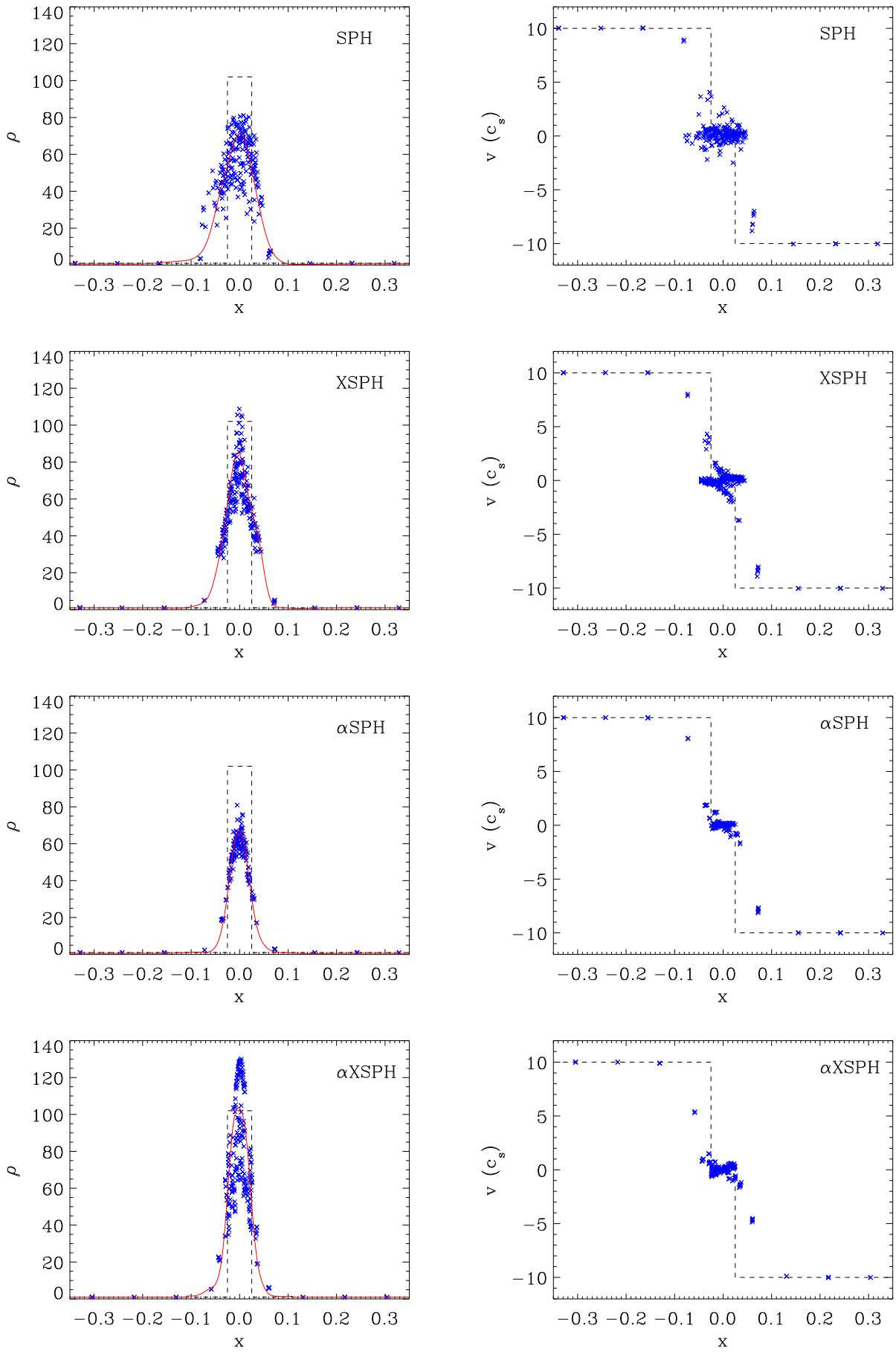

Figure 2.9: Comparison of Mach 20 isothermal shock for SPH, XSPH, αSPH and αXSPH at t=0.25. The density (left) and velocity (right) of a few layers of particles are indicated by blue crosses. The red line shows the smoothed density (along the line $y = 0$) and the dashed black line shows the analytic solution.

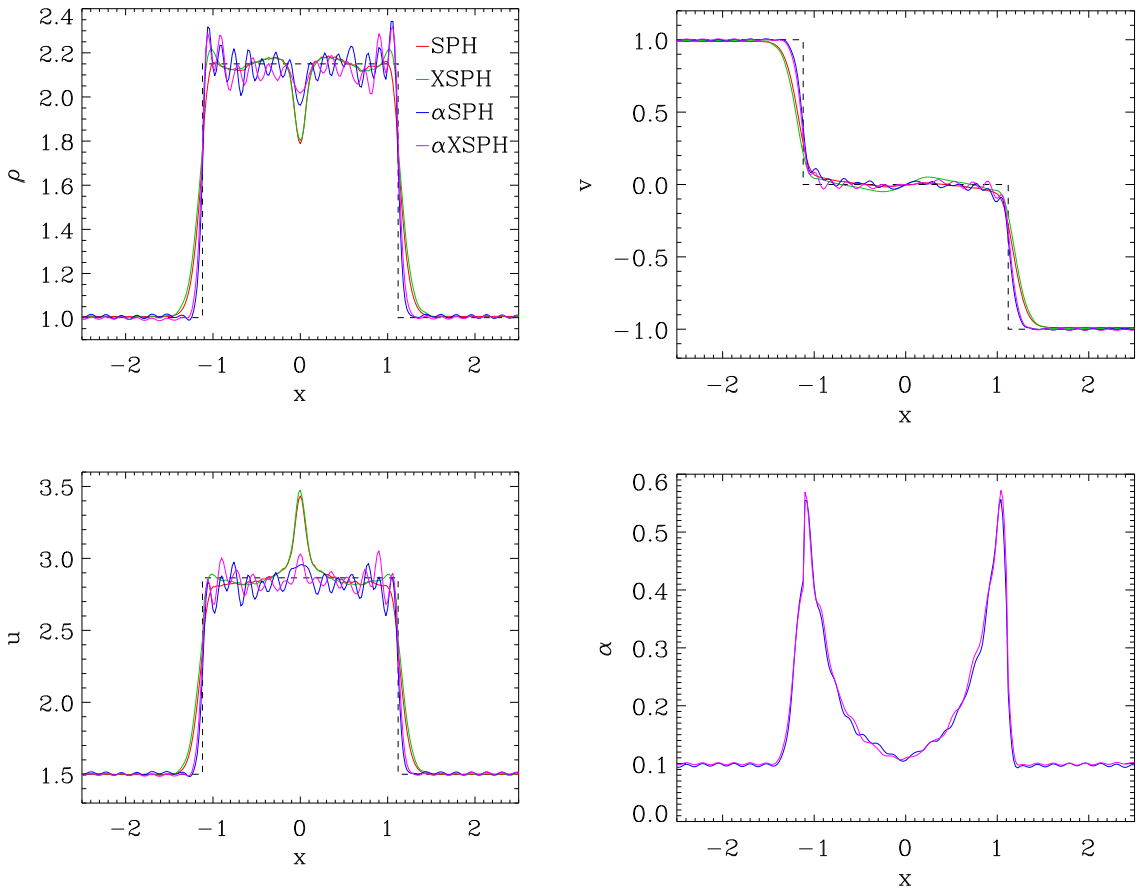

Figure 2.10: Comparison of adiabatic Mach 2 shock for SPH, XSPH, αSPH and αXSPH at t=1. The density (top left), velocity (top right) and thermal energy (bottom left) are plotted for the 4 codes, with the same colours in each plot. The analytic solutions are given by the dashed lines. The bottom right figure shows the viscosity α for the αSPH and αXSPH codes.

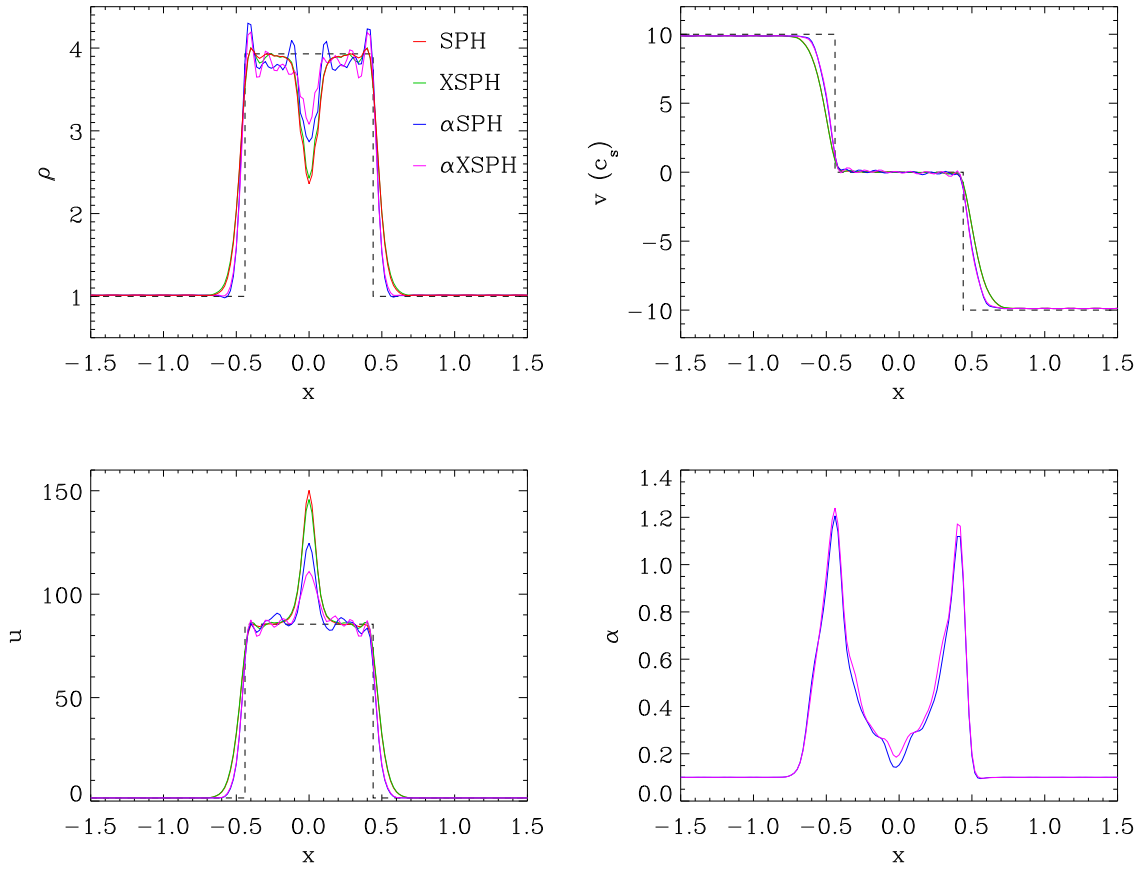

Figure 2.11: Comparison of adiabatic Mach 20 shock for SPH, XSPH, αSPH and αXSPH at t=0.1. The density (top left), velocity (top right) and thermal energy (bottom left) are plotted for the 4 codes, with the same colours in each plot. The analytic solutions are given by the dashed lines. The bottom right figure shows the viscosity α for the αSPH and αXSPH codes.

CHAPTER 3

The Velocity Dispersion in Molecular Clouds

The origin of the velocity dispersion in molecular clouds, and in particular the Larson (Larson, 1981) scaling law is one of the longstanding issues in star formation. This chapter starts by examining the velocity line-width relation in molecular clouds and the possible explanations for molecular cloud turbulence. Recently, Bonnell et al. (2006) have proposed that supersonic velocity motions are induced in clumpy gas as it passes through a spiral shock. Furthermore the velocity dispersion is found to vary with size scale as $\sigma \propto r^{0.5}$, similar to observational results.

Before examining molecular cloud formation on galactic scales (Chapters 4,5,6), this chapter discusses the velocity dispersion in shocked gas. The analysis presented here extends that of Bonnell et al. (2006) by considering the dependence of the velocity dispersion on different gas distributions. Both numerical and analytical results are included, mainly for linear shocks, which are a more controlled means of modelling a spiral arm shock than using a section of a galactic disk. The distributions used are uniform, clumpy and fractal gas, the first as a test case, and the latter to represent the structure of the ISM. The velocity dispersion relation is calculated and compared for the different gas distributions.

3.1 Turbulence and structure in molecular clouds

As briefly mentioned in Chapter 1, molecular clouds are understood to be both turbulent and highly structured. The width of observed line profiles have indicated that supersonic velocities are present in molecular clouds (Heyer & Brunt, 2004; Ossenkopf & Mac Low, 2002; Falgarone & Phillips, 1990; Perault et al., 1985; Hayashi et al., 1989; Larson, 1981). These dynamics are further believed to control star formation and determine the properties of protostellar cores (Mac Low & Klessen, 2004). Although referred to as 'turbulence', the origin and nature of these motions are not fully understood. The most general definition of ISM turbulence is simply that the gas exhibits random motions on many scales (Mac Low & Klessen, 2004). However there is a consistent correlation observed in molecular clouds between the velocity dispersion and size scale (the Larson (1981) relation), approximately $\sigma \propto r^{0.5}$ (e.g. Myers (1983); Solomon et al. (1987); Brunt (2003)). This has invoked many comparisons between interstellar turbulence and classical turbulence, e.g. Kolmorogov incompressible turbulence (Passot et al., 1988; Falgarone & Phillips, 1990) ($\sigma \propto L^{0.33}$); Burger's shock dominated turbulence (Scalo et al., 1998) ($\sigma \propto L^{0.5}$); and the She-Leveque

model for incompressible turbulence (She & Leveque, 1994; Boldyrev, 2002) ($\sigma \propto L^{0.42}$ (Boldyrev et al., 2002)).

The possible sources of turbulence can be summarised as follows (see Mac Low & Klessen (2004),Elmegreen & Scalo (2004) and references therein): gravitational, magnetic or hydromagnetic instabilities; galactic rotation, through magneto-rotational instabilities, shocks in spiral arms or collisions of clouds on different epicyclic orbits; stellar feedback via supernovae, stellar winds and HII regions. Recent simulations have indicated that turbulence induced by a large scale driving force (e.g. large scale flows from supernovae or galactic rotation) is more consistent with observed molecular cloud structures (Brunt, 2003; Klessen & Burkert, 2001). Supernovae have been shown to produce sufficient energy to generate the velocity dispersions observed (Mac Low & Klessen, 2004). However observations of turbulent velocities in regions which do not contain massive star formation suggests that magneto-rotational instabilities (Piontek & Ostriker, 2005; Sellwood & Balbus, 1999) and colliding flows (Ballesteros-Paredes et al., 1999) may also be important. Interestingly, recent observations have suggested that the elongations of molecular clouds are more compatible with galactic rotation models rather than stellar feedback (Koda et al., 2006).

Galactic disk simulations have investigated gravity driven turbulence (Wada et al., 2002), stellar feedback (Wada & Norman, 2001; de Avillez & Breitschwerdt, 2005; Dib et al., 2006) and the influence of spiral density waves on ISM dynamics (Chapter 4). Analytical results also indicate that vorticity is generated in centrally condensed clouds subject to galactic shocks (Kornreich & Scalo, 2000), and the induced velocities follow the observed velocity size-scale relation. Previous numerical work on colliding flows showed that density and velocity perturbations occur even in uniform flows subject to cooling instabilities (Heitsch et al., 2005), although a velocity length scale correlation was not investigated. Simulations of clumpy flows have also indicated that a Salpeter type clump mass spectrum can be reproduced (Clark & Bonnell, 2006). Spiral shocks have also been proposed to explain the dynamics of molecular clouds (Bonnell et al., 2006; Zhang et al., 2001). Bonnell et al. (2006) model giant molecular cloud formation as gas passes through a clumpy spiral shock. The dynamics of the molecular clouds are determined on all scales simultaneously as the clouds form and the induced velocity dispersion size scale relation is consistent with observations. This can account for the observed velocity dispersions that are found even in regions devoid of massive stars. Furthermore, there is no need for a continuous driving mechanism as the time for the decay of these velocities is proposed to be of similar magnitude to the cloud lifetime.

It is well known that the ISM is highly structured (Cox, 2005; Elmegreen & Scalo, 2004; Dickey & Lockman, 1990; Perault et al., 1985). There are 2 current views as to the nature of the ISM, and in particular molecular clouds. Molecular clouds can be considered as discrete clumps in an inhomogeneous ISM, or the regions of highest density in a fractal distribution (see review by Williams et al. (2000) and references therein). In the first scenario, the molecular clouds are surrounded by some interclump medium, either low density molecular (Blitz & Stark, 1986; Aalto et al., 1998) or HI (Blitz, 1993) gas. The fractal description arises from the apparent self-similar nature of the ISM, in particular observations of a clump mass spectrum which is consistent over many scales. As noted in Chapter 1, the mass of molecular clouds, and clumps within molecular clouds follow a scaling law, $dN/dM \propto M^{-\beta}$. For example for molecular clouds in the inner Galaxy

$\beta = 1.5 - 1.8$ (Solomon & Rivolo, 1989). The realtion is slightly steeper for cloud clumps, $\beta = 1.8 - 2.2$ (Williams et al., 1995), and star forming cores, e.g. $\beta \sim 2.1$ (Testi & Sargent, 1998).

Since both the velocities and mass follow scaling laws, it is natural to suppose that turbulence and the mass spectra of clouds/clumps are related (Falgarone et al., 1991; Passot et al., 1988). The usual view is that the structure observed in molecular clouds is produced by the turbulent gas motions (e.g. Falgarone et al. 2005). This chapter (and Bonnell et al. 2006) instead proposes that turbulence arises from the inhomogeneity of the ISM, and that velocities are induced in non-uniform gas which is subject to a shock. The simulations predominantly model the passage of gas through a spiral arm by using a linear sinusoidal potential, although these results would apply generally to shocks between colliding flows e.g. from supernovae.

3.2 Numerical simulations of clumpy, fractal and uniform shocks

This section describes numerical results of both shock tube tests and shocks induced by a spiral potential. Predictions from analytical models are shown in Sections 3.2.6 and 3.3.

Although Chapter 2 suggested that using a variable viscosity and XSPH improve the results of shock tests, the simulations here use standard SPH. This is because XSPH is known to increase the velocity dispersion in the shock (Monaghan, 1992). Clearly for these results, any increase in the velocity dispersion due to errors in the SPH code needs to be minimised. The artificial viscosity parameters are also constant, using $\alpha = 1$ and $\beta = 2$ for the lower Mach numbers shocks but these were increased to $\alpha = 2$ and $\beta = 4$ for some of the tests. In all calculations, the gas is isothermal, non self-gravitating and there are no magnetic fields. These simulations are dimensionless, and are characterized by the Mach number of the shock and the initial density distribution of the gas. In all calculations, the particles are allocated velocities in the x direction only and, except for the oblique shocks (Section 3.2.5), the gas shocks in the yz plane.

The parameters used in the different simulations are shown in Table 3.1. There are 4 distributions of gas - uniform, homogeneous spherical clumps in pressure equilibrium, spherical clumps of different radii/density and fractal distributions. The filling factors for each distribution are calculated by overlaying a 3D grid on each distribution and determining the porosity. The filling factor is given by $F = N_{full}/N_{total}$ where N_{full} is the number of cells containing at least 1 particle and N_{total} the total number of cells. The filling factor varies with resolution of the grid, a 32^3 grid was selected since this gave a filling factor of almost 100% for the uniform distribution. The maximum initial scale length corresponds to the range of x values for the particles in the initial distribution. The slope of the resulting velocity dispersion relation (Section 3.2.4) is also shown, where $\sigma \propto r^{\alpha}$.

Sections 3.2.1 and 3.2.2 describe the initial conditions for shock tube tests and tests using a sinusoidal potential, and the results from these are shown in Sections 3.2.3, 3.2.4 and 3.2.5.

Test	Distribution	L	F (%)	$\mathcal{M}$	α
ST	Uniform	4	100	10	0.2
ST	Clumps (r_{cl}=0.1)	4	27	10	0.7
ST	Clumps (r_{cl}=0.2)	4	50	10	0.6
ST	Uniform	4	100	20	0.17
ST	Clumps (r_{cl}=0.1)	4	27	20	0.5
ST	Clumps (r_{cl}=0.2)	4	50	20	0.42
SP	Uniform	3	100	30	0.16
SP	Clumps (r_{cl}=0.1)	3	12	30	0.43
SP	Clumps (r_{cl}=0.2)	3	23	30	0.32
SP	Clumps (r_{cl}=0.4, 0.1, 0.04)	3	32	30	0.75
SP	2.2 D Fractal	3	10	30	0.4
SP	2.7 D Fractal	3	23	30	0.29

Table 3.1: Table showing the different runs performed and the distributions of gas used for initial conditions. ST and SP refer to shock tube and sinusoidal potential tests, L is the maximum initial length scale, F the volume filling factor and $\mathcal{M}$ the Mach number of the shock. The slope of the velocity dispersion relation (Section 3.2.4) is given by α, where $\sigma \propto r^{\alpha}$. All simulations used 2×10^5 particles except for the fractal distributions which required either 2×10^6 or 3×10^6 particles.

3.2.1 Shock tube test

3D shock tube tests were performed with initial distributions of uniform and clumpy gas to model colliding flows. For both distributions, particles were placed within a cuboid of dimensions $-2 < x < 2$, $-1 < y < 1$ and $-1 < z < 1$. To produce a clumpy shock,the particles were distributed in uniform density spheres within these length scales. To ensure that the gas is in pressure equilibrium prior to entering the shock, constant pressure boundaries are applied. The clumps are initially allowed to settle into equilibrium before the simulation is carried out. To produce clumps of different radii, the external pressure can be increased or decreased. The particles are then assigned a velocity of $v_0 = 10\ c_s$ for $x \leq 0$ and $v_0 = -10\ c_s$ for $x > 0$. When a steady state is reached, two Mach 10 shocks are produced. These calculations were also repeated with $v_0 = \pm 20\ c_s$ and all tests use 2×10^5 particles.

3.2.2 Sinusoidal potential

The calculations in Section 3.2 mainly consider shocks in gas subject to an external potential. In this case the gas self shocks, similar to gas experiencing a stellar potential in a spiral galaxy. A velocity dispersion relation similar to the observed $\sigma \propto r^{0.5}$ law has been shown to develop as gas passes through a clumpy spiral shock (Bonnell et al., 2006). Here a simpler problem is considered, which does not include shearing of the gas through a spiral arm, to investigate the effect of the shock dynamics on the initial gas distribution. Instead of the spiral potential, a 1D sinusoidal potential is applied of the form

$$\psi = A\cos(k(x + B)). \tag{3.1}$$

where k is the wavenumber and B a length parameter to determine the location of the minimum. This is equivalent to the linear passage of gas through sinusoidal spiral arms. The dimensionless velocity acquired by gas falling from the peak to the base of the potential is $V_{pot} = \sqrt{2 \times A}$. Several different potentials were tested, varying A and k, and only applying the potential once the gas has passed a minimum. However the results presented here are largely independent of the exact nature of the potential. The structure of the shock is similar for different potentials for a given initial distribution. The relative strength of the shock determines the magnitude of the velocity dispersion, whilst the initial distribution determines the velocity size scaling law. For the simulations presented here, $k = \pi/4$, $A = 100$ and $B = 2$, which produces a minimum at 2 and maxmima at -2 and 6.

For the sinusoidal potential simulations, particles are assigned a velocity of 50 c_s in the x direction and zero velocity in the y and z direction. This produces a shock of Mach number ≈ 30. A distribution of spherical clumps in pressure equilibrium is set up in the same way as described for the shock tube tests. A test is also carried out with a distribution with clumps of different size-scales and densities, giving structure on a range of scales. The clumps have initial diameters of 0.4, 0.1 and 0.04, with clumps of smaller diameter placed inside larger clumps. For the uniform and clumpy distributions, particles are positioned within a cuboid of dimensions $-1.5 < x < 1.5$, $-1 < y < 1$ and $-1 < z < 1$. Shocks are also examined with an initial fractal distribution. The method described in Elmegreen (1997) is used to generate fractals. The algorithm includes 3 parameters, an intrinsic length scale L, the number of hierarchical levels, H, and the number of points in each level, N. The dimension of the fractal is $D = logN/logL$ and the number of points is N^H. Two fractal distributions are used, for a 2.2 D fractal, with $L = 2.1$, $N = 5$ and $H = 9$ requiring ≈ 2 million points, and a 2.7 D fractal, with $L = 2.5$, $N = 12$ and $H = 6$ requiring ≈ 3 million points. The x, y, z coordinates are then scaled (equally) so each fractal fits inside a cube of dimensions $-1.5 < x < 1.5$, $-1.5 < y < 1.5$ and $-1.5 < z < 1.5$. The estimated fractal dimension of the interstellar medium is D=2.3, based on the cloud size and mass spectra found from observations (Elmegreen, 1996).

Since for the distributions with fractals or different size clumps the gas exhibits different densities and pressures, constant pressure boundaries are no longer appropriate. Instead a pressure switch is used in order that only gas in the shocked region is subject to pressure forces. The gas experiences pressure only when $div(v) \leq 0$ i.e. compression of the gas is occurring. This enables structure on all scales to be maintained in the gas distribution before gas reaches the shock. Tests for the uniform density clumps showed this method produced similar results compared to when constant pressure boundaries were applied.

3.2.3 Morphology of the shocks

Column density plots for different simulations are shown in Figures 3.1,3.2,3.3 (all for the sinusoidal potential tests). The uniform shock in Figure 3.1 shows a smooth shocked region of approximately constant density and width. By contrast the clumpy shock (Figure 3.1, lower) shows a much broader shocked region of non-uniform density. The shock contains more structure and appears more similar to simulations of turbulence. The distribution of different size clumps shows similar behaviour, although more smaller scale structure

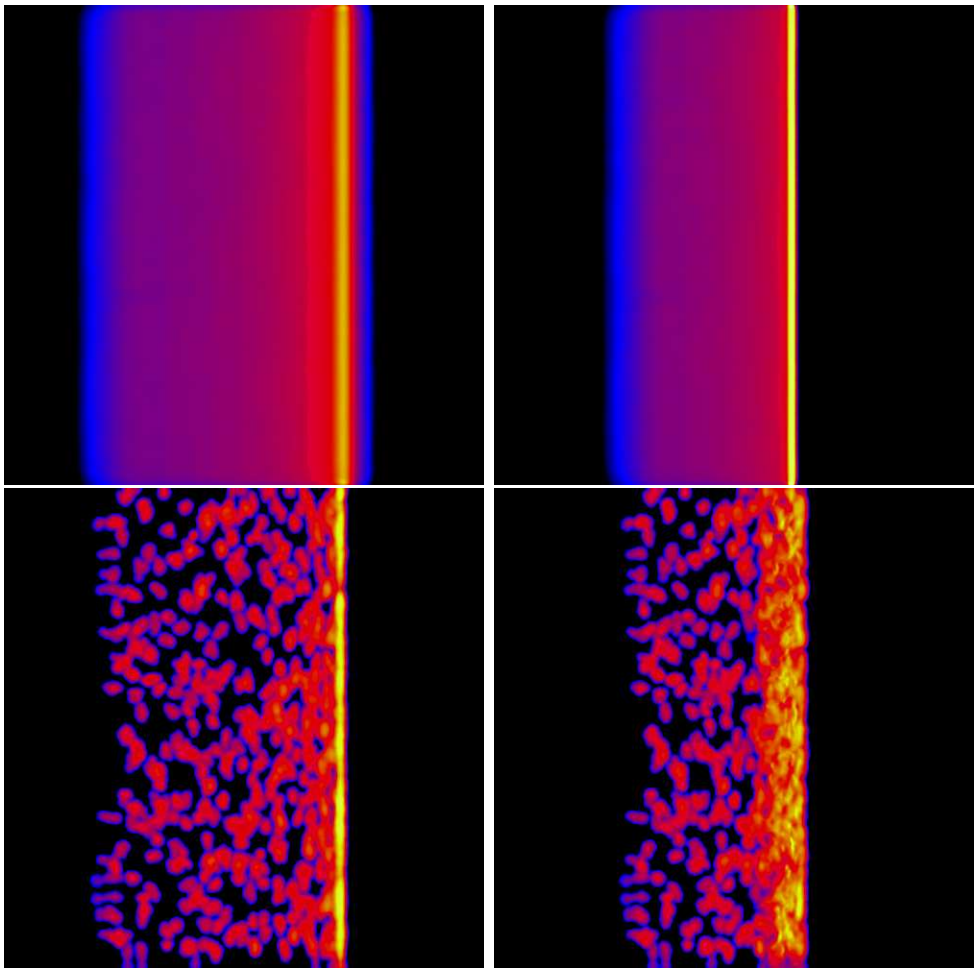

Figure 3.1: The column density distribution is shown for linear shock tests where gas is passed through a sinusoidal potential. The initial distribution is uniform (top) and clumpy (bottom, where the clump radius is 0.1). The left panels ($2.8 < x < 4.8, -1 < y < 1$) show the gas as it begins to shock (t=0.15) while the right panels ($3.2 < x < 5.2, -1 < y < 1$) show the gas when the shock is fully developed (t=0.25). The minimum and maximum of the potential lie at $x = 2$ and $x = 6$ respectively. The logarithmic column density ranges form 90 to 9×10^6, in units of particles per unit area.

is apparent in the shocked gas (Figure 3.2). The shocked gas of the fractal distribution (Figure 3.3) shows more filamentary structure compared to the clumpy distributions.

3.2.4 Velocity dispersion

The 1D velocity dispersion of the post-shock gas is calculated for the different shock simulations. Only the v_x velocities are considered, which correspond to the direction of motion of the initial gas, since the velocity dispersion in the y and z directions are always subsonic. For a given size, the velocity dispersion is averaged over numerous regions of that size scale. The regions are 3-D and chosen to centre on the densest particles in the shock. Only particles with densities greater than the maximum pre-shock density are considered for calculating the velocity dispersion, thus ensuring only gas in the shock is included.

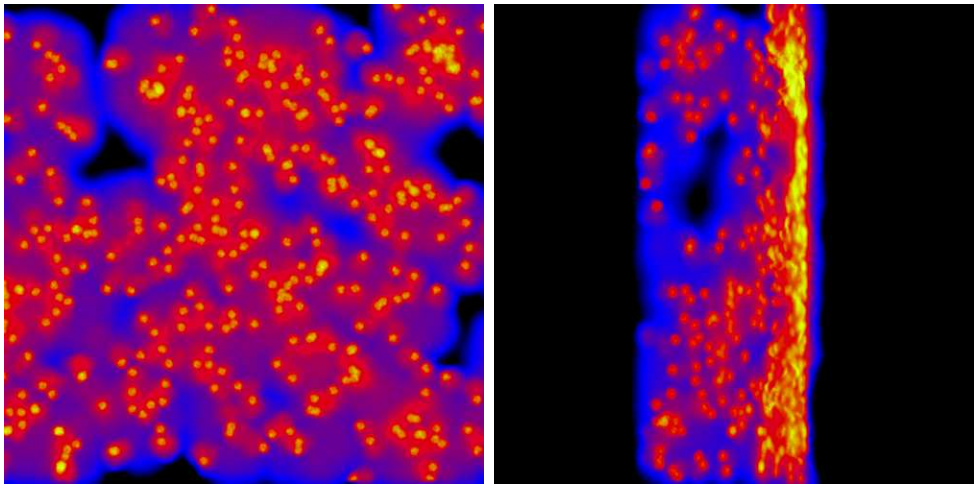

Figure 3.2: The column density distribution is shown for a shock test where the initial distribution consists of different radii clumps. The gas shocks as it passes through a sinusoidal potential. The left panel ($-1 < x < 1$, $-1 < y < 1$) shows the initial gas distribution (t=0) while the right panel ($3.2 < x < 5.2$, $-1 < y < 1$) shows a stage (t=0.25) during the shock. The scaling is the same as Figure 3.1, and the minimum and maximum of the potential lie at $x = 2$ and $x = 6$.

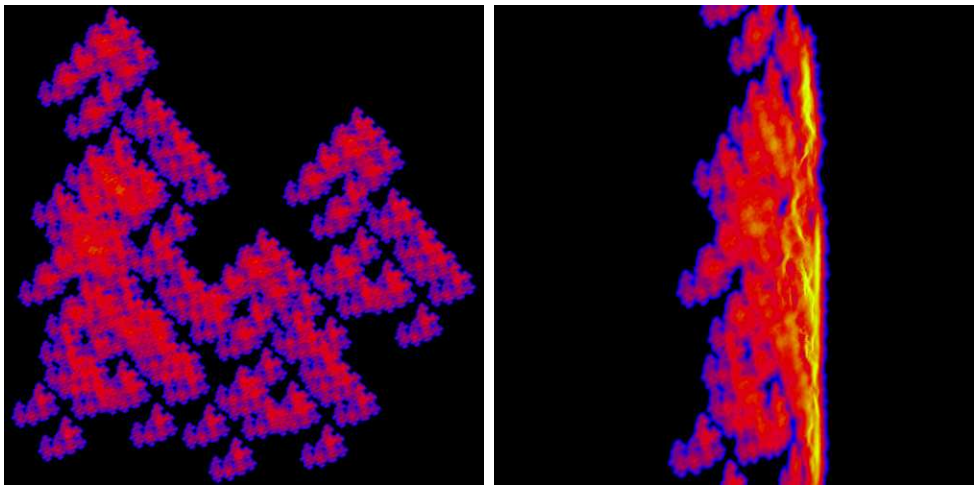

Figure 3.3: The column density distribution is shown for a shock test where gas distributed according to a 2.2D fractal is passed through a sinusoidal potential. The left panel ($-1.5 < x < 1.5$, $-1.5 < y < 1.5$) shows the initial gas distribution (t=0) while the right panel ($3.2 < x < 5.2$, $-1 < y < 1$) shows a stage (t=0.25) during the shock. The scaling is the same as Figure 3.1.

(Even for a uniform shock, including the pre shock gas will produce a Larson type velocity dispersion size-scale relation.) This process is repeated for regions of different size-scale to determine the dependence of the induced velocity dispersions on the size-scale.

For the shock tube tests, the velocity dispersion was found to be supersonic, even for the uniform shock with the standard viscosity parameters $\alpha = 1$ and $\beta = 2$. Increasing the viscosity parameters to $\alpha = 2$ and $\beta = 4$ lowered the values of the velocity dispersion for both the Mach 10 and Mach 20 shocks, although the velocity dispersion is still supersonic for the Mach 20 shock. The results presented for the shock tube tests use the higher viscosity parameters, whilst for the sinusoidal potential tests, there is less noise and the standard parameters $\alpha = 1$ and $\beta = 2$ are used. In all cases the higher viscosity parameters had little effect on the velocity dispersions for the clumpy shocks.

The velocity dispersion size-scale relation for each of the simulations are shown in Figures 3.4, 3.5, 3.6 and 3.7. Also shown is the $\sigma \propto r^{0.5}$ relation, coinciding with most observational results. In Figure 3.4 and 3.5, the velocity size-scale relation is plotted for uniform and clumpy initial gas distributions, for the shock tube test and the sinusoidal potential. For the sinusoidal potential, the velocity dispersion for the uniform shock dispersion remains flat and subsonic (the sound speed in all simulations is 0.3). This is as expected, since for a uniform shock, the velocity of the shocked gas should have zero velocity dispersion. Again for the shock tube tests, the velocity dispersions for the uniform shocks are relatively flat. By contrast the clumpy shocks show an increasing velocity dispersion with size-scale. The velocity of gas in the shock depends on the amount of mass it has encountered (Section 3.2.6). For the clumpy shock, gas entering the shock will encounter different amounts of mass (e.g. where gas approaches another clump, or alternatively a relatively empty area) and a range of velocities are exhibited by the shocked gas. This range of velocities increases as the size-scale of the region increases. At some size-scale, the region of gas will contain the full range of structure inherent in the initial distribution. The velocity size-scale relation then remains relatively flat for any further increase in size-scale.

In reality, the ISM has structure on many different length scales. To explore how this affects the resulting velocity dispersion, further simulations used a range of clump sizes and initially fractal distributions. Figure 3.6 and 3.7 also show an increasing velocity size-scale relation for initial gas distributions exhibiting structure on a range of scales. Figure 3.6 shows the velocity size-scale dependence where the initial distribution consists of different sized clumps, and Figure 3.7 the initial fractal distributions. The velocity dispersion extends to smaller scales due to the presence of structure initially over these scales. The velocity size-scale relation is similar to the observed relation $\sigma \propto r^{0.5}$ for most of the results in Figure 3.4, 3.5, 3.6 and 3.7 corresponding to non-uniform initial distributions. The exponent α, where $\sigma \propto r^{\alpha}$, varies from approximately 0.29 for the 2.7D fractal distribution to 0.75 for the distribution with different clump sizes. With the exception of the $\alpha = 0.75$ result, our results lie within the observed range of values e.g. $\alpha = 0.5 \pm 0.05$ (Solomon et al., 1987; Dame et al., 1986), $\alpha = 0.4 \pm 0.1$, $\alpha = 0.65 \pm 0.08$ (Fuller & Myers, 1992), $\alpha = 0.2, 0.5$ (Goodman et al., 1998), representing a range of size scales from cloud cores to molecular clouds.

Generally the distributions with higher filling factors produce shallower gradients in the velocity dispersion relation. As the filling factor increases, the distributions and

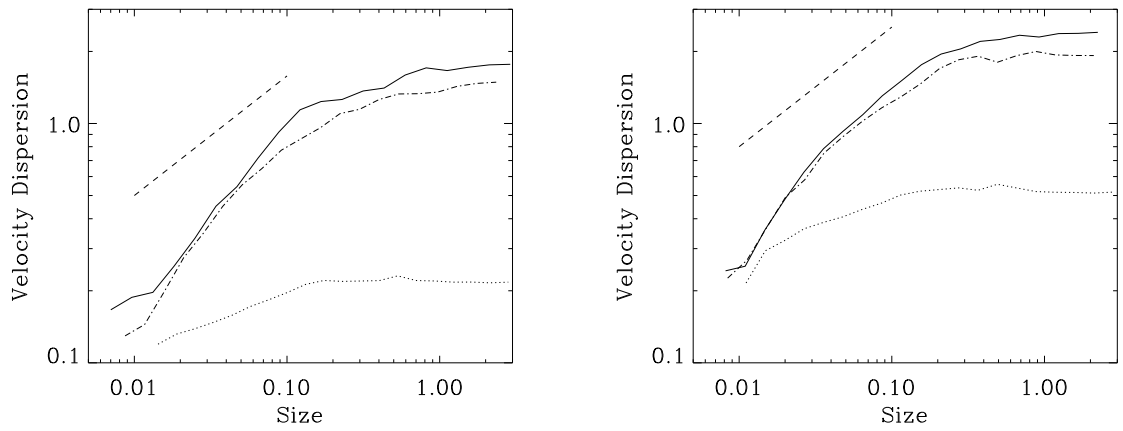

Figure 3.4: The one-dimensional velocity dispersion of the post-shock gas is plotted against size-scale for the 3D shock tube test. The figures show a $\mathcal{M}$=20 shock (left) and $\mathcal{M}$=40 shock (right). The initial distributions prior to the shock are uniform (dotted line), clumps of radii 0.1 (solid line) and clumps of radii 0.2 (dash-dot line). The dashed line represents the observed $\sigma \propto r^{0.5}$ relation and the sound speed is 0.3. The initial distribution has a maximum spatial extent of 4, and the viscosity parameters $\alpha = 2$ and $\beta = 4$ are used.

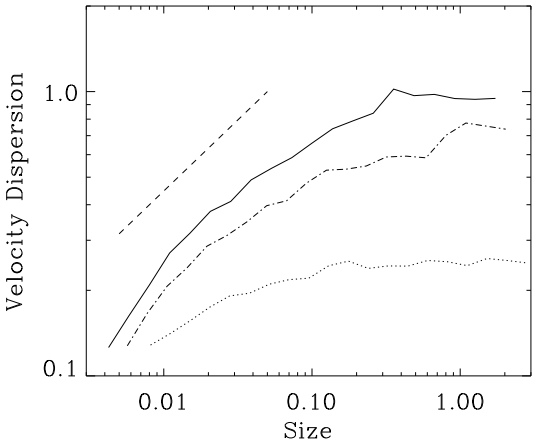

Figure 3.5: This figure shows the one-dimensional velocity dispersion of the post-shock gas plotted against size-scale for the sinusoidal potential. The initial distributions prior to the shock are the same as Figure 3.4, with the same key although the maximum initial length scale is 3 for these distributions. The dashed line shows $\sigma \propto r^{0.5}$ and the sound speed is 0.3.

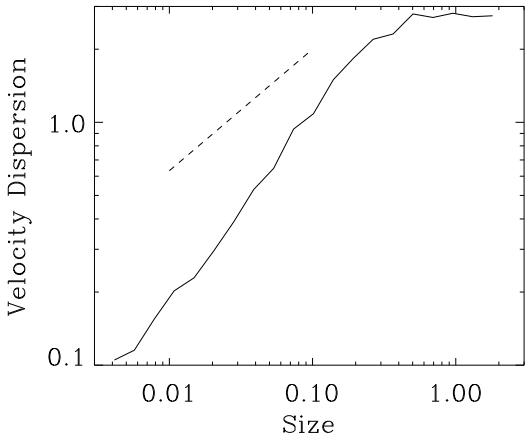

Figure 3.6: The 1D velocity dispersion dependence on size-scale is plotted for post-shock gas using an initial distribution of different size clumps. The maximum initial length scale is 3 and the gas shocks when passed through a sinusoidal potential. The dashed line shows $\sigma \propto r^{0.5}$ and the sound speed is 0.3.

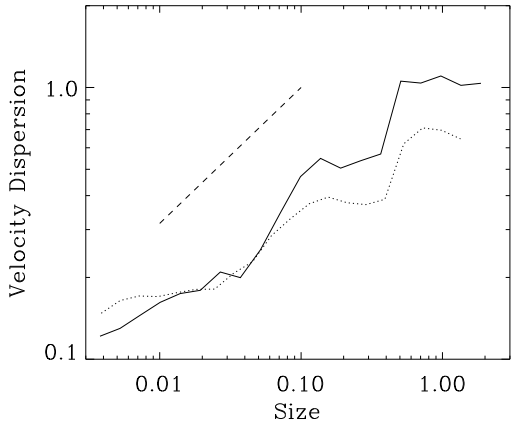

Figure 3.7: The 1D velocity dispersion dependence on size-scale is plotted for post-shock gas where the initial distributions are a 2.2D (solid) and 2.7 D (dotted) fractal. The gas is passed through a sinusoidal potential and the maximum spatial extent of the initial fractals is 3. The dashed line show $\sigma \propto r^{0.5}$ and the sound speed is 0.3.

subsequent velocity dispersions tend towards those of uniform gas, and subsequently the maximum velocity dispersion is less supersonic. The exception appears to be the distribution of different sized clumps, where the velocity size scale relation is somewhat steeper, probably because the filling factor of the smaller clumps is lower, and the smaller clumps contain most of the mass.

3.2.5 Oblique shocks

Due to the geometry of the shock, the velocity dispersion relations shown in the previous section have only used the v_x component of the velocity. A more general case is examined by modifying Equation (1) to include a dependence on y. This produces an oblique shock, more similar to spiral shocks. The potential is still sinusoidal, but the minima of the potential now lie in planes inclined by an angle θ to the yz plane. This is equivalent to an inclination of $90^o - \theta$ with the initial flow of the gas. A shock test is performed with this modified potential using the clumpy (r_{cl}=0.1) initial distribution. The gas column density for the shock is shown in Figure 3.8. The shock is found to induce a velocity dispersion in both v_x and v_y although the v_z dispersion is still subsonic. In Figure 3.9, the velocity dispersion is displayed for v_x and v_y, where the shock is inclined at $\theta = 45^o$ and 30^o. The magnitude of the v_x and v_y dispersions is then proportional to the component of the shock front perpendicular to these directions, i.e.

$$\frac{\sigma_x}{\sigma_y} = \frac{max(|\sigma| \cos\theta, c_s)}{max(|\sigma| \sin\theta, c_s)} \tag{3.2}$$

for a given size scale. The term c_s is an estimate of the minimum value of the dispersion, along the line of sight parallel to the shock (though as shown next in Figure 3.10, the minimum velocity dispersion in these simulations is slightly lower than c_s).

In Figure 3.10, the velocity dispersion is displayed along the line of sight for different viewing angles, again for the 30^o and 45^o oblique shocks. The maximum velocity

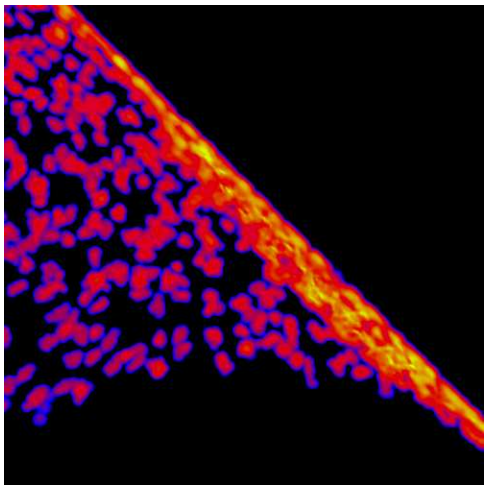

Figure 3.8: The column density distribution is shown for an oblique shock where the shock front is inclined at 45^o to the y axis. The gas initially has a clumpy (r_{cl}=0.1) distribution and is passed through a sinusoidal potential. The figure ($2.6 < x < 4.6$, $-0.8 < y < 1.8$) shows a stage (t=0.2) during the shock, and the shock in this image lies half way between a potential minimum and the following maximum. The scaling is the same as Figure 3.1.

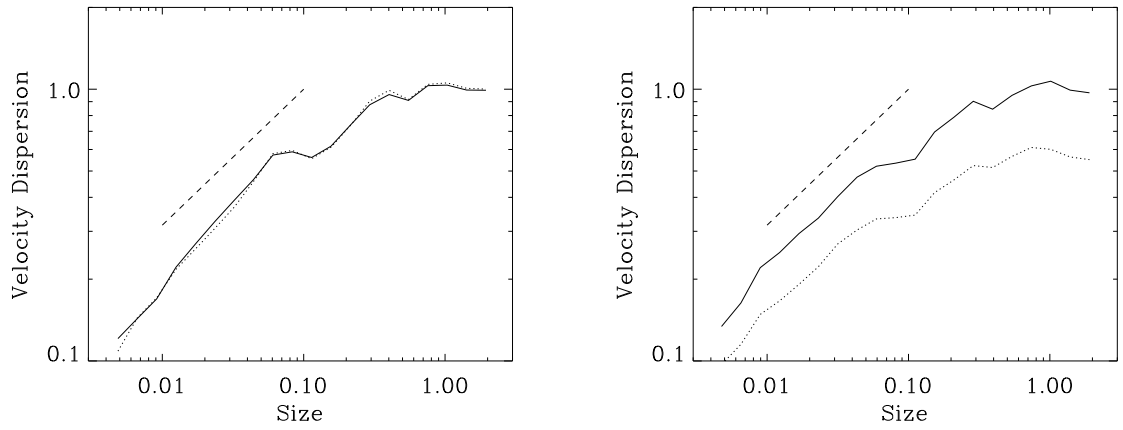

Figure 3.9: The v_x (solid) and v_y (dotted) velocity dispersions are plotted against size-scale for post-shock gas where the shock is inclined at 45^o (left) and 30^o (right) to the y axis. For $\theta = 45^o$, σ_x and σ_y are almost identical. The clumpy (r_{cl}=0.1) distribution is used, with a maximum initial length scale of 3. The gas shocks when passed through a sinusoidal potential. The dashed line shows $\sigma \propto r^{0.5}$ and the sound speed is 0.3.

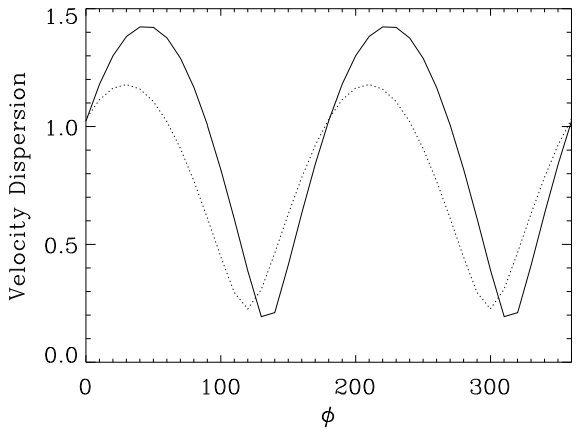

Figure 3.10: The maximum velocity dispersion along the line sight is plotted against viewing angle ϕ for the 45^o (solid) and 30^o (dotted) oblique shocks. The angle ϕ is measured anticlockwise from the $x > 0$ axis.

dispersion is chosen at each viewing angle, corresponding to a size scale of ~ 1 (c.f. Figure 3.9). The angle ϕ is measured anticlockwise from the $x > 0$ axis, with 10^o increments. The peaks then correspond to the line of sight perpendicular to the shock, whilst the minima occur when the line of sight is parallel to the shock. The difference in magnitude of the peaks occurs since the amplitude of the 45^o shock is stronger. From these results, some anisotropy is expected in the magnitude of the velocity dispersion of gas in molecular clouds, corresponding to the geometry of shocks in the gas. For classical models of turbulence, the magnitude of the velocity dispersion is unlikely to show any preferred direction.

3.2.6 Mass loading

This section discusses physically why an increasing velocity size-scale relation emerges in these models. For the clumpy shocks, the gas exhibits a range of densities and velocities across the region of shocked gas. The post-shock velocity of a small parcel of gas depends on the amount of mass it encounters during the shock ('mass loading'). If similar amounts of gas enter the shock, conservation of momentum determines that the velocity of the gas in the rest frame of the shock will be small. However, if gas entering the shock encounters only a small amount of material, it's velocity will be less affected and remain of higher magnitude.

Within a region of size-scale less than that of the internal structures in the gas, gas in that region will encounter a similar column density in the shock. Therefore the gas will exhibit a low velocity dispersion. However as the size-scale of the region increases, the region will include different structures and gas of different densities. Therefore different parcels of gas will encounter different amounts of mass and exhibit different post-shock velocities. Thus over a larger region a higher velocity dispersion occurs in the gas.

To test the hypothesis of mass-loading, a semi-analytical approach is also applied

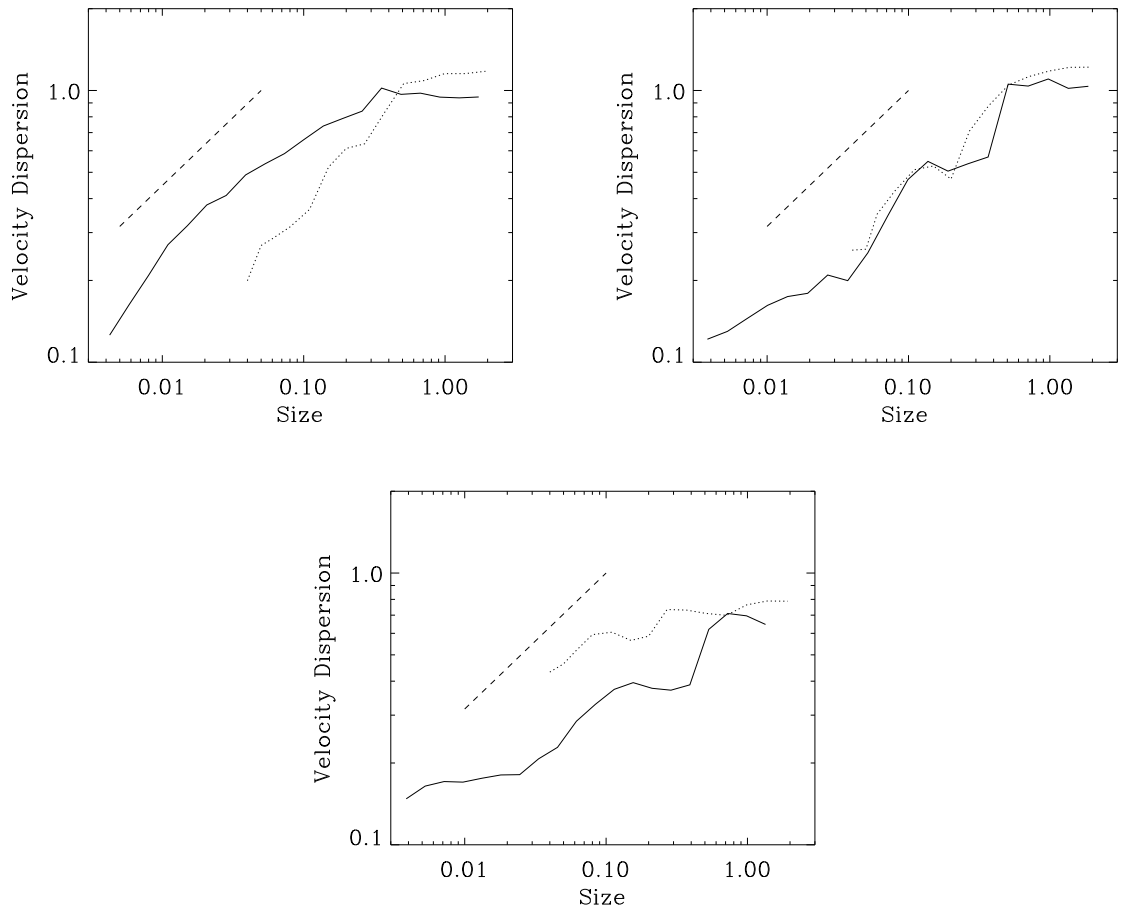

Figure 3.11: The dependence of the one-dimensional velocity dispersion of the post-shock gas on size-scale is plotted from our simulations (solid) (as in Figures 3.5 and 3.7) and the corresponding semi-analytical result (dotted). The semi-analytical result is calculated assuming the post-shock velocities are dependent on mass loading. Three different distributions are shown: clumpy (clump radii 0.1) (top left); 2.2D fractal (top right) and 2.7D fractal (bottom). The dashed line shows $\sigma \propto r^{0.5}$.

to calculate the velocity dispersion for the fractal and clumpy distributions. The initial distribution of particles is set up and a grid is positioned across the plane in which the shock will occur, at the centre of the distribution. For each grid cell, the mass of particles located within a distance l either side of the grid is calculated. By applying the conservation of momentum, the expected velocity of the gas entering each grid cell can be determined, assuming that all the gas within the width l of the centre is compressed into the shock. The width of mass included each side of the grid was l=0.2 for the clumpy shock and l=0.6 for the fractal distribution where more of the gas ends up in the shock (this parameter does not change the results providing sufficient material is included to accurately represent the gas distribution). The velocity dispersion was then calculated as described in Section 3.2.4.

In Figure 3.11 the velocity size-scale relation is plotted for the clumpy distribution (clumps of radius 0.1) and the 2 fractal distributions, from simulations and the corresponding semi-analytical tests. The results for the simulations are all taken from the sinusoidal

potential tests. For the clumpy distribution the slope determined from mass loading is somewhat steeper than the results from the simulation. The shape and gradient for the 2.2 D fractal shows a strong correlation between the simulation and the analytical result. For the 2.7D fractal, the semi-analytical velocity dispersion size relation is shallower than that determined by the simulation, although both show a shallower gradient compared to the other 2 distributions. The analytical method can be repeated by setting up distributions with different random seeds to show the degree of scatter in the expected gradients for the distributions. The clumpy shock, which should give very similar distributions regardless of the initial seed, produced a consistent slope of $\alpha = 0.48 \pm 0.03$ compared to $\alpha \approx 0.43$ for the simulation. The fractal distributions showed a much greater variation in slope, the 2.2D fractal giving $\alpha = 0.43 \pm 0.16$ compared to $\alpha \approx 0.4$ for the simulation. For the 2.7D fractal, $\alpha = 0.25 \pm 0.15$ for the analytical result, so the line shown on Figure 3.11 is at the lowest extent of this range, whilst $\alpha \approx 0.3$ for the simulation.

3.3 Analytical models

In this section, the velocity dispersion is determined analytically for collisions of clumps. The column density of gas from each clump entering the shock is calculated, and the resulting velocity of the post-shock gas determined from the conservation of momentum. The most simple case of two clumps colliding is investigated first (Section 3.3.1), as well as considering multiple collisions of clumps (Section 3.3.2).

3.3.1 Collision of two clumps

The previous results represented plausible mass distributions for the ISM, although consequently the velocity size-scale relation could only be determined numerically. Here the case of 2 clumps colliding is considered and the resulting velocity dispersion calculated directly. This distribution represents the 'least uniform' distribution, so the most removed scenario from a uniform shock. The clumps are assumed to be uniform density spheres and are travelling with equal and opposite velocities. The clumps are offset from each other and so do not collide head on. The parameters describing the collision are shown in Figure 3.12, where b is the impact parameter of the 2 clumps. In the following description, a Cartesian axis is assumed, centred on the point of maximum overlap between the 2 spheres, such that the centre of each sphere is situated at $y = \pm b/2$. In these coordinates, the collision of the clumps is symmetrical about $z = 0$. The initial velocity is $v_0 = 1$, and the column density is scaled so that maximum column density is $\Sigma_{max} = 1$ along the diameter of each sphere. First, the radii of the clumps are assumed to be the same, so $r_1 = 1$ and $r_2 = 1$.

To calculate the velocity dispersion, it is assumed that all the gas in the 2 clumps is compressed when they collide. The post-shock velocity of the material is found by determining, for each clump, the mass per unit area perpendicular to the shock ($\Sigma 1$ and $\Sigma 2$ in Figure 3.12). The calculation of the velocity dispersion is centred along the column which contains the most mass. In Figure 3.12, this corresponds to the column of gas at $y = 0$, $z = 0$ (i.e. the midpoint of b).

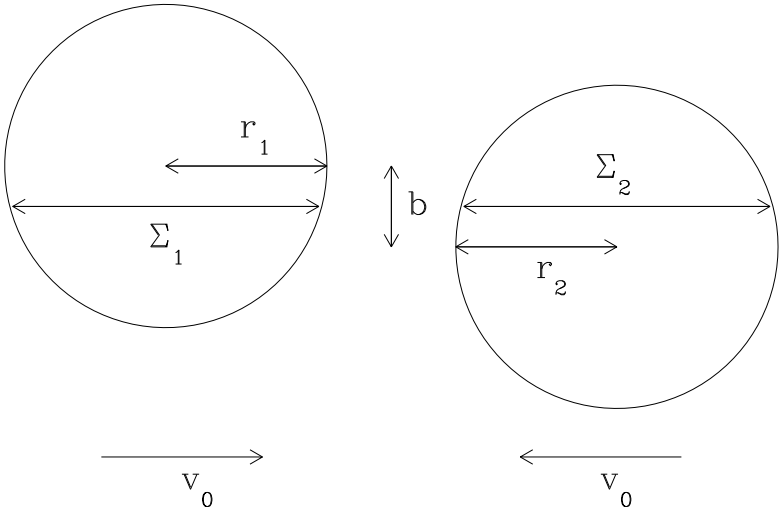

Figure 3.12: Diagram showing a collision with impact parameter b between 2 spheres. The column densities $\Sigma 1$ and $\Sigma 2$ perpendicular to the shock are calculated to determine the expected velocity of gas in the shock.

In Figure 3.13 the column density for each clump is plotted, as well as the post-shock velocity, for a cross-section of the collision along the y axis. By taking a cross-section, the problem is reduced to 1 dimension, and the mass for each sphere can be determined as a function of length scale. Using the idea of mass loading, all the gas is assumed to be compressed in the xy plane. The expected velocity of gas in the shock is calculated by applying the conservation of momentum, i.e.

$$v_s = \frac{(\Sigma 1 - \Sigma 2)v_0}{(\Sigma 1 + \Sigma 2)}. \tag{3.3}$$

In Figure 3.13, $b = 0.5$ and the 2 spheres are overlapping by a distance of 1.5. At $y = 0$ there is an equal contribution in mass from each sphere, and so the velocity in the shock will be 0. The velocity increases to ± 1 for gas which does not encounter any material from the other clump.

This idea is extended to calculate the velocity across a 2D shock from the collision of the clumps. Again the gas is assumed to be compressed in the yz plane and the column density entering the shock from each sphere is calculated. The expected post-shock velocity of the gas is calculated, again over the yz plane. The velocity dispersion is found over a disk centred on the co-ordinates $y = 0$, $z = 0$. The velocity dispersion is determined over disks of increasing radius, to produce a velocity size-scale relation. The mass-weighted velocity dispersion is shown in Figure 3.14, with collisions of different impact parameter.

For the simple case of 2 clumps colliding, the velocity dispersion increases with size scale approximately as a power law, independent of the impact parameter. Increasing the impact parameter transposes the power law to smaller size scales, since the size of the shocked region decreases. For size-scales $> r - b/2$, the velocity dispersion includes gas which does not enter the shock and the velocity size-scale relation flattens. The power law for the shocked gas is somewhat steeper than the $\sigma \propto r^{0.5}$ relation observed, rather $\sigma \propto r^1$. However, the power law exponent may be expected to decrease when considering larger regions and structure on multiple scales composed of many clumps (Section 3.3.2).

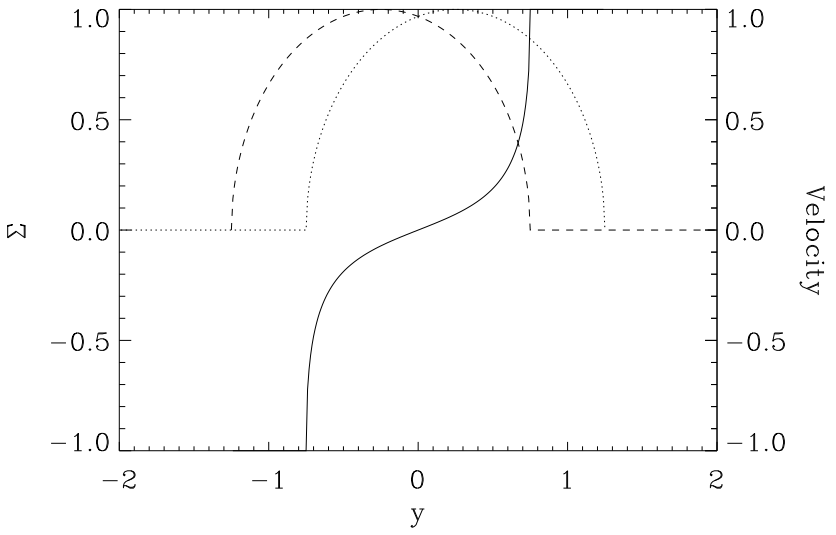

Figure 3.13: The velocity (solid line) is plotted for a cross-section of post-shock material when 2 spheres collide. The cross-section corresponds to taking a cut where $z = 0$. The dotted and dashed lines show the column density for each sphere along the cross-section.

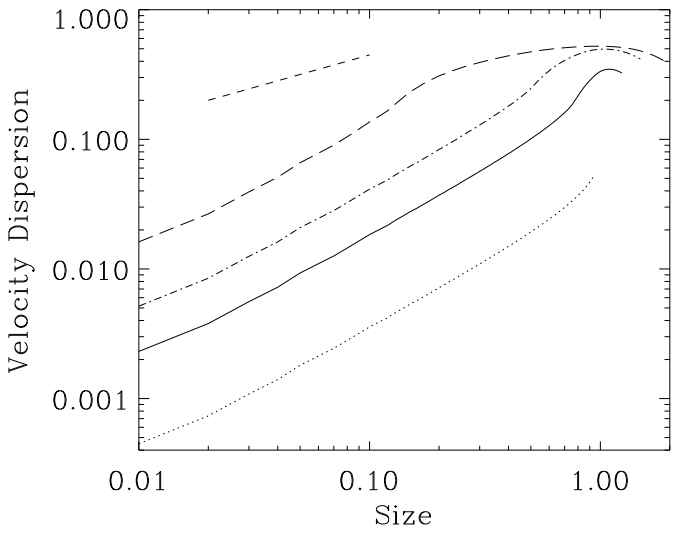

Figure 3.14: The mass-weighted velocity dispersion predicted for the collision of 2 spherical clumps, each of radii 1 and initially travelling at $v_0 = 1$. The impact parameters of the collision are $b = 0.1$ (dotted), $b = 0.5$ (solid), $b = 1$ (dot-dash) and $b = 1.75$ (long dash) whilst the short dash line represents $\sigma \propto r^{0.5}$.

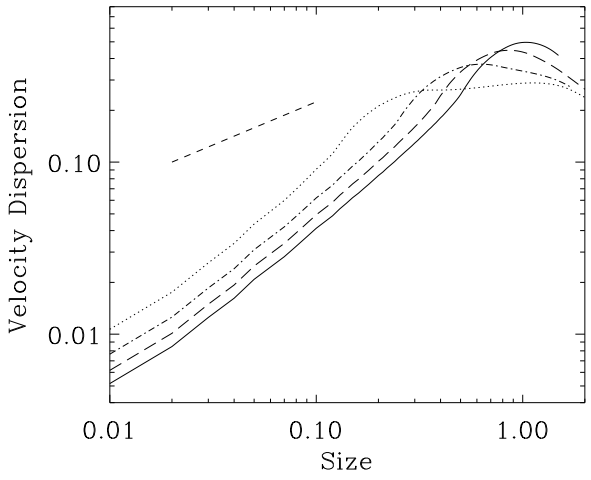

Figure 3.15: The mass-weighted velocity dispersion predicted for the collision of 2 spherical clumps travelling with initial velocity $v_0 = 1$. The radius of the first clump is set to 1, whilst the radius of the second clump is 1 (solid), 0.75 (long dashed), 0.5 (dot-dash) and 0.25 (dotted). The impact parameter for all the collisions is $b = 1$. The short dash line shows $\sigma \propto r^{0.5}$.

This power law is also independent of the comparative radii of the 2 spheres. Figure 3.15 shows the effect of varying the radius of the second clump (r_2). Similarly to varying the impact parameter, the velocity size-scale relation shifts to smaller scales as r_2 decreases, and levels off at size-scales comparable to r_2. Scaling both clump radii up or down will extend the velocity size-scale relation to larger or smaller size-scales. For example, if the radius decreases by a factor of 10, the column density and therefore mass-weighted velocity dispersion will also decrease by the same factor.

Assuming that the clumps have velocities $v_0 = 1$, the velocity dispersion for an impact parameter of $b \geq 0.5$ reaches a maximum of ~ 0.3. Since the initial velocity v can be scaled up or down, the maximum velocity dispersion for an initial velocity of $v_0 c_s$ will be approximately 0.3 $v_0 c_s$ (e.g. 3 c_s if $\mathcal{M} = 20$). When the impact parameter is small, the velocity dispersion is unlikely to be supersonic (e.g. the maximum is ~ 0.5 c_s when $b = 0.1$ and $\mathcal{M} = 20$). This is expected, since if $b = 0$ the clumps collide head on and the velocity dispersion is 0 everywhere.

3.3.2 Multiple collisions of clumps

The velocity size-scale relation obtained for 2 clumps colliding is somewhat steeper than those observed for molecular clouds. However this distribution of gas is an extreme case, as in general the gas would be comprised of multiple clumps of various sizes. This section considers many collisions of clumps and the average velocity dispersion is calculated at each size scale. In all the collisions, it is still supposed that 2 clumps collide, and the radius of the first clump is fixed to 1. However both the impact parameter b and the second clump radius, r_2, can be varied. Three different possibilities for the collision of clumps are shown in Figure 3.16, where r_2 varies randomly. The impact parameter is

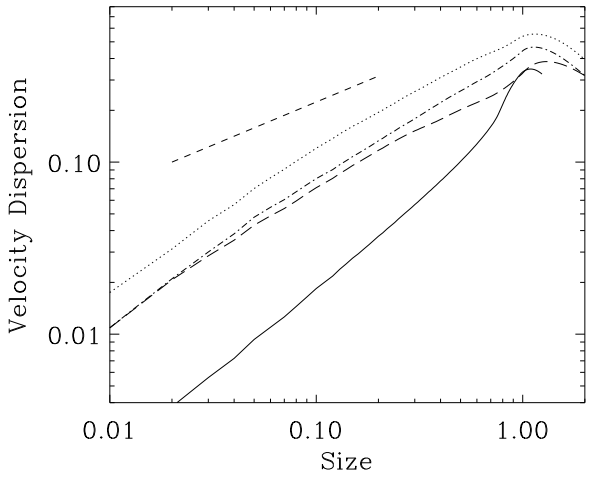

Figure 3.16: The mass-weighted velocity dispersion predicted for the collision of multiple spherical clumps. The solid line shows the velocity dispersion for 2 clumps of radii 1 and impact parameter 0.5. The dot-dash and dotted lines give the average velocity dispersion for multiple collisions of clumps, where all clumps are assumed to have radii of 1, but the impact parameter varies. The impact parameter is either random (dot-dash) or biased towards large b (dotted). The velocity dispersion for multiple collisions with both random b and r_2 is given by the long dashed line. The short dash line shows $\sigma \propto r^{0.5}$.

varied randomly, i.e. following a probabillity distribution of $f(b) = 1,\ 0 < b < 1$, and is biased towards large values ($f(b) = b,\ 0 < b < 1$). Without gravity, b should follow $f(b) = b^2$. For comparison, the velocity size-scale relation from 2 clumps colliding with impact parameter $b = 0.5$ (and both of radii 1) is also included.

The slope is shallower for multiple collisions of random b, giving $\sigma \propto r^{0.8}$. The velocity dispersion was also calculated with b biased towards large values, reflecting the probability of a collision relative to the impact parameter. This produces a slightly flatter slope, although it mainly increases the magnitude of the velocity dispersion. Finally, with both b and r_2 allowed to vary randomly, the gradient decreases further to $\sigma \propto r^{0.7}$.

This is still an incomplete model compared to the simulations of clumpy gas previously described, with further possible variations in the clump and shock geometry. Furthermore, collisions of multiple clumps have not been included, i.e. where > 2 clumps collide simultaneously, or 2 clumps collide with each other before colliding with further material in the shock. The latter is evident in the simulations, where layers of clumps enter the shock and interact with each other. This is again likely to produce a shallower relation compared with the calculations in this section. Overall, for the most structured distribution of 2 offset clumps colliding, the resulting velocity size-scale relation is steep, $\sigma \propto r^1$. For the least structured distribution, i.e. uniform gas, the velocity size-scale relation of the shock is flat. In reality, the distribution of gas, and therefore the gradient of the velocity size-scale relation, is likely to lie within these two extremes.

3.4 Summary

The results of this chapter support the conclusions of Bonnell et al. (2006), that shocks can induce a velocity dispersion size-scale relation in inhomogeneous gas, and thus account for the observed gas motions in molecular clouds. Simulations and analysis of shocks for initial distributions of uniform, clumpy and fractal gas have been presented here. For all these distributions except for the uniform shocks, an increasing velocity size scale relation occurs. For example, for a 2.2 D fractal distribution representative of the ISM, the velocity size-scale relation is approximately $\sigma \propto r^{0.4}$, in good agreement with observations. The slope of the velocity size-scale relation tends to decrease with distributions corresponding to higher filling factors. The velocity size-scale relations determined for these distributions can be understood in terms of mass loading, as indicated by analytical tests. Oblique shock tests show that the magnitude of the line-of sight velocity dispersion depends on the angle from which the shock is viewed, providing an observational test for this model.

These results imply that: 1) The observed multi-scale structure of the ISM may explain the velocity dispersion in molecular clouds. This is in contrast to the usual view that turbulence produces the structure of molecular clouds (e.g. Falgarone et al. (2005)); 2) In these models, the dynamics of the shocked gas corresponds to random velocities, rather than classical turbulence, despite the apparent velocity size scaling relation.

CHAPTER 4

Gas Dynamics in a Spiral Potential

The remaining chapters (4, 5 and 6) describe global simulations of a galactic disk in a spiral galaxy. The SPH particles in these simulations model a gaseous galactic disk, whilst the stellar component is included by a background potential. Without explicitly including stars, the gaseous part of the disk can be modelled at high resolution. The disadvantage though is that the gravitational forces between the stars and the gas are not treated self consistently. The potential used here contains components for both the stellar distribution, a spherical halo, and includes a density wave perturbation which concentrates the stellar mass into symmetric spiral arms. Grand design galaxies, where the spiral structure is thought to be due to density waves, represent a significant proportion of spiral galaxies. Observations indicate the presence of shocks in the spiral arms of these galaxies, as predicted from analysis of gas subject to a spiral potential (Roberts, 1969).

Even without including gravitational, magnetic or thermal instabilities, spiral shocks are potentially very significant to molecular cloud formation. They may form clouds in the spiral arms by modifying the gas dynamics and/or increasing the density to allow molecular gas formation (or the formation of GMCs from pre-existing molecular gas). A detailed description of the gas dynamics is included in this chapter, before the molecular gas content of the disk is analysed in Chapter 5. The results in this chapter show that spiral shocks are found to have a major influence on both the organization of structure in the spiral arms and the velocity dispersion of the gas. Furthermore, the interarm structure in the disk increases with time, leading to the formation of spurs perpendicular to the spiral arms. Spurs are common features of spiral galaxies, and this thesis (as well as recent observations of M51) suggests they may well be linked to molecular cloud formation in the spiral arms.

To summarise, this chapter discusses:

- Spiral density waves and gravitational potentials
- The possibility of triggered star formation by spiral shocks
- The initial conditions and an overview of simulations performed
- The dynamics of spiral shocks
- The formation of spurs

4.1 Spiral Galaxies

Spiral galaxies are diverse in their appearance, properties and structure. They can be classified as barred or unbarred, grand design or flocculent. Grand design galaxies, such as M51, contain clear, symmetric spiral arms which extend for at least 1 rotation of the disk. Typically grand design galaxies will exhibit a 2 or 4 armed spiral pattern. Flocculent galaxies, e.g. NGC4414, on the other hand contain multiple short spiral arms and are asymmetric. For isolated spiral galaxies, it is found (Elmegreen & Elmegreen, 1982) that approximately 30% of unbarred spirals are grand desfign, whilst $\sim 70\%$ of barred galaxies exhibit grand design spiral patterns. Galaxies located in groups or binaries are more likely to show grand design patterns.

The 3 most common theories used to explain spiral structure in galaxies are:

- Spiral density waves (Lin-Shu hypothesis)
- Shearing and swing amplification of gravitational instabilities
- Self propagating star formation

The Lin-Shu hypothesis (Lin & Shu, 1964) proposes that the orbits of stars are arranged into kinematic density waves. The spiral arms occur where the orbits are most closely aligned, and the stellar density increases. The density wave produces a perturbation over the entire galactic disk and a symmetric grand design pattern. The pattern is present in the underlying stellar population and is expected to be long lived. New generations of stars form as gas is compressed by the density perturbation (Roberts, 1969), and constitute a new spiral pattern of brighter stars. Density waves originate from instabilities in the disk, which may be induced by a companion galaxy or bar. By contrast, the shearing of gravitational instabilities in the stellar disk (Toomre, 1964; Goldreich & Lynden-Bell, 1965) or self propagating star formation (Mueller & Arnett, 1976; Gerola & Seiden, 1978) are expected to produce shorter spiral arms more typical of flocculent spiral galaxies. In these cases, star formation and the generation of spiral arms are simultaneous, and the spiral arms are not expected to survive multiple rotation periods.

The first indications for the presence of spiral density waves in galaxies came from observations of M81. Kinks in the radial velocity field from HI maps showed abrupt changes coincident with the spiral arms. These changes in velocity across the spiral arms, now termed streaming motions, showed deviations from a flat rotation curve, but could be accounted for by adding a density wave perturbation to the galactic potential (Rots, 1975; Visser, 1980a). Streaming motions of 50 - 80 km s^{-1} (i.e. the difference in velocity compared to a flat rotation curve) have since been observed in M51 (Vogel et al., 1988; Tilanus & Allen, 1991; Adler et al., 1992) as well as various other galaxies such as NGC3267 (Reuter et al., 1996). The streaming motions for M51 are the largest observed, which is not surprising considering M51 shows such remarkably clear spiral structure. Some galaxies, e.g. M31 (Loinard et al., 1999) with a less ordered spiral pattern, do not show streaming motions characteristic of spiral density waves. The difference is not clear cut though - in some apparently flocculent galaxies, the dust forms long symmetric arms (Seigar et al., 2005; Thornley & Mundy, 1997; Block et al., 1996), whilst self propagating star formation may contribute to flocculent structure in grand design galaxies (Elmegreen, 1979).

The simulations in this thesis model grand-design galaxies and follow the density wave scenario. The Lin-Shu hypothesis assumes that the spiral pattern is quasi-static and lasts for at least a few orbits. This allows an analytical time-independent potential to be obtained which describes the spiral perturbation to a galactic disk. It is unclear whether the spiral patterns in galaxies are this stable; recent results (Merrifield et al., 2006) suggest galaxies may start winding up even within one orbital period. A time-independent spiral potential is usually applied to numerical models of galactic disks (e.g. Patsis et al. (1997) Gómez & Cox (2002), Wada & Koda (2004), Gittins (2004)), since the gas distribution can be analysed in a steady state, and the long term morphology of spiral patterns is unknown. An alternative for modelling flocculent spiral galaxies is to use a time dependent potential from an N body simulation (Clarke & Gittins, 2006) or include both the stellar and gaseous components in calculations (Elmegreen & Thomasson, 1993; Bottema, 2003).

The next section shows how a general expression for a spiral perturbation can be determined from density wave theory, before describing the potential used for the simulations in this thesis.

4.2 Spiral Density Waves

The Lin-Shu hypothesis finds wave solutions for the surface density of the galactic disk. The disk is described by the fluid equations, where the density of the disk includes both the stellar and gaseous components of the galaxy. The velocity dispersion and any pressure-like forces in the disk are neglected here, and the disk is supposed to be infinitely thin. In cylindrical coordinates (r, θ, z) the equations describing the disk are

$$\frac{d\Sigma}{dt} + \frac{1}{r}\frac{d}{dr}\Big(r\Sigma v_r\Big) + \frac{1}{r}\frac{d}{d\theta}\Big(\Sigma v_\theta\Big) = 0 \tag{4.1}$$

$$\frac{dv_r}{dt} + v_r\frac{dv_r}{dr} + \frac{v_\theta}{r}\frac{dv_r}{d\theta} - \frac{v_\theta^2}{r} = \frac{d\phi}{dr} \tag{4.2}$$

$$\frac{dv_\theta}{dt} + v_r\frac{dv_\theta}{dr} + \frac{v_\theta}{r}\frac{dv_\theta}{d\theta} + \frac{v_\theta v_r}{r} = \frac{1}{r}\frac{d\phi}{d\theta} \tag{4.3}$$

with Poisson's equation

$$\frac{d^2\phi}{dr^2} + \frac{1}{r}\frac{d\phi}{dr} + \frac{1}{r^2}\frac{d^2\phi}{d\theta^2} + \frac{d^2\phi}{dz^2} = -4\pi G\Sigma\delta(z). \tag{4.4}$$

Σ is the surface density, ϕ is the gravitational potential and $\delta(z)$ is the Dirac delta function. In equilibrium $\Sigma = \Sigma_0(r)$, $v_r = 0$, $v_\theta = r\Omega(r)$ and $\phi = \phi_0$. Perturbations are taken about equilibrium so $\Sigma = \Sigma_0 + \Sigma'$, $v_r = v_r'$, $v_\theta = r\Omega + v_\theta'$ and $\phi = \phi_0 + \phi'$. The linearized equations allow solutions of the form

$$\begin{aligned}\Sigma' &= Re\Big(A(r)\exp[i\psi(r)]\exp[i(wt - n\theta)]\Big) \\ &= A(r)\exp^{iwt}\cos[wt - n\theta + \Psi(r)]\end{aligned} \tag{4.5}$$

and so the density can be described as a wave. If $A(r)$ varies slowly with r and $\Psi(r)$ varies quickly, then Equation 4.5 produces a spiral wave propagating through the disk. The potential corresponding to Equation 4.5 can be approximated by integrating Poisson's equation. This provides an analytical expression (Lin & Shu, 1964)

$$\phi(r, z) = C(r, z)\exp[F(r, z) - in\theta] \tag{4.6}$$

where C and F are found by applying suitable boundary conditions. However most models assume a general form for a spiral potential

$$\phi = A \sum_n \alpha_n cos(\chi_n) \tag{4.7}$$

where ϕ, A and χ_n may depend on r, θ and t. This expression sums over each spiral wave node of n spiral arms, each with amplitude α_n, e.g. if n takes values of 2 and 4 the potential contains both 2 and 4 arm spiral perturbations. The function A gives the overall amplitude of the spiral nodes, usually as a function of radius of the form $\exp[r - r_0]$ so the amplitude of all the spiral arms peaks at some radius r_0. The spiral pattern itself is given by

$$\chi_n = \Psi_n(r) - n(\theta - wt) \tag{4.8}$$

where w is the pattern speed and the function $\Psi_n(r)$ defines the shape of the arms. The standard form of Ψ is

$$\Psi_n = \pm \frac{n}{\tan i} \ln(r/r_0) \tag{4.9}$$

where i is the pitch angle, the angle between the arms and a circular orbit. This form is found to agree with observed spiral galaxies (Tully, 1974; Roberts et al., 1975; Visser, 1980b).

4.3 Galactic Potential

The previous section introduced a general potential which will produce a spiral density pattern. For the simulations in this thesis, a gravitational potential is used which includes 3 components, for the stellar disk, the spiral perturbation and outer halo. These potentials use the spiral morphology, mass distribution and rotation curve of the Milky Way as a basis. Gravitational feedback from the gas to the stellar disk is not included, however the transfer of angular momentum between the potential and the gas is possible (Section 4.7.1).

Disk potential

The disk is represented by a logarithmic potential which produces a flat rotation curve, e.g. Binney & Tremaine (1987),

$$\psi_{disk}(r, z) = \frac{1}{2} v_o^2 \log \left(r^2 + R_c^2 + \left(\frac{z}{q} \right)^2 \right). \tag{4.10}$$

The core halo radius is $R_c = 1$ kpc, $v_0 = 220$ km s^{-1} and $q = 0.7$ is a measure of the disk scale height.

Spherical Halo

The potential for the outer dark matter halo is solved from the density distribution

$$\nabla^2 \psi_{halo}(r) = -4\pi G \rho_{halo}(r), \qquad \rho_{halo}(r) = \frac{\rho_h}{1 + (r/r_h)^2} \tag{4.11}$$

where $\rho_h = 0.0137$ M$_\odot$ pc^{-3} is the halo density and $r_h = 7.8$ kpc is the halo radius (Caldwell & Ostriker, 1981).

Spiral perturbation

A spiral potential is taken from Cox & Gómez (2002):

$$\begin{aligned}
\psi_{sp}(r,\theta,t) &= -4\pi G H \rho_0 \exp\Big(-\frac{r-r_0}{R_s}\Big)\sum_{n=1}^{3}\frac{C_n}{K_n D_n}\cos(n\gamma) \\
\text{where}\quad \gamma &= N\Big[\theta - \Omega_p t - \frac{\ln(r/r_0)}{\tan(\alpha)}\Big], \\
K_n &= \frac{nN}{r\sin(\alpha)}, \\
D_n &= \frac{1+K_nH+0.3(K_nH)^2}{1+0.3K_nH}, \\
C(1) &= 8/3\pi, \quad C(2) = 1/2, \quad C(3) = 8/15\pi
\end{aligned} \tag{4.12}$$

The key parameters describing the spiral pattern are $N = 4$, the number of arms, $\Omega_p = 2 \times 10^{-8}$ rad yr^{-1} , the pattern speed, $\rho_0 = 1$ atom cm^{-3}, the amplitude and $\alpha = 15^o$, the pitch angle. The amplitude is equivalent to $\approx$ 200 km^2 s^{-2} which corresponds to a perturbation of 3 per cent to the disk potential and an increase of 20 km s^{-1} as gas falls from the top to the bottom of the potential well. The terms K_n, D_n, C_n and the exponential term determine the dependence of amplitude on radius. The radial parameters assumed are $r_0 = 8$ kpc, $R_s = 7$ kpc and $H = 0.18$ kpc. This potential is of the form of Equation 4.7 and consists of 3 spiral wave patterns. By comparison with Equation 4.7, the potential contains 4, 8 and 12 arm spiral nodes, but the amplitude of the 4 arm component is much larger. The overall form of the potential provides a roughly uniform density between the 4 spiral arms (Cox & Gómez, 2002).

The disk and spiral potential used for the models in this thesis is shown in Figure 4.1. The amplitude of the spiral potential has been multiplied by a factor of 10 so the perturbation is clearer.

4.3.1 Comparison with the Milky Way

The parameters for the spiral potential are chosen based on observations of the Milky Way, although there is considerable uncertainty in the values of these parameters. Furthermore, the Milky Way may be closer in structure to a flocculent spiral galaxy. However, the main aim of this thesis is to investigate spiral shocks rather than produce an accurate model of the Galaxy.

The Milky Way has been described as closest to either a 2 or 4 arm spiral galaxy. A review by Vallée (2005) shows that most results suggest the Milky Way has 4 spiral arms and a pitch angle of 15^o. The pattern speed suggested in Cox & Gómez (2002) produces a co-rotation radius of 11 kpc. The co-rotation radius is not easily determined, although recent literature suggests that co-rotation is nearer to 8 kpc (Mishurov & Zenina, 1999). Again for the purposes of this thesis, the priority is to investigate the shock without requiring a specific location of co-rotation. Also at co-rotation the gas does not shock, so including gas at co-rotation in these models is not useful at this stage.

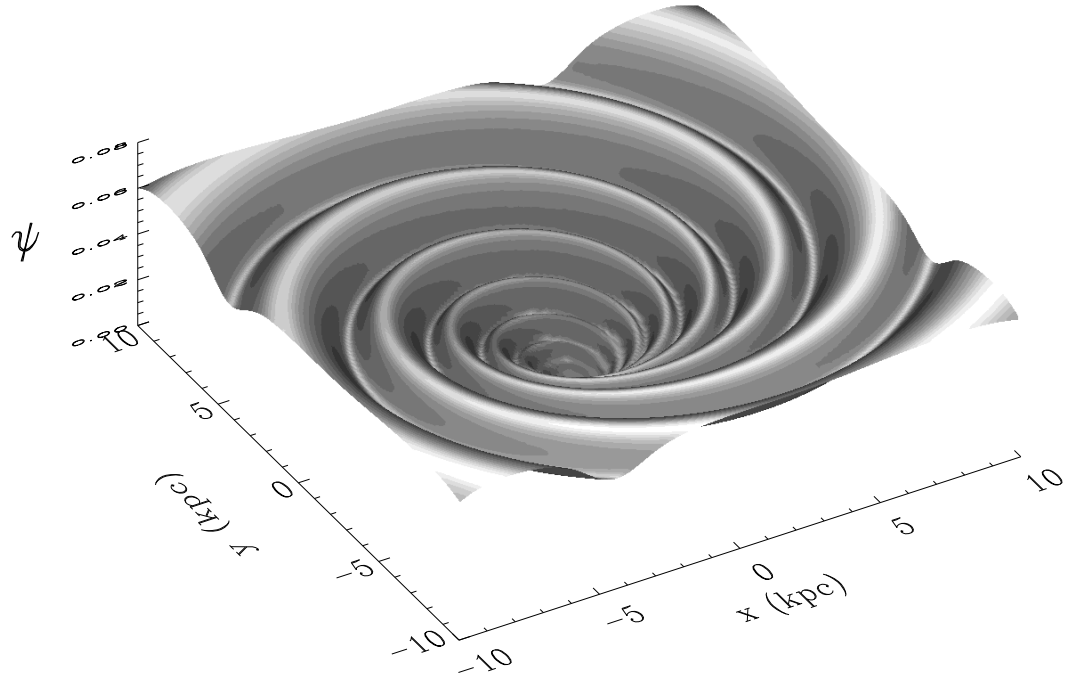

Figure 4.1: The sum of the spiral and disk potentials corresponding to equations 4.10 and 4.12. The spiral potential has been multiplied by a factor of 10 so that the perturbation is clearly visible.

4.4 Gas response to a spiral potential

The remainder of this thesis is concerned with the response of the ISM to the galactic potential described in the previous section. The response of gas to a spiral potential was considered analytically by Roberts (1969) and Shu et al. (1972, 1973). A spiral potential is chosen of the form of Equation 4.7, and the gas is assumed to be isothermal (Roberts, 1969) or a 2 phase medium (Shu et al., 1972). The solutions to the fluid equations are found in terms of a 2 dimensional coordinate system, parallel and perpendicular to equipotentials. These solutions provide the density and velocity of gas in the galactic disk. The gas is assumed to flow in closed streamlines, which repeat over a period of 2π. The streamlines depart from circular motion due to perturbations by the spiral potential. For a potential of sufficient strength, the velocity of the gas perpendicular to the spiral arms is reduced sufficiently to produce a shock. The location of the shock depends on the strength of the potential, pattern speed and sound speed of the gas (Slyz et al., 2003; Gittins & Clarke, 2004). The densities and location of the shock are described further in Section 4.6.

As discussed in Chapter 1, molecular clouds are largely confined to the spiral arms, particularly in the Outer Galaxy, and it has long been recognised that star formation occurs primarily in the spiral arms (Baade & Gaposchkin, 1963). This could be merely due to the increased density of gas in the spiral arms, showing a Schmidt law dependence (Kennicutt, 1989). Alternatively, the dynamics of the spiral shock may play a direct role in forming molecular clouds. This view was first put forward by Roberts (1969), who proposed that shocks produced by spiral density waves 'trigger' star formation in spiral

galaxies. It is this possibility that is investigated in the rest of this thesis, or rather whether spiral density waves can trigger molecular cloud formation.

Observationally, evidence for direct triggering of star formation is inconclusive. As mentioned in Section 4.1, observations of streaming velocities in external galaxies has established the presence of density waves, and imply that the gas shocks in the spiral arms. There is further evidence of spiral shocks in star forming regions in our own Galaxy (Zhang et al., 2001; Normandeau, 1999). Recent results from a sample of 20 spiral galaxies (Seigar & James, 2002) indicate a correlation between the strength of spiral arm shocks and the star formation rate. Observations of NGC 3992 and NGC 628 (Cepa & Beckman, 1990) also show a non-linear increase in star formation in the spiral arms indicative of triggering. On the other hand, a comparison of spiral arms in grand design and flocculent spiral galaxies (Elmegreen & Elmegreen, 1986; Stark et al., 1987) indicated no correlation of spiral arm class with star formation rate. This could suggest that spiral shock triggering is not widespread, but limited to galaxies with very strong density waves, since it may be expected that if spiral shocks directly trigger star formation, then grand design galaxies will show an increased star formation rate.

There may also be an observable difference between star formation in the spiral arms and the interarm regions. It is apparent that the largest molecular clouds tend to be located in spiral arms (Stark & Lee, 2006; Dame et al., 1986), and possibly that the spiral arms also contain a greater concentration of massive stars (Romanishin, 1985; Cedrés et al., 2005). Large molecular cloud complexes are observed in the interarm regions of M51, but do not appear to be gravitationally bound compared to their spiral arm counterparts (Rand & Kulkarni, 1990).

4.5 Initial conditions and details of simulations

The simulations in the following chapters consider a region of the galactic disk between a radius of 5 and 10 kpc. For the galactic potential described, the orbits of the SPH particles all lie within co-rotation (at approximately 11 kpc). A limited section of the galactic disk is chosen to maximise the resolution of the simulations. At smaller disk radii, the effects of a galactic bulge or bar are more likely to effect the gas dynamics, which are not included in these models. The disk scale height is $z \approx 100$ pc, which is similar to the scale height expected for 100 K gas (Dickey 2005).

The initial positions and velocities of the particles are determined from a 2D test particle run and are shown in Figure 4.2. The particles in the test particle run are initially distributed uniformly with circular velocities, according to the potential of the disk (Equation 4.10). They evolve for a couple of orbits subject to the galactic potential, to give a spiral density pattern with particles settled into their perturbed orbits. For the SPH runs, the velocities in the z direction are allocated from a random Gaussian distribution of 2.5% of the orbital speed. The same magnitude velocity dispersion is applied in the plane of the disk. Overall, gas in the plane of the disk is in equilibrium, as the rotational velocities of the gas in the disk balance the centrifugal force from the potential. Approximate equilibrium is maintained in the vertical direction from the velocity dispersion of the gas. There is little difference as to whether the particles are initially distributed randomly, or

from a test particle run, but a steady state evolves more quickly in the latter.

The number of particles used in simulations is either 10^6 or 4×10^6. The simulations are run for between 200 and 300 Myr, where the orbital periods at 5 and 10 kpc are 150 Myr and 300 Myr respectively. The gas passes through multiple spiral shocks in this time and reaches a steady state. No boundary conditions are applied to the calculations, although this introduces a slight distortion at the inner and outer edges of the disk, where the gas pressure is underestimated. With 4×10^6 particles, the disk is fairly well resolved in the spiral arms, where the ratio of the smoothing length (h) to the disk scale height (H) is approximately 0.4 (the disk scale height calculated as the height of the disk which contains 2/3 of the local disk mass). However the ratio h/H increases up to ≈ 1 in the interarm regions.

The total mass of the disk is nominally 5×10^8 $M_\odot$, but as self-gravity is not included, the total gas mass can be scaled to higher or lower masses. The gas is distributed uniformly on large scales with an average surface density of $\Sigma \approx 2$ $M_\odot$ pc^{-2} and average density of 10^{-2} $M_\odot$ pc^{-3}. For the highest resolution run, most gas in the interarm regions has densities ranging from 10^{-3} $M_\odot$ pc^{-3} to 10^{-2} $M_\odot$ pc^{-3} whilst the initial peak density in a spiral arm is ≈ 0.5 $M_\odot$ pc^{-3} (Figure 4.3). The nominal surface density (≈ 2 $M_\odot$ pc^{-2}) is lower than the gas surface density of 5 $M_\odot$ pc^{-2} suggested by (Wolfire et al., 2003) for a radius of 8.5 kpc, although the simulations mainly focus on modelling just the cold phase of the atomic gas. The distribution of mass is also plotted at later times in Figure 4.3, and does not change significantly after ~ 100 Myr. For a steady state to occur, the simulation should be run for a time $\frac{2\pi}{\Omega-\Omega_p}$ but this is impractical near co-rotation where $\Omega \sim \Omega_p$.

As described in Chapter 1, the thermal composition of the ISM is complex and the proportion of the different thermal phases is not accurately known. Most of the calculations in this thesis use a single phase medium. Although this does not represent the various phases of the ISM, this treatment allows the overall structure of the disk and spiral shock to be compared for the different temperatures of gas which will occur in the ISM. The single phase calculations presented here use gas temperatures of 10, 50, 10^2, 10^3, or 10^4 K. For GMCs to form, gas entering the spiral arms must be cold atomic clouds (Elmegreen, 2002) or pre-existing molecular gas (Pringle et al., 2001). Since the overall aim of this work is to investigate molecular cloud formation, the lower ISM temperature calculations are more relevant to this problem. The gas is assumed to be isothermal, neglecting the processes of heating and cooling which are required to model the ISM consistently. The omission of heating and cooling with respect to the estimates of molecular gas densities is described further in Chapter 5. Chapter 6 looks at molecular cloud formation in a 2 phase medium.

4.6 Overall view of simulations

Before describing the results of these simulations in detail, an overview is provided of the main features for different temperatures, and the evolution of the structure of the disk with time.

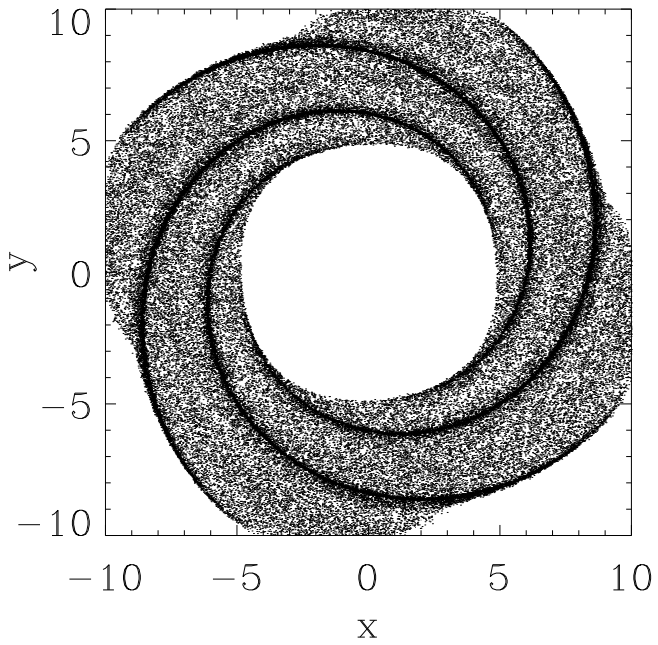

Figure 4.2: The initial positions of particles obtained from the test particle simulation are plotted. 100,000 particles are shown here, although a million particles were used to provide the SPH initial conditions.

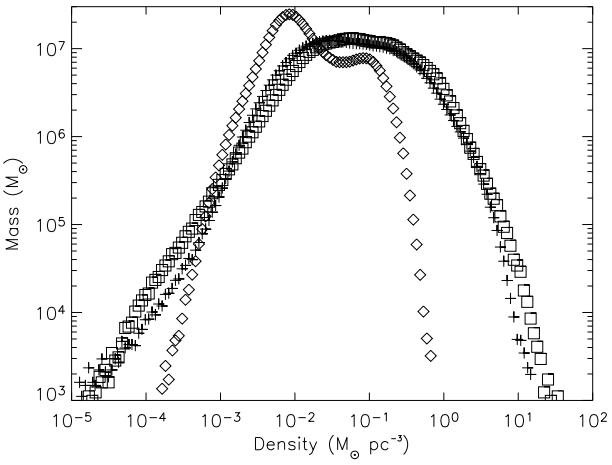

Figure 4.3: The distribution of mass as a function of gas density at the beginning (diamonds), after 100 Myr (crosses) and at the end (280 Myr) (squares) of the 50 K simulation. The nominal density for molecular clouds is 2.5 $M_\odot$ pc^{-3}.

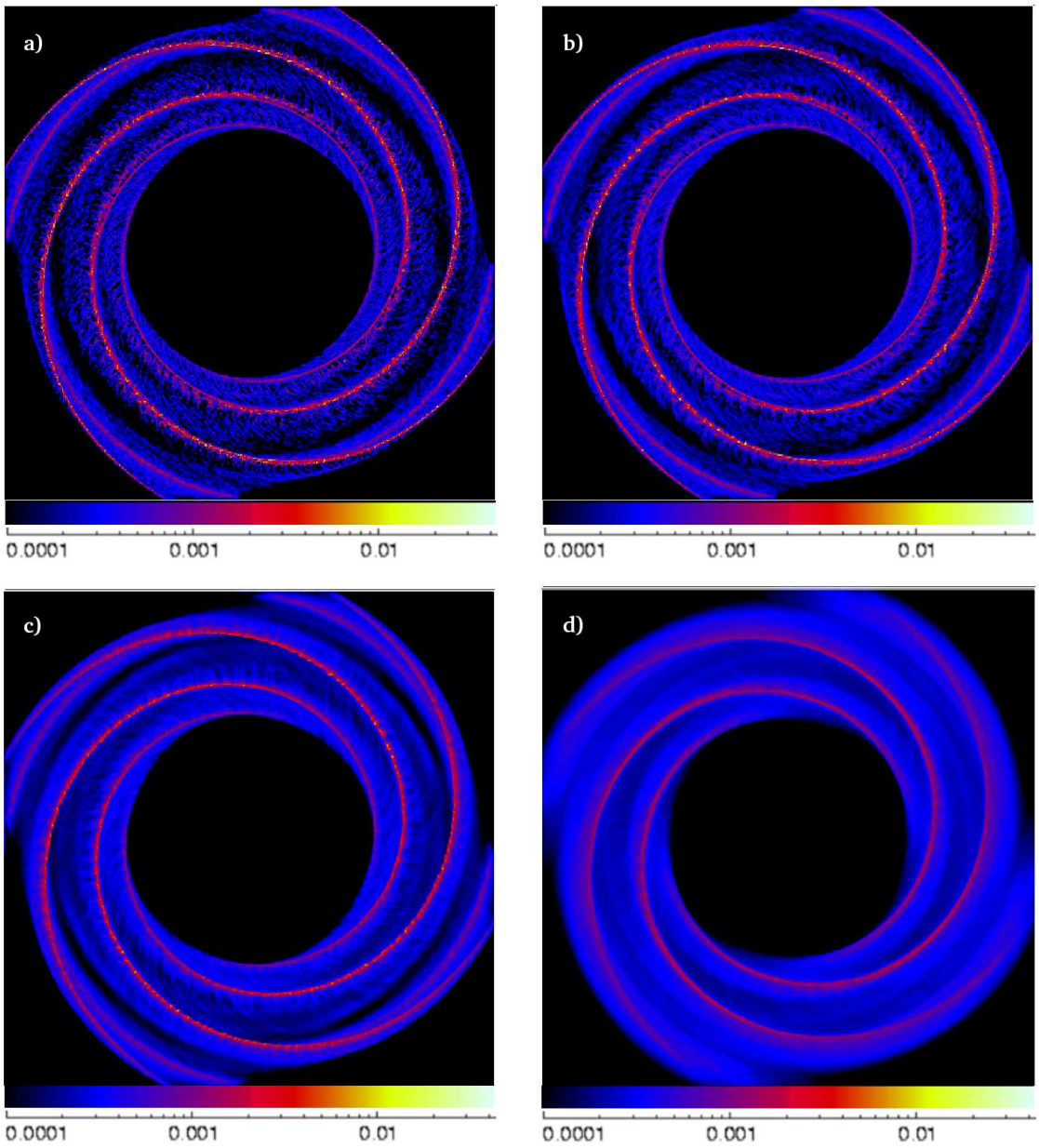

Figure 4.4: These figures show the column density after 100 Myr for simulations at different temperatures (in all cases 1 million particles are used). Each plot is 20 kpc by 20 kpc and the temperature is a) 10 K, b) 100 K, c) 1000 K and d) 10^4 K. All plots are shown in the rotating frame of the potential.

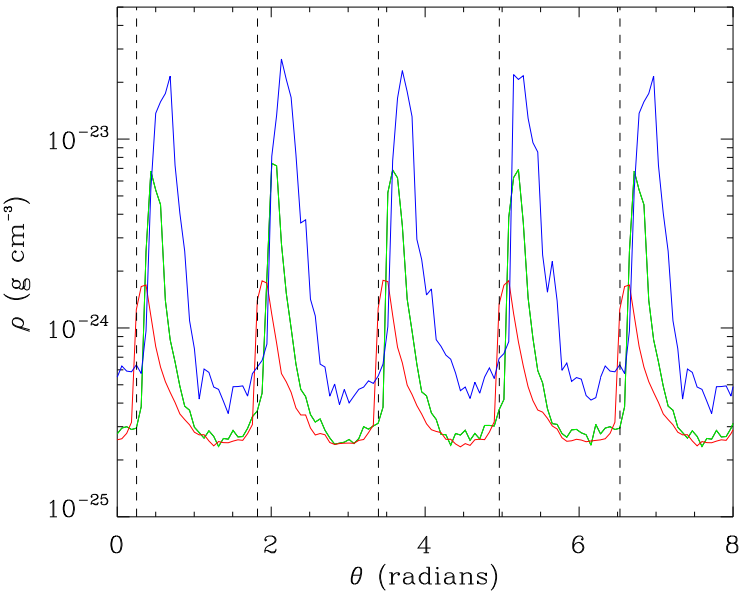

Figure 4.5: The density is plotted versus azimuth for the 50 K (blue), 1000 K (green) and 10^4 K (red) simulations after 100 Myr. The average density is calculated from 500 by 200 pc areas at 7.5 kpc. The gas is flowing in the direction of positive θ. Also indicated are the minima of the potential (dashed lines).

4.6.1 Density and structure of disk

Figure 4.2 shows the initial conditions used for all the simulations, from the evolution of particles subject to the spiral potential without gas pressure. As expected, the gas is initially evenly distributed with smooth spiral arms. The widths of the spiral arms are even along the length of each arm, and the densities across the arms are fairly uniform. Figure 4.4 show images of the whole galactic disk for gas temperatures of 10, 100, 1000 and 10^4 K, after the SPH simulations have run for 100 Myr. The structure of the disk is very different for the different temperatures. For the 10 and 100 K gas, there is a strong spiral shock producing dense spiral arms. The effective Mach number of the shock decreases with increasing sound speed, so the shock is much weaker for the 10^4 K gas. The density dependence on azimuth is shown in Figure 4.5, for 50 K, 100 K and 10^4 K gas, again after 100 Myr. The density is determined from a ring of width 200 pc centred at 7.5 kpc. The ring is divided into 100 segments each of length $r\triangle\theta = 500$ pc and area 9×10^4 pc^2, with the average density calculated in each segment. The figure shows an approximately 40 fold increase in the average density in the spiral arms for the 50 K simulation compared to a 5 fold increase for the 10^4 K simulation.

The 100 K simulation also shows considerable secondary structure, both in the spiral arms, and where material is leaving the spiral arms. By contrast, the disk and spiral arms are completely smooth in the 10^4 K simulation. As mentioned in the introduction, most previous simulations have used temperatures of approximately 10^4 K and have a similar morphology to Figure 4.4 d.

4.6.2 Evolution of highest resolution run

The highest resolution run (4×10^6 particles) was performed at 50 K, chosen to investigate the interesting structure present in the colder gas, and since significant molecular gas formation is more likely at a relatively cold temperature (Chapter 5). Figure 4.6 focuses in on the evolution of a section of the gas disk with time for the 50 K simulation (the whole disk is shown in Section 4.8.1). After 50 Myr, the distribution of gas is still relatively uniform across the interarm regions. The density in the spiral arms has increased though as the spiral shock develops. Some structure is beginning to evolve in the spiral arms, as apparent in the inner regions of the disk where structures are shearing away from the arms. After 100 Myr, the structure in the spiral arms is much more evident with the gas in the arms becoming clumpy. As shown in Figure 4.3, the density of gas in the simulations extends to over 10 $M_\odot$ pc^{-3}, above the nominal density for molecular clouds. As will be discussed in Chapter 5, the density of these clumps is high enough for molecular hydrogen formation. The spiral arms also become more ragged and their width increases, whilst the interarm regions are no longer uniform. By 150 Myr, structure perpendicular to the spiral arms has evolved into prominent spurs. The details and formation of these spurs are described in Section 4.8.1.

4.6.3 Location of the spiral shock

Figure 4.5 also shows the location of the spiral shock with respect to the minimum of the potential, at a radius of 7.5 kpc. For all temperatures, the gas shocks after the potential minimum, but the shock is much closer to the minimum for the hotter gas. Intuitively, the shock may be expected to lie after the potential minimum. As the gas moves down the potential, it gains energy and therefore velocity. The velocity then decreases as the gas climbs back up the potential, and for a strong enough potential, the velocity decrease is sufficient to cause a shock (Figure 4.7). However, this is in contrast to Roberts (1969), who instead finds that the gas shocks before the minimum inside corotation. The theoretical results provide steady state solutions, assuming the orbits have settled into the potential. This allows the situation where the orbits become aligned to produce a shock before the minimum, although this scenario is less obvious than shown in Figure 4.7. The location of the shock was compared at later times during the simulations, and although the location of the shock moves slightly closer to the potential minimum, the shock still lies after the minimum for the 3 temperatures.

The difference between these results and Roberts (1969) is in fact due to the nature of the potential and the location relative to corotation. These simulations in particular use a 4 armed spiral potential, whilst Roberts (1969) uses a 2 armed potential. The location of the shock from previous numerical simulations is found to agree reasonably with corresponding values determined by theoretical analysis (Gittins & Clarke, 2004). Oddly, for a 4 armed spiral potential, the shock lies after the minimum for most radii inside corotation, whereas for a 2 armed potential, the shock lies before the minimum. Further results to illustrate this are included using the potential of Equation (4.12), but with $N = 2$ (Figure 4.8). At a radius of 7.5 kpc, the hot (10^4 K) gas (assumed for Roberts (1969) and Gittins & Clarke (2004)) shocks before the potential minimum, although the shock is still after the minimum for the cold gas. Further inside the disk, at 6.5 kpc, both

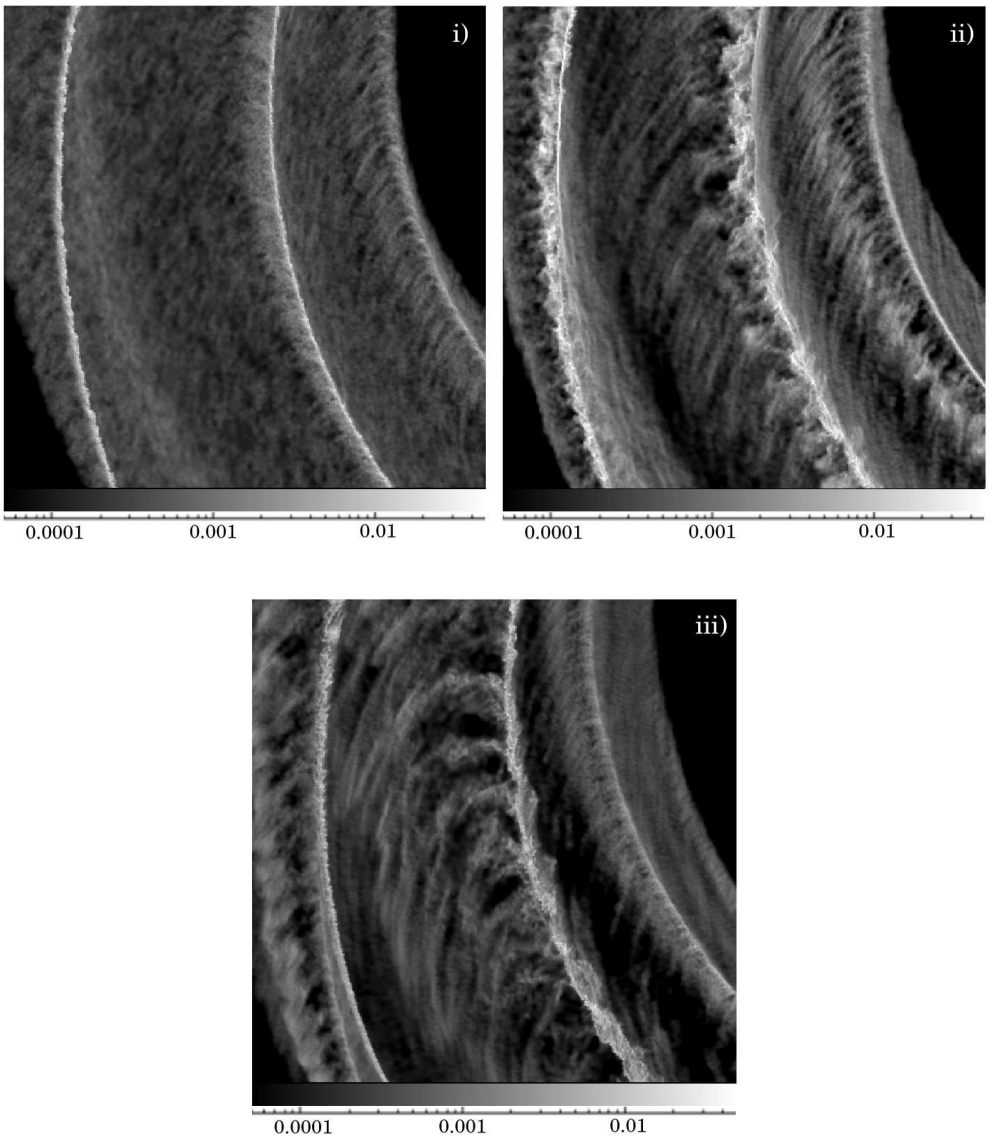

Figure 4.6: Column density plots (g cm^{-2}) showing a 5 kpc by 5 kpc section of the disk (with Cartesian coordinates -9 kpc $< x <$ -4 kpc and -5 kpc $< y <$ 0 kpc. The xy-coordinate grid is centred on the midpoint of the disk and remains fixed with time. Gas is flowing clockwise across the disk, i.e. from bottom to top. The time corresponding to each plot is i) 50 Myr, ii) 100 Myr and iii) 150 Myr. This simulation used 4 million particles with a temperature of 50 K.

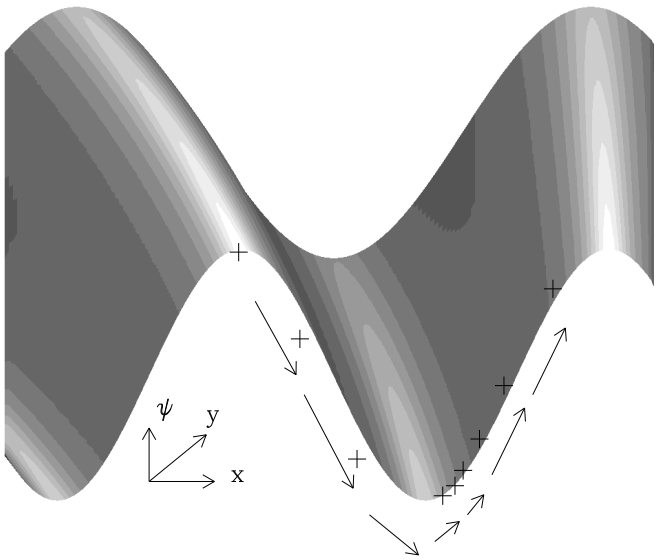

Figure 4.7: Diagram showing the cross section of a spiral potential through a galactic disk. Crosses indicate the possible positions of particles as they travel over the potential, with the build up of material which is climbing up from the minimum of the potential. To simplify, the crosses are shown in a 2D representation - in reality flows across the potential converge in a direction parallel as well as perpendicular to the shock (Figure 4.22).

hot and cold gas shock after the minimum whereas at 8.5 kpc, both hot and cold gas shock before the minimum (with corotation at 11 kpc). The dependence of the location of the shock is further discussed for different shock strengths, pitch angles and pattern speeds in Gittins & Clarke (2004) and Slyz et al. (2003).

Recent observations of young star forming regions in NGC2997 (Grosbøl et al., 2006) indicate that the spiral shock occurs before the potential minimum. CO measurements tend to either show CO intensity peaks before the maximum stellar density, e.g. M51 (Aalto et al., 1999) or is roughly coincident with the maximum stellar density e.g. M83 (Lundgren et al., 2004).

4.7 The dynamics of spiral shocks

The main structures noted in the cold gas simulations are the clumps, which evolve in the spiral arms, and the interarm spurs. This section provides an explanation for the clumpiness in the arms, which is most noticeable in Figure 4.6 ii). The following section (Section 4.8) goes on to describe the formation of spurs.

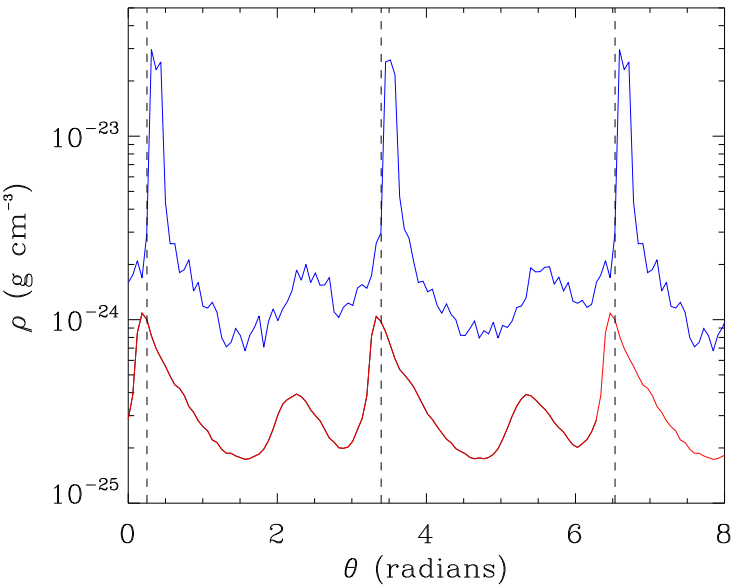

Figure 4.8: The density is plotted versus azimuth for 100 K (blue) and 10^4 K (red) gas for a 2 arm potential. The gas is flowing in the direction of positive θ and the average density is determined at a radius of 7.5 kpc. The minima of the potential (dashed lines) lie between the shocks at the different temperatures.

4.7.1 Structure formation in the spiral arms

For the simulations of cold gas, distribution of gas in the spiral arms changes from a smooth thin shock to clumpy structures distributed along the spiral arm, as highlighted by Figures 4.4 and 4.6. The highest density gas, present in these clumps, is comparable with the density of molecular clouds e.g. a density of 100 cm^{-3} corresponds to just less than 5 M$_\odot$ pc^{-3}, which is within the range of densities attained in Figure 4.3. As described in Chapter 1, molecular cloud formation is commonly attributed to gravitational and magnetic instabilities. However these simulations include neither self gravity or magnetic fields, so another process must be involved. The formation of these dense molecular cloud structures can be understood as being caused by the dynamics as interstellar gas passes through a spiral shock. The effect of the spiral shock on the dynamics of the particles can be seen by examining the change in angular momentum of particles as they travel through a spiral shock. Initially, the pre-shock gas contains small-scale structure due to the particle nature of SPH. The spiral shocks amplify any pre-existing structures such that the clumpiness of the gas increases with each passage through a spiral arm. This amplification of clumpiness corresponds to changes in the angular momentum phase space density of the gas. This can be seen at first glance in Figure 4.9, which shows the angular momentum phase space near the beginning of the 50 K simulation, and at a later time when the gas is in the spiral shock. The phase space is fairly smooth initially, but becomes a lot more clumpy as the gas passes through the spiral shock.

The dynamics of the shock are described in detail for the high resolution 50 K simulation in this section. At the beginning of the simulation, the distribution of the

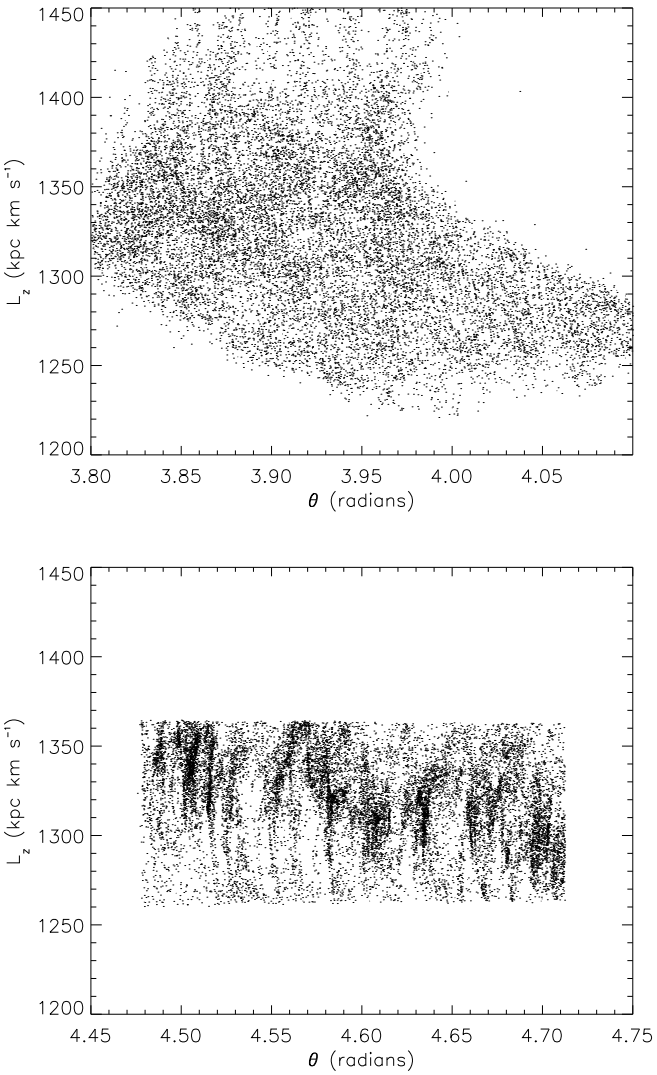

Figure 4.9: These figures show the angular momentum for the particles in a section of the disk, where θ is the azimuthal angle measured clockwise round the disk. The top plot shows the angular momentum phase space for the particles after 10 Myr. The bottom plot shows the same particles after 50 Myr, as the particles are going through a spiral arm. The particles were selected from a region of the spiral arm after 50 Myr, and their angular momenta determined after 50 and 10 Myr.

particles' angular momentum is smooth. In a strong spiral shock, the orbits of the particles become crowded together in the proximity of the spiral arm. At any point along the spiral arm, particles from a range of radii interact with each other and shock. These interactions cause the particles to gain or lose angular momentum. Thus the shocks disturb the smooth phase-space density of the gas particles by modifying the particles' angular momenta. With no such interactions between the particles, there is only a small change in angular momentum due to the non-axisymmetric potential (Figure 4.10).

This change in angular momentum is illustrated in Figure 4.11, which plots the evolution of L_z, the z-component of the angular momentum, for a select number of particles as a function of time. Initially the particles are at the same azimuth, but occupy a range of radii, with the larger radii corresponding to larger L_z. A similar plot (Figure 4.22) is shown in Section 4.8.1, accompanied by a plot of the particles' orbits, which more clearly shows how the orbits converge in the spiral shock. Particles with higher initial values of L_z, and therefore at larger radii, enter the shock earlier. This is because the spiral arms are trailing and the particles are inside the co-rotation radius (see Figure 4.12). As a particle enters such a shock it is typically at the outer radial range of its epicyclic motion within the spiral potential (see, for example, Figures 3 and 9 in Roberts (1969)), and so has lower angular momentum than the average for that radius. Thus when it enters the shock, it mixes immediately with material which has higher angular momentum. In Figure 4.11, the particles entry into the shock is marked by a sudden jump in the value of L_z. Figure 4.13 shows that the magnitude of the jump is correlated with the post-shock density the particle encounters. Thus the stronger the mixing, the bigger the jump. Each particle then travels along nearly parallel to the shock for some distance, before it leaves the shock (Roberts, 1969).

As it moves along the shock, the particle stays roughly in phase with the rotating spiral potential, and is subject to a torque from the potential. The particle in the shock experiences a retarding torque from the potential and loses angular momentum (Figure 4.12). As the particle loses L_z, it travels radially inwards along the spiral arm. Eventually L_z is too high for the particle to travel further radially inwards and the particle leaves the spiral arm. Once the particle leaves one spiral arm it then proceeds at more or less constant L_z until it meets the next one. From Figure 4.10 it can be seen that the decrease in L_z, which occurs as the particle slowly leaves the spiral arm, exceeds the increase it acquires on entry to the arm. Thus the net effect of the spiral potential, coupled with dissipation in the arms, is to produce a steady transfer of angular momentum from the particles to the potential. Figure 4.14 shows the change in distribution of the particles and the increase in the non-uniformity of the distribution with time and indicates a slight reduction in the angular momentum of the particles.

For the simulations with higher values for the temperature of the ISM, the shocks are weaker, and the distribution in L_z stays much more uniform. This is because the particles are subject to smaller changes in L_z as they pass through the shock. As the density of the shock is less, particles entering the shock are less likely to interact with other particles. The typical increase of L_z is lower than that shown for the particles in Figure 4.11. Hence the particle is also subject to a retarding torque for a shorter amount of time and can more readily leave the spiral arm before interactions occur with other particles.

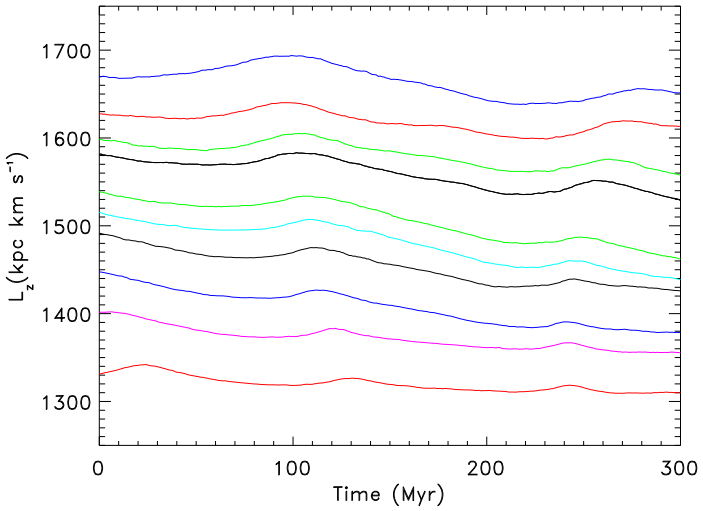

Figure 4.10: The angular momentum (z-component) with time of 10 selected particles from the test calculation (without hydrodynamics) The particles are initially all at the same azimuth, but at different radii.

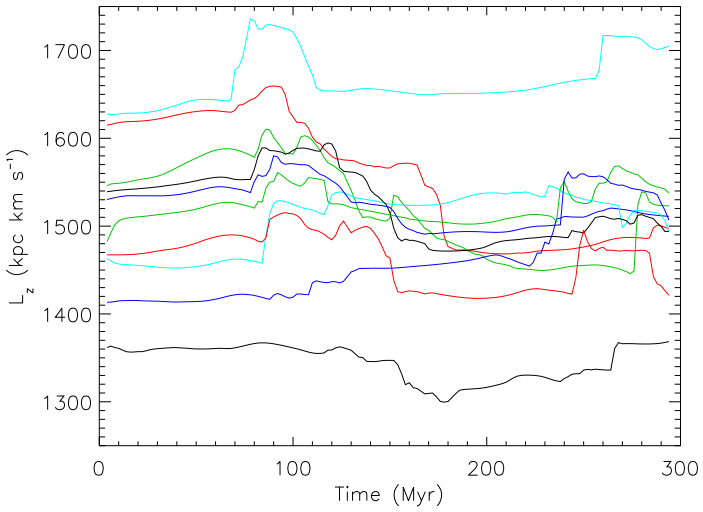

Figure 4.11: The angular momentum (z-component) with time of 10 selected particles with 6.8 kpc $< r <$ 7.8 kpc. The particles are initially all at the same azimuth, but at different radii.

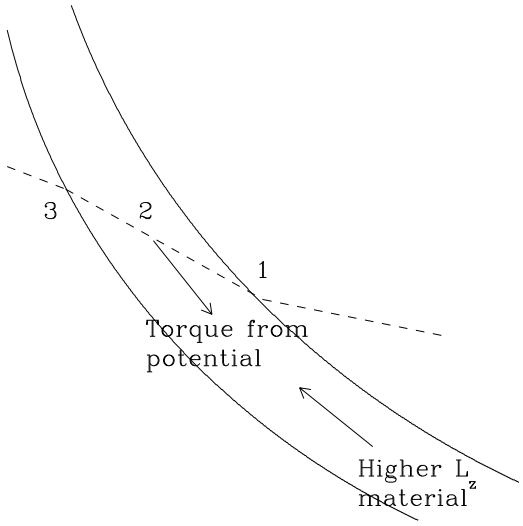

Figure 4.12: Typical passage of particle through spiral arm, in the rest frame of the spiral potential. The particle is assumed to lie within co-rotation. As the particle enters the spiral arm (1), it encounters higher angular momentum material. The particle experiences a shock perpendicular to the spiral arm, but its velocity parallel to the spiral arm initially increases. The particle travels along the spiral arm (2), more or less in phase with the spiral potential. The particle is then subject to a decelerating torque from the potential. Eventually the angular momentum is too high for the particle to remain in phase with the spiral potential, and the particle leaves the spiral arm (3).

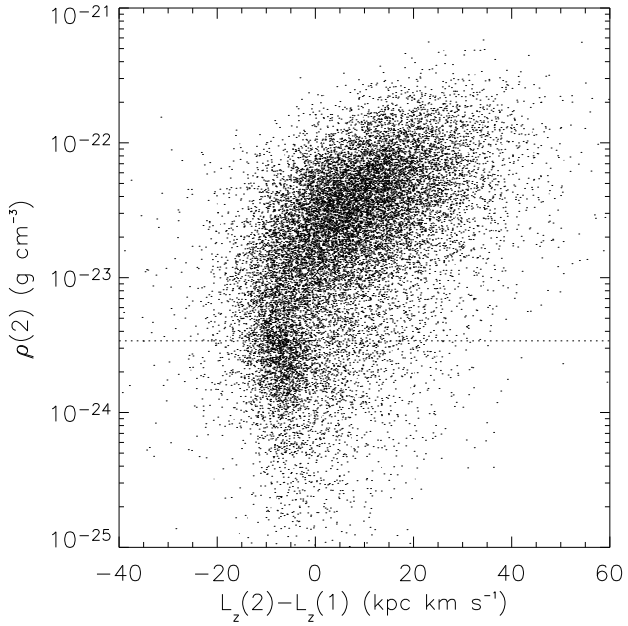

Figure 4.13: The jump in the z-component of angular momentum ($L_z(2)-L_z(1)$) is plotted as a function of post-shock density ($\rho(2)$) for a number of particles. The pre-shock densities of the particles (not shown) all fall below the dotted line. There is a strong correlation between density enhancement in the shock and the magnitude of the jump in L_z.

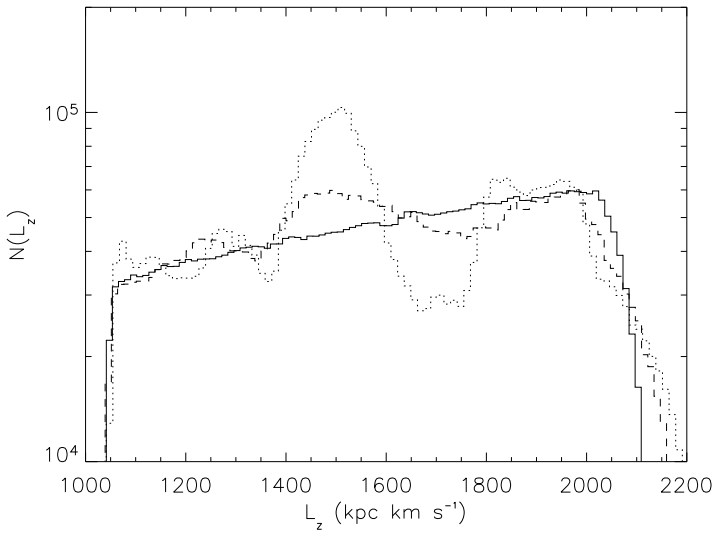

Figure 4.14: The number of particles (N(L_z)) which have the value of the z component of the angular momentum L_z. The total number of particles for the whole disk is included at the beginning of the simulation (solid line), after 140 Myr (dashed line) and after 280 Myr (dotted line).

The pre-shock ISM, as shown in the initial conditions in Section 4.5, is inhomogeneous, with particles randomly distributed. This inhomogeneity is amplified within the spiral arms, where the gas assembles into more recognisable small scale clumps. It is this amplification which gives rise to the structures within the arm, particularly in the more dense molecular gas, as will be shown in Chapter 5. Figure 4.15 (upper) shows the density in a small sector of the simulation. Since θ is measured clockwise round the disk, particles are located in the top part of the disk, and are selected to cover a spiral arm. The gas is travelling approximately from left to right across the spiral arm. Approaching the spiral arm from below can be seen apparent waves of material. These are in fact the remnants of clumps formed in the previous arm, which have become elongated by the differential shear in the inter-arm region. These inhomogeneities, which are transmitted from the previous arm, provide input for new inhomogeneities in the next arm. In Figure 4.15 (lower) the value of L_z for each of the particles in Figure 4.15 (upper) is plotted as a function of the θ-coordinate. The region below the arm (Figure 15 (lower)) spans a relatively small range in L_z, and the phase-space density here is relatively smooth. Just above this is a region where the phase-space density drops. This corresponds to the rapid jump in L_z, discussed above, which occurs as particles enter the spiral shock. Above this there is a patchy structure of phase-space density enhancements. It is clear that the inhomogeneity which occurs here, within the arm, is much greater than that seen in the pre-shock gas.

A simple analogy to the behaviour of the gas passing through the spiral shock is the flow of a single lane of traffic along a highway. If the flow is uniform, the cars will be travelling at equal velocities and with equal spacing. Similarly if the cars enter the highway at regular intervals, as they leave, the flow will remain uniform. However if the cars instead enter the highway at different points and with different velocities, queues will form within the flow. As the traffic leaves the highway the cars are situated in groups

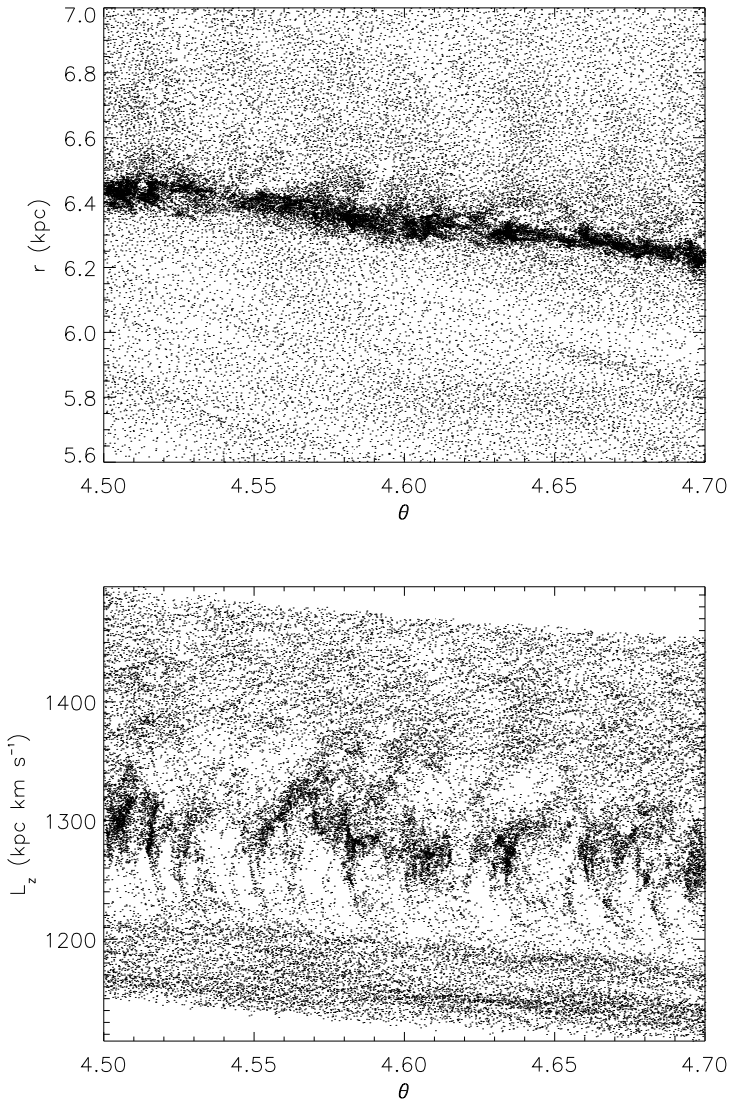

Figure 4.15: The top figure shows particles in a section of the disk in coordinates (r, θ). θ is measured clockwise round the disk, and thus the section is taken from the top of the disk. Gas is moving from left to right. The bottom figure shows the corresponding z component of the angular momentum plotted against θ. The simulation has evolved for 50 Myr and shows the converging of orbits in the shock.

instead of regularly spaced intervals. For the passage of gas through the spiral arm, the particles enter the arm with different velocities (depending on radius), bunch together and form clumps (Figure 4.15). The clumps then leave the arm at some point corresponding to their velocity, when the angular momentum of the clump becomes too high to permit further travel inwards along the spiral arms.

4.7.2 Spacing of clumps

A rough estimate can be made of the linear scale of the inhomogeneities found in the spiral arms. The typical time a particle spends within a spiral arm can be estimated from Figure 4.11 as being approximately $t_{arm} \sim 6 \times 10^7$ years. The typical velocity spread of particles within a spiral arm can be seen from Figure 4.16 to be approximately $v_\perp \sim 10$ km s^{-1}. Then the average scale-length of density structure generated by the piling up process would be $L \sim t_{\rm arm} v_\perp \sim 600$ pc. This agrees roughly with the mean distance between the highest density peaks along the arm, corresponding to the most dense molecular gas (yellow in Figure 5.6 (iv)).

4.7.3 The velocity dispersion in the spiral arms

Chapter 3, showed that a supersonic velocity dispersion is induced in gas which shocks when passing through a 1D sinusoidal potential. Furthermore, the velocity dispersion shows a velocity size scale relation similar to observations. To investigate this for the galactic disk, the 2D velocity dispersion is determined in the plane of the disk as a function of azimuthal angle. This is calculated by taking a 200 pc width ring centred at $r = 7.5$ kpc. The ring is divided into 100 segments, each of length $r\triangle\theta = 500$ pc and area 9×10^4 pc^2, and the velocity dispersion of the gas calculated in each segment.

Figure 4.16 shows the variation of the velocity dispersion, calculated after 100 Myr for the 50 K simulation. The velocity dispersion is shown for the velocity component in the plane of the galaxy, $v_\perp = \sqrt{(v_x^2 + v_y^2)}$, and the z component of the velocity. There is a sudden jump in the velocity dispersion as gas enters the spiral arms. The dispersion of $v_\perp$ increases to 10 km s^{-1} where the spiral arms occur. In comparison a velocity dispersion of 7-10 km s^{-1} is observed for molecular clouds of sizes 20-50 pc (Solomon et al., 1987; Heyer & Brunt, 2004). Bonnell et al. (2006) find a velocity dispersion up to 10 km s^{-1} in simulations of gas passing through a spiral shock. This velocity dispersion is due to random chaotic internal motions induced in clumpy gas subject to a shock.

The velocity dispersion quickly decreases upon leaving the arms. A further decrease in the velocity dispersion occurs in the interarm regions. The ratio in the smoothing length compared to the disk scale height (h/H) approaches 1 in the interarm regions. This potentially leads to damping of velocities due to insufficient resolution, particularly in the v_z velocity component.

The velocity dispersion here is not calculated specifically for the molecular clouds, instead a large increase in dispersion corresponds with the spiral arms where the molecular clouds are located (Chapter 5). Bonnell et al. (2006) show that a $\sigma \propto r^{0.5}$ law comparable

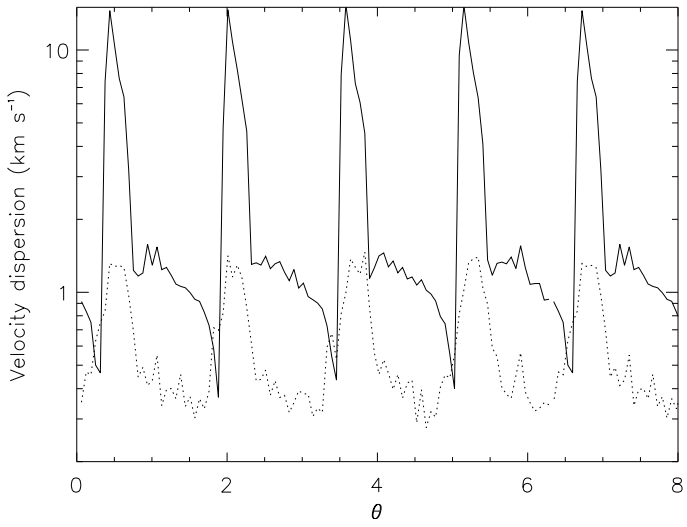

Figure 4.16: The velocity dispersion plotted against azimuth (θ) for a ring whereby r=7.5 kpc and $\triangle$r=200 pc. The figure shows the dispersion of the $v_\perp = \sqrt{(v_x^2 + v_y^2)}$ (solid) and the dispersion of v_z (dotted). (θ is measured clockwise round the disk, i.e. in the direction of gas flow.) The figure corresponds to a time of 100 Myr in the simulation.

to those observed occurs in smaller scale simulations of the passage of GMCs through spiral shocks. However the resolution of these simulations is too low to accurately determine the velocity dispersion of all but the largest molecular clouds.

4.8 Spurs and feathering

It is also evident from Figures 4.4 and 4.6 that the structure in the spiral arms leads to significant observable structure in the inter arm regions. This section starts by describing in more detail these features apparent from the simulations. Their formation is discussed following the explanation of the clumpy structure in the previous section. The presence of interarm spurs are common in spiral galaxies. A description of observational results, as well as other recent numerical and theoretical work is included in Section 4.8.2.

4.8.1 The formation of spurs

As seen from Figure 4.6 iii), spurs are an obvious characteristic of the cold gas simulations. Density plots for the whole disk of the 50 K simulation are shown in Figure 4.17 at 4 different times. Initially there is a smooth spiral perturbation to an approximately uniform disk. The density of the spiral arms increases with time and non-uniform structure develops along each arm. As this arm substructure grows, dense clumps shearing away from the spiral arms lead to interarm features. These features occur on the leading edge of the spiral arm, leaving the trailing side smooth. Structure perpendicular to the spiral arms is noticeable first in the inner parts of the disk (Figure 4.17b), and then spreads to

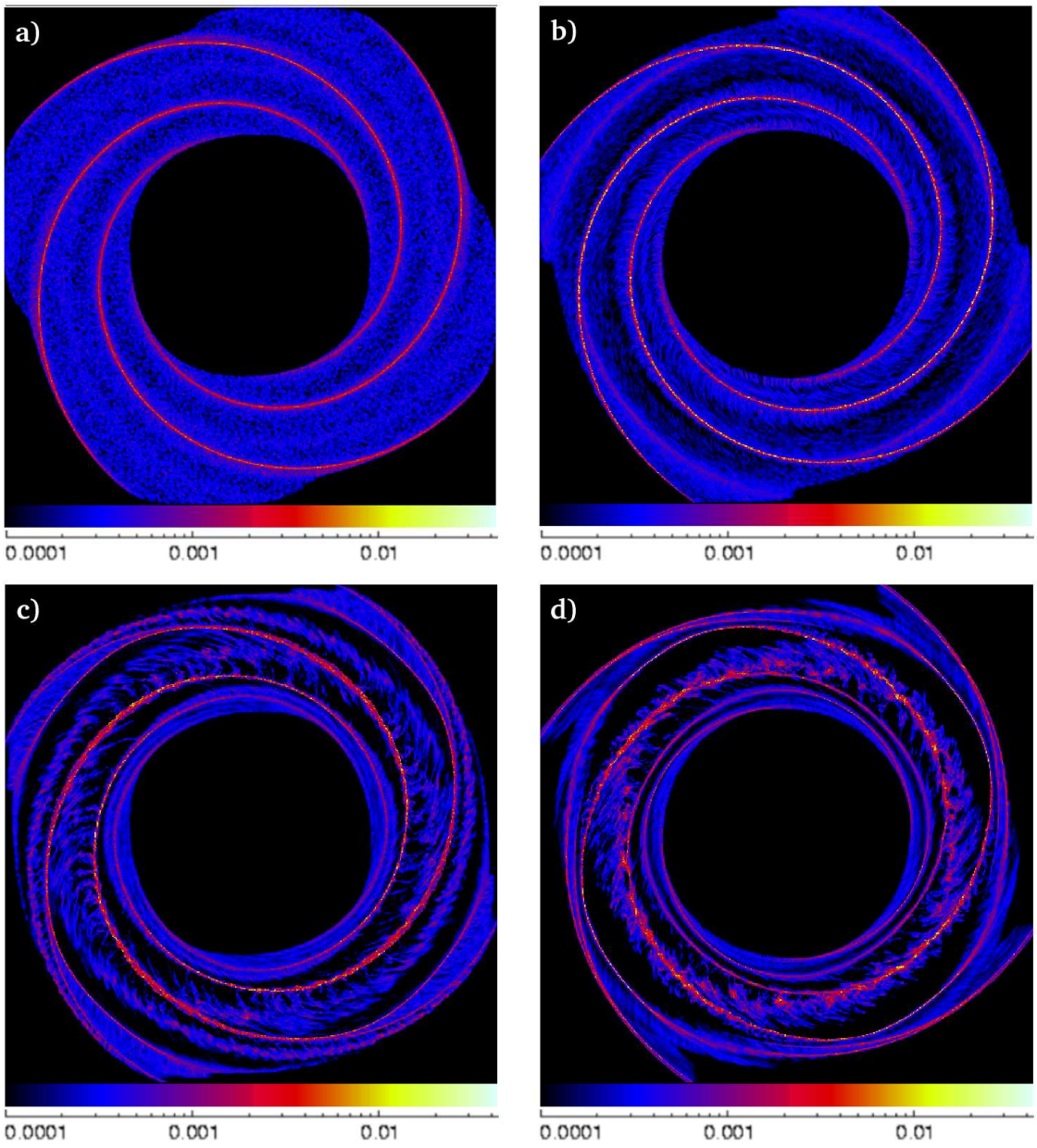

Figure 4.17: Column density plots (g cm^{-2}) when T=50 K after a) 0, b) 60, c) 160 and d) 260 Myr. The number of particles is 4 million and each plot is 20 kpc by 20 kpc. The same scaling is used on all subsequent column density plots in this chapter, and all column density plots are shown in the rotating frame of the potential.

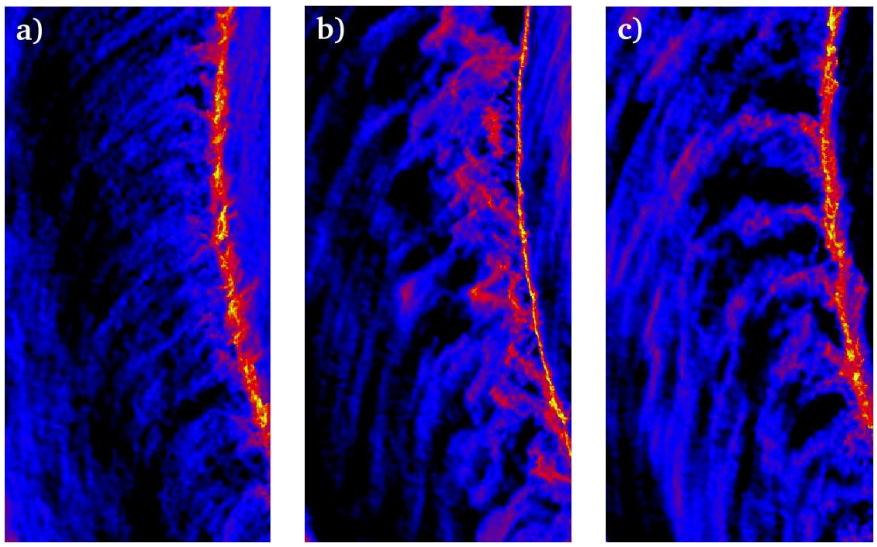

Figure 4.18: Time evolution of feathering and spurs. Column density plots for the 50 K run after a) 80 Myr, b) 120 Myr and c) 160 Myr. Each plot is 2 kpc by 4 kpc.

larger radii. This is not surprising since the orbital period is less at smaller radii, so the comparative evolution of that part of the disk is faster. Both the arm and interarm regions become more disordered with time, and consequently the spiral arms become wider.

The detailed structure of the spurs and feathering in the 50 K simulation is shown in Figure 4.18. The interarm structure increases with time from smaller scale structures to more pronounced larger scale spurs and feathering. The spurs (clearest in Figure 4.18 c) are perpendicular to the spiral arm. whilst the feathering refers to closely spaced parallel lanes of gas with a much smaller pitch angle than apparent for the spurs. Over time, spurs become more distinct with a regular spacing (≈ 0.7 kpc after 160 Myr in Figure 4.18 c). The feathering results from shearing of the spurs, so there is a direct correlation between the spurs that leave perpendicular to the spiral arm and the feathering that approaches the next spiral arm.

A larger section of the disk is shown for simulations at 100, 1000 and 10^4 K in Figure 4.19. As the temperature increases, the Mach number of the shock decreases and much weaker spiral arms are produced. The gas is largely smooth at 10^4 K due to the higher pressure, and the spiral arms exhibit no obvious substructure. The spiral shocks are much weaker for the higher temperature gas, since the change in velocity induced by the spiral potential is more comparable with the sound speed of the gas. For the 10^4 K case, the sound speed is ≈ 10 kms^{-1} whilst the change in velocity across the spiral potential is ≈ 20 kms^{-1}. The 1000 K simulation shows regular spaced more diffuse clumps along the spiral arms. The spurs, and to a lesser extent the feathering, are still evident but are less pronounced. On the other hand, the 10^4 K simulation does not display such interarm structure, but instead retains a smooth gas distribution (Figure 4.19 c).

In order to ascertain the origin of the interarm structure, the gas is traced backwards in time from the spur that leaves the spiral arm to when the gas was located in the spiral arm itself. Figures 4.20 and 4.21 show that there is a direct correlation between clumps in the spiral arms and the spurs that leave perpendicular to the arms. Thus the spurs

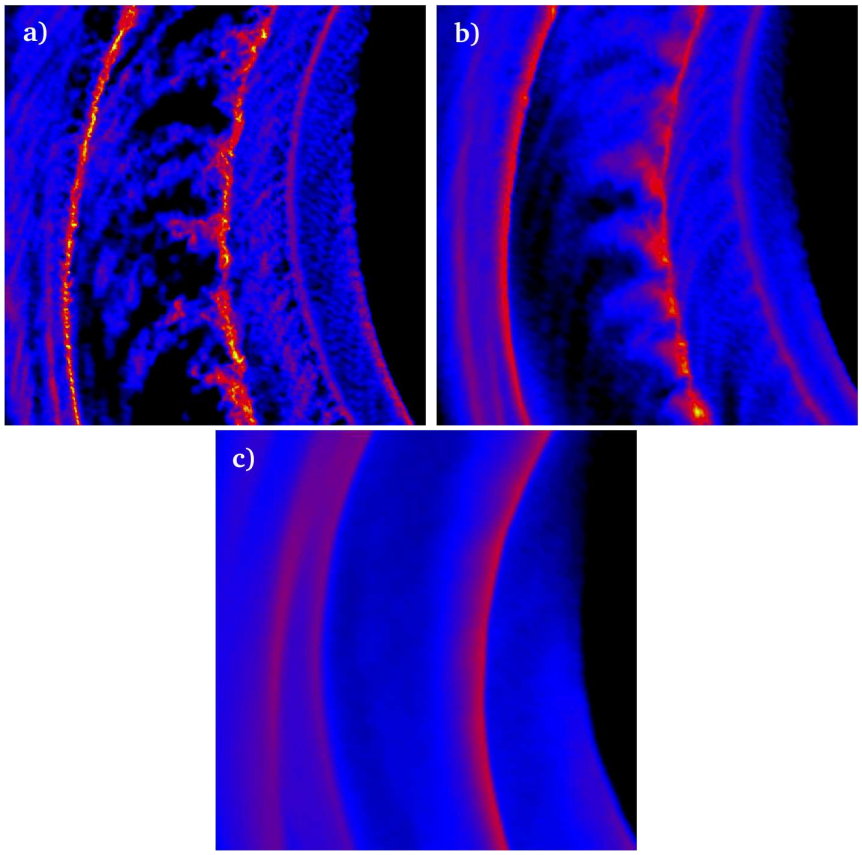

Figure 4.19: Column density plots (g cm^{-2}) when the temperature is a) 100, b) 10^3 and c) 10^4 K. The time corresponding for each figure is 220 Myr. Each plot shows a 5 kpc by 5 kpc section of the global simulation. The overall number of particles in these simulations is 1 million.

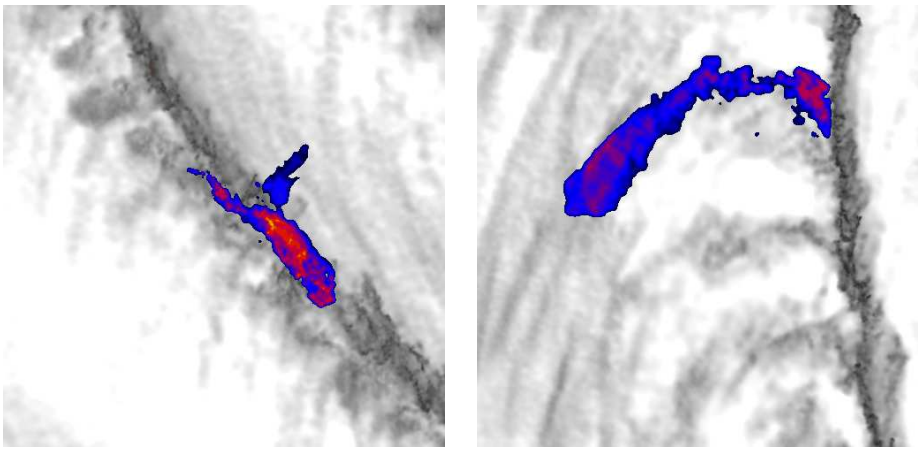

Figure 4.20: Formation of a spur (right hand plot, after 160 Myr) from a dense clump of gas in the spiral arm (left hand plot, after 100 Myr). The temperature is 50 K and both plots are 2 kpc by 2 kpc.

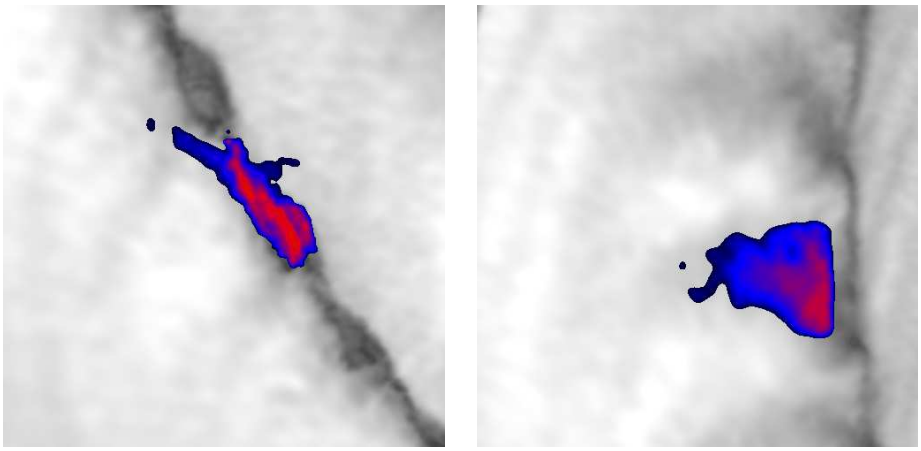

Figure 4.21: Formation of a spur (right hand plot, after 220 Myr) from a dense clump of gas in the spiral arm (left hand plot, after 180 Myr). The temperature is 1000 K and both plots are 2 kpc by 2 kpc.

simply result from the shearing of clumps in the spiral arms, due to the divergent orbits of material that leave the arm. Consequently the spacing of the spurs is similar to the spacing of the clumps, $\sim$ 600 pc estimated in Section 4.7.2. As structure (GMCs) is observed to exist in spiral arms, this provides a simple explanation for the presence of spurs, regardless of how the GMCs themselves are formed.

For an overall view of the process of clump and subsequent spur formation, the paths of the five particles and their corresponding angular momenta are plotted in Figure 4.22. The red line corresponds to a particle already in the shock, which therefore has higher angular momentum. Particles entering the shock typically show a jump in the angular momentum as they interact with the higher angular momentum material (e.g. yellow line, Figure 4.22). As particles travel along the spiral arm, they tend to lose angular momentum, since they are constrained by the spiral potential. It appears in Figure 4.22 that particles entering the shock later (e.g. green line) show less change in angular momentum, possibly because they interact with gas in the shock which has similar angular momentum. Hence the path represented by the green line is less affected by the shock, and this particle spends less time in phase with the potential compared to the others. Eventually the gas leaves the spiral arm when its angular momentum is too high to travel further radially inwards, and forms the spur shown in Figure 4.20.

The reduced degree of interarm structure apparent in the higher temperature simulations can again be interpreted as due to a weaker spiral shock. At higher ISM temperatures, the shocks are weaker and they have less effect on the particles' angular momentum. The particles spend a shorter time in phase with the potential, their orbits are less perturbed and the clumps which produce the spurs do not occur. Furthermore, the gas pressure can smooth out much of the structure during the crossing of the spiral arm. If the structure in the spiral arms is removed, then there is nothing to shear into the subsequent spurs and feathering in the interarm region. For example, the 10^4 K run has a sound speed of $\approx$ 10 km s^{-1} which is comparable to the velocity of the gas perpendicular to the spiral arm (in the rotating spiral potential). Thus, structures of size scales $\leq$ the width of the arm can be smoothed by the internal pressure before leaving the spiral arm.

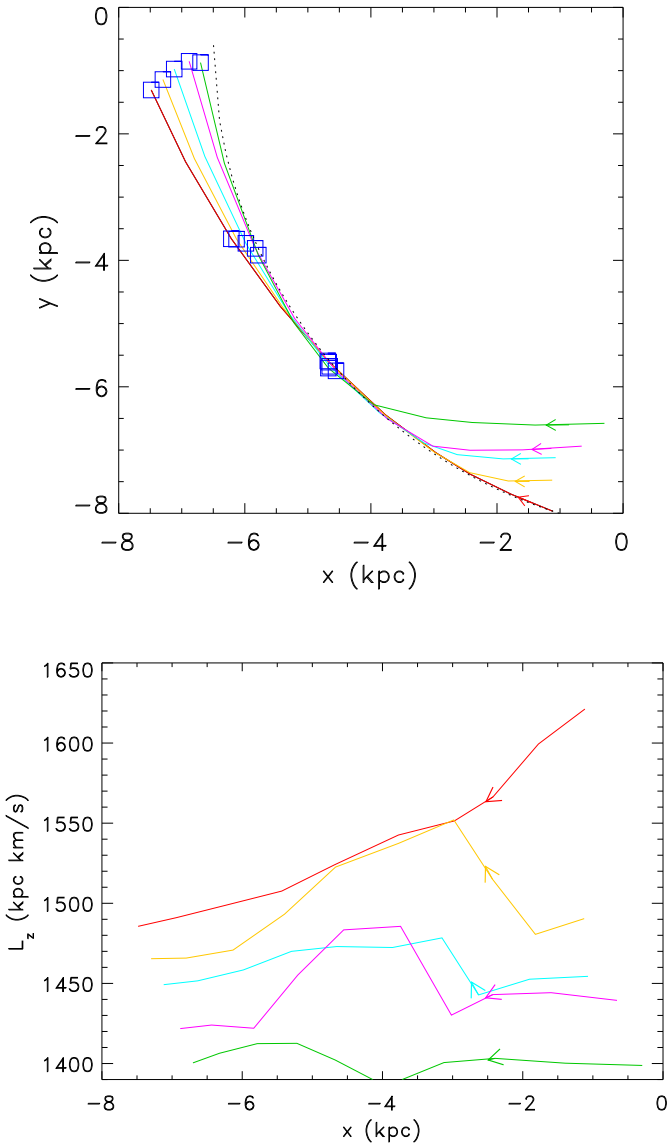

Figure 4.22: The orbits of 5 selected particles are displayed pre- and post-shock (top) where the xy-coordinates correspond to a fixed Cartesian grid centred at the midpoint of the disk. The dotted line indicates the position of the shock front, and the orbits are taken from the rest frame of the potential. Boxes indicate the location of the five particles at three corresponding times. The final position of the particles coincide with the spur shown in Figure 5.20 (right). The corresponding angular momenta of the particles are also plotted (bottom). Particles are travelling from right to left in both plots.

4.8.2 Interarm features in spiral galaxies

Interarm features similar to those described in these simulations are commonly observed in many spiral galaxies, including grand design galaxies such as M51 (Aalto et al. (1999)). These structures are secondary perturbations to the disk, unpredicted by density wave theory. Spurs (particularly in M51) often show a correlation with HII regions, suggesting a link between these structures and star forming giant molecular clouds. In fact the local star-forming region of Orion has been referred to as the Orion spur (Bok, 1959).

Spurs are seen as narrow dark lanes that extend perpendicular to the spiral arms (Lynds, 1970; Weaver, 1970). They are particularly striking in the HST images of M51 (Scoville et al., 2001), especially towards the centre of the galaxy. The spurs extend over half the distance between the arms, and are often dotted with HII regions. Surveys indicate that spurs have pitch angles of $30 - 50^o$ (Russell & Roberts, 1992) and widths comparable to those of spiral arms (Elmegreen, 1980). Further examples of spurs are also shown in Byrd (1983) (M31) and Kaufman et al. (1989) (M81). Feathering (Balbus, 1988; Kim et al., 2002) generally refers to parallel filamentary features shifted from the spiral arms. These are often observed on the outskirts of spiral galaxies (e.g. M74). Branches are more significant longer spurs often associated with resonances. Several simulations have previously shown the bifurcation of spiral arms primarily at the 4:1 resonance in their potential (Patsis et al., 1994, 1997; Chakrabarti et al., 2003).

Recent computational work has reestablished an interest in spiral arm substructure, and a new survey (La Vigne et al., 2006) has extended the observations given above. From a survey of 223 spiral galaxies, 20% contain feathers, which they define as extinction features branching off from the spiral arms, often associated with star formation. This fraction increases for galaxies with clearer spiral structure and well defined dust lanes.

4.8.3 Comparison with other numerical and theoretical work

Spurs have been suggested to form mainly through gravitational or magneto-Jeans instabilities. Balbus (1988) demonstrated that transient gravitational instabilities develop preferentially nearly parallel and nearly perpendicular to the spiral arm. This introduces the appealing scenario where spurs and density perturbations along the arms are generated by the same mechanism. Generally, dense regions along the course of the spiral arm will produce projections roughly perpendicular to the arm as a result of shear expansion. Simulations (Kim & Ostriker, 2002; Shetty & Ostriker, 2006) show the formation and fragmentation of spurs in 2D magneto-hydrodynamical calculations of a shearing box. Dense clumps are produced in the arms principally through the magneto-Jeans instability, leading to the formation of spurs. Previous numerical analysis by Dwarkadas & Balbus (1996) indicated that galactic flows through spiral arms are stable against purely hydrodynamic instabilities.

The simulations presented here show widespread spurs and feathering without self gravity or magnetic fields. The conditions necessary for their formation are instead that there is clumpy structure in the spiral arms, and the gas is sufficiently cold so this structure is not smoothed out. Although the clumps in the spiral arms could be formed through

magnetic or gravitational instabilities (Kim & Ostriker, 2006; Kim et al., 2002), the spiral shock alone may be sufficient. Previous 2D hydrodynamical simulations have also found small scale spurs forming along the spiral arms (Wada & Koda, 2004; Gittins, 2004). As mentioned previously though, the simulations in this thesis use temperatures lower than most previous numerical analysis. These results reveal that the temperature of the disk has a crucial effect on the disk structure and the formation of spurs. Consequently, interarm substructure is much more evident in these results than previous purely hydrodynamical simulations.

The analysis of Wada & Koda (2004) suggests an alternative explanation of spurs in terms of Kelvin Helmholtz instabilities. They observe a rippling distortion of the shock front which induces structure along the spiral arms, and the shearing of this structure to form spurs. Their analysis uses larger pitch angles than those of Dwarkadas & Balbus (1996). Kelvin Helmholtz instabilities require a high Reynolds (and Richardson) number in the gas flow. However the resolution of these simulations limits the Reynolds number to more moderate values ($Re \approx 500$ for 100 K gas). Hence Kelvin Helmholtz instabilities are unlikely to be present in these simulations. Kim & Ostriker (2006) also find that Kelvin Helmholtz instabilities are suppressed in a 3D stratified disk.

CHAPTER 5

The Formation of Molecular Clouds

The formation of molecular hydrogen in the ISM was first considered theoretically by Gould & Salpeter (1963). Since then H_2 has been detected, or more commonly inferred from the presence of other molecules, in various environments - including dark clouds, HII regions and galactic nuclei. As sites of star formation though, molecular clouds are of most interest for studying H_2 formation. Hollenbach et al. (1971) determined analytical expressions for the key processes involved in H_2 formation, upon which subsequent models of molecular gas in the ISM are generally based. Further progress in understanding the process of H_2 formation on grains may come from laboratory experiments, which have recently been developed. For molecular cloud formation, most models consider interstellar shocks (e.g. Hollenbach & McKee 1979), since these produce the high densities and low temperatures favourable for abundant H_2.

The previous chapter analysed the formation of dense clouds in spiral arms. This chapter examines whether these clouds are likely to be molecular. The chapter begins by describing how molecular hydrogen forms, before introducing an algorithm from Bergin et al. (2004) which calculates the rate of H_2 formation. This algorithm incorporates the density and temperature of the ISM, as well as parameters for interstellar grains, to compute the formation rate on grains. Expressions for the photodissociation and cosmic ray ionization rates then determine the destruction of H_2. The algorithm is applied to the simulations shown in Chapter 4 to model the evolution of H_2 over the galactic disk. In this chapter, the conditions necessary for H_2 to form on galactic scales are discussed, and the distribution of molecular hydrogen across the disk illustrated. The structure of molecular clouds is highlighted, and described in terms of the analysis in Chapter 4.

The results presented here can be compared with observations of molecular clouds. The location of the molecular clouds is shown, and compared with recent surveys of the Milky Way. Further comparison of the properties of individual molecular clouds is given in Chapter 6.

5.1 The formation of H_2

Molecular hydrogen (and the other 100 or so more complex molecules) forms in the ISM by a process of recombination on dust grains. Hydrogen atoms bind to the surfaces

of interstellar dust grains, such as ices, silicates or carbonaceous materials, and then combine to form molecules by diffusing across the surface, or quantum tunnelling. The rate of molecular formation is determined (Hollenbach et al., 1971) by

$$R_G = \frac{1}{2}\gamma n_H < v_H > n_{grain} < \sigma_g > \tag{5.1}$$

where n_H and n_{grain} are the number density of hydrogen atoms and grains, and $< \sigma_g >$ the mean grain cross section. The term $< v_H >$ is the thermal speed of the hydrogen atoms and so $n_{grain} < v_H > n_{grain} < \sigma_g >$ represents the frequency of collisions of hydrogen atoms with dust grains. The parameter γ is the recombination efficiency which represents the fraction of hydrogen atoms which successfully recombine to form molecules after binding to a dust grain. Hydrogen atoms do not necessarily recombine to form H_2 as they may be evaporated from the grain surface first. Most of these terms are typically replaced by constants to give

$$R_G = R n_H n \tag{5.2}$$

where n is the total number density of atomic and molecular hydrogen and R a constant of order 10^{-17} cm^{-3} s^{-1}. This assumes a constant grain size, and that the number density of grains is proportional to the total number density. The recombination efficiency is commonly chosen to be 0.3 (Hollenbach et al., 1971). More detailed results show that the recombination efficiency is likely to be higher for temperatures < 300 K (Cazaux & Tielens, 2002, 2004), and may also increase when including a range of grain sizes (Lipshtat & Biham, 2005). A further indication of the formation rate of H_2 on grains can now be provided by laboratory experiments (Pirronello et al., 1999; Vidali et al., 2004) which support the view that H_2 occurs readily for temperatures of < 300 K and can determine the efficiency of recombination for different types of grains. However for this thesis, which provides a first approximation to this problem, these more recent developments have not been included.

The processes which convert molecular hydrogen back to atomic gas are equally important to molecular cloud formation and morphology as molecular formation. The 2 dominant mechanisms are photodissociation from UV radiation and cosmic ray ionization (Hollenbach et al., 1971). Photodissociation is dependent on the strength of the UV field, determined by the proximity of massive stars, and the density of molecular gas. Where the column density of molecular hydrogen is high, self shielding reduces the amount of UV rays reaching the inner parts of the cloud. Likewise the cosmic ionization rate is dependent on the density of molecular gas and the cosmic ray ionization rate.

The formation of molecular hydrogen has predominantly been considered for interstellar shocks (Shu et al., 1972; Aannestad, 1973; Hollenbach & McKee, 1979; Koyama & Inutsuka, 2000; Bergin et al., 2004). These usually refer to shocks from stellar winds or supernovae, but galactic scale spiral shocks also occur in the ISM. This chapter investigates whether spiral shocks are likely to produce significant H_2. High Mach number shocks in the ISM will compress the gas sufficiently to reach the densities required for H_2 formation. This process is investigated analytically in Hollenbach & McKee (1979). For an adiabatic shock, they find H_2 forms rapidly on grains for densities of $n \geq 10^3$ cm^{-3}, providing the temperature is < 100 K. This includes a treatment of grain heating by UV rays and line cooling from important molecular coolants such as H_2, CO, OH and H_2O. Numerical models of shocks by Koyama & Inutsuka (2000), with 10^4 K gas, show that a thin dense

layer of H_2 occurs inside the shock-compressed gas resulting from a thermal instability, although the densities are too low for more extensive H_2 formation. Bergin et al. (2004) highlight the importance of self-shielding and thus determine a timescale of 10-20 Myr necessary to assemble a column density sufficient to shield H_2 from photodissociation.

As discussed in Chapter 1, there are several theories for molecular cloud formation, where the primary mechanism for the formation of H_2 does not necessarily involve shocks. Gravitational or magnetic instabilities may lead to dense regions of gas where molecular formation will occur. Estimates of the internal pressure and self gravity of a cloud by Hartmann et al. (2001) find that the density needed for molecular gas to form is similar to the density at which self gravity becomes important. In their model though, the molecular gas is still considered to form through colliding flows. Self gravity then rapidly produces stars in the densest regions. A similar scenario occurs in simulations by Glover & Mac Low (2006b), who find that molecular gas is formed first through turbulent compressions in the gas, before self gravity causes local collapse, on timescales of 1-2 Myr. An alternative is that molecular clouds form slowly (5-10 Myr) by gravitational collapse from initially static conditions (Glover & Mac Low, 2006a).

This thesis includes galactic-scale dynamics, but uses a simple model for the ISM and the formation of H_2. The latter is calculated from an algorithm (Bergin et al., 2004) which requires the density, column density and temperature of the gas, but not the detailed chemistry such as the density of different species and corresponding cooling rates. Nevertheless Bergin et al. (2004) find that the equations described in the next section agree well with their detailed calculations, which examine photoelectric, cosmic ray and X-ray heating and cooling from collisions of C, O H^+, CO and H_2 with electrons and hydrogen atoms. As described in Chapter 1, there have been several numerical simulations that have considered the detailed physics of the ISM on smaller scales. Those of Glover & Mac Low (2006a,b) mentioned above have also included the transition of atomic to molecular gas, for simulations of 20-40 pc cubes over timescales of < 10 Myr. They use a similar approach to that described here to calculate the formation of molecular gas, and photodissociation rate. However, unlike these simulations, the formation of H_2 is included explicitly by the cooling and heating of the gas.

5.1.1 Molecular gas density

The algorithm of Bergin et al. (2004) provides the rate of change of H_2 density

$$\frac{dn(H_2)}{dt} = R_{gr}(T) n_p n(H) - [\zeta_{cr} + \zeta_{diss}(N(H_2), A_V)] n(H_2) \tag{5.3}$$

where n is the number density (of atomic or molecular hydrogen), N is the column density (of atomic or molecular hydrogen) and T the temperature. The total number density is n_p, where $n_p = n(H) + 2n(H_2)$. Molecular hydrogen is produced through condensation onto grains, determined by the first term on the right of Equation 5.3. R_{gr} is the formation rate on grains, $2.2 \times 10^{-18}\ S\ T^{0.5}$ (Bergin et al., 2004) where $S = 0.3$ is the recombination efficiency. Destruction of H_2 occurs through cosmic ray ionization and photo-dissociation, represented by the second term on the right of Equation 5.3. The cosmic ray ionization rate, ζ_{cr} is assumed constant ($\zeta_{cr} = 6 \times 10^{-18}$ s^{-1}).

Following Bergin et al. (2004), the approximation of Draine & Bertoldi (1996) is adopted for the H_2 dissociation rate:

$$\begin{aligned} \zeta_{diss}(N(H_2)) &= \zeta_{diss} f_{shield}(N(H_2)) e^{-\tau_{d,1000}} \zeta_{diss}(0) \\ f_{shield}(N(H_2)) &= \frac{0.965}{(1+x/3)^2} + \frac{0.035}{(1+x)^{0.5}} \\ &\quad \times \exp[-8.5 \times 10^{-4}(1+x)^{0.5}] \\ \text{where} \quad x &= N(H_2)/5 \times 10^{14} \text{cm}^{-2} \end{aligned} \tag{5.4}$$

The function f_{shield} is a measure of the self shielding of the gas, dependent on the column density, $N(H_2)$. To determine the self shielding, the rate of photodissociation is summed over all energy levels for a given density. The approximation f_{shield} is found to be in good agreeement with the full model (Draine & Bertoldi, 1996). The term $\tau_{d,1000}$ is the dust extinction at 1000 Åand $\zeta_{diss}(0) = 4.17 \times 10^{-11}$ s^{-1} is a measure of the strength of the UV field. This formulation assumes that the background UV spectrum is the same as that of a B0 star, and that the radiation flux is constant everywhere. The strength of the flux is measured by the magnitude of $\zeta_{diss}(0)$. This is a very approximate measure of the the photodissociation rate, which should ideally vary depending on the local level of star formation. The column density $N(H_2)$ is found in the disk calculations by multiplying the local H_2 density by the scale height of the disk. This again only provides an estimate of the column density.

Before considering the galactic disk simulations shown in Chapter 4, Equation 5.3 was investigated for a linear shock. This was to check the behaviour of Equation 5.3 for different densities and temperatures, and provide comparison with Bergin et al. (2004) (Figure 13). Similar to Bergin et al. (2004), a shock is considered with pre-shock density $n_0 = 1$ and velocity $v_0 = 15$ km s^{-1}. Figure 5.1 shows the H_2 number density relative to the total number of hydrogen atoms for different initial densities and temperatures. The self-shielding approximation of Draine & Bertoldi (1996) is used in all these calculations. As expected, the time for significant H_2 to form decreases as the post-shock density n_p increases.

The right hand plot of Figure 5.1 then shows calculations where the post-shock density is fixed at 1400 cm^{-3}, but the temperature of the shock is allowed to vary. Since in Equation 5.3, the formation rate of H_2 on grains depends on the sound speed, the amount of H_2 formed increases with temperature. This at first seems contradictory from the idea of molecular gas forming in cold dense gas. However, firstly, the recombination efficiency decreases at higher temperatures (Cazaux & Tielens, 2004), since the hydrogen atoms are expected to evaporate from the grains before H_2 can form. In Equation 5.3, the recombination efficiency is constant, overpredicting the H_2 formation at higher temperatures. Secondly, the rate of H_2 formation has a greater dependence on the density ($\propto n^2$). For lower temperatures, the Mach number of shocks, and subsequently density, increases. As shown in Section 5.2, this has much more effect than the change in temperature, even without allowing the recombination efficiency to vary.

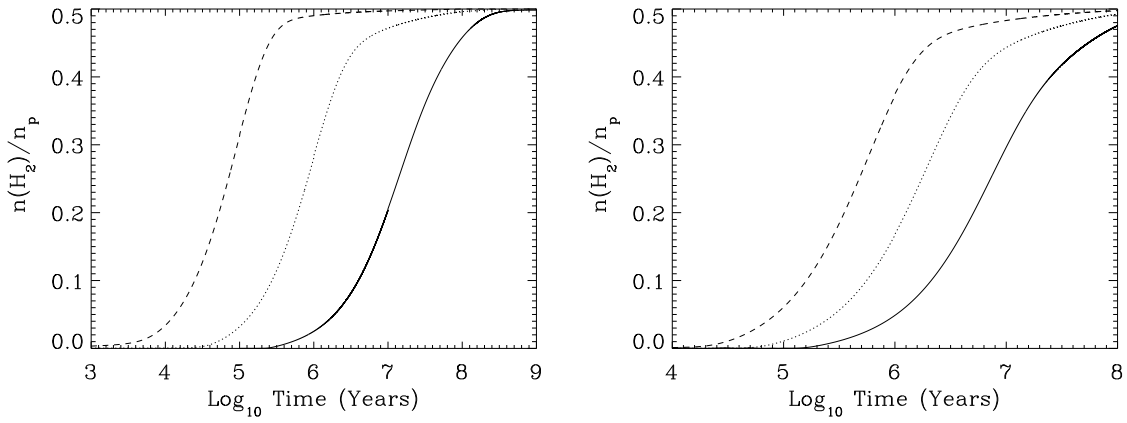

Figure 5.1: Plots showing the behaviour of Equation 5.3 for different densities (left) and temperatures (right). The left hand plot assumes the temperature of the shock is 20 K, whilst the density in the shock is 10^{-20} g cm^{-3} (n_p=6000 cm^{-3}) (dashed line), 10^{-21} g cm^{-3} (n_p=600 cm^{-3}) (dotted line) and 10^{-22} g cm^{-3} (n_p = 60 cm^{-3}) (solid line). The right hand plot assumes the density in the shock is 1400 cm^{-3} and the temperature is 10 K (solid line), 100 K (dotted line) and 1000 K (dashed line).

5.1.2 Application to simulations

The formation of H_2 is now considered for the galactic disk simulations, using Equation 5.3. The density of H_2 is post-processed in these calculations. The density and temperature of each SPH particle are available for each time frame in the simulations. Assuming that $n(H_2)$ is 0 everywhere initially. the ratio of molecular to atomic gas is calculated at each successive time. The density of molecular gas is taken from the previous time frame and as mentioned above, provides an estimate of the column density $N(H_2)$. This ratio of the number density is then converted to a volume density for each particle in each time frame.

Figure 5.2 shows the molecular gas fraction plotted against density for 1/10th of the particles in the 50 K simulation. This figure shows that Equation 5.3 mainly selects the most dense particles, although the molecular gas fraction is also time dependent. Since the formation of H_2 is not instantaneous, the molecular gas fraction increases with the time gas spends in the denser spiral arms. The fraction of molecular gas is also shown with time for a few particles in Figure 5.3. The particles are initially located in the same part of the disk. They reach a fraction of approximately 50% H_2 in the spiral arms. Between the first and second spiral arm, the H_2 is not fully dissociated, but between the second and third spiral arms, the H_2 fraction is negligible.

In the next sections, the outcome of H_2 density is calculated for different temperatures, before concentrating on the high resolution 50 K run. Since self gravity is not included, the mass of the disk can be changed and new values of the H_2 density calculated. Similarly the level of photodissociation can be increased or decreased.

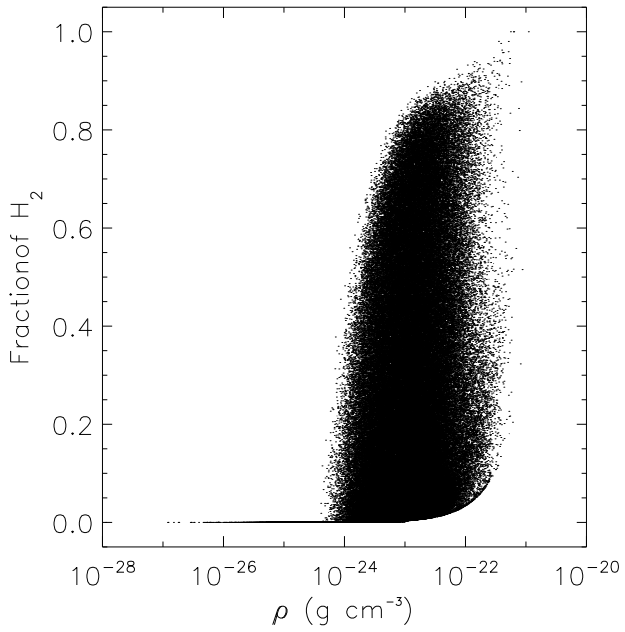

Figure 5.2: The distribution of the molecular fraction of particles is shown versus their density for the 50 K simulation, after 100 Myr. 1/10th of particles are plotted, i.e. 4×10^5. There is a clear cut off at $\rho \sim 10^{-24}$ g cm^{-3}, below which the gas is totally atomic. The large spread in the H_2 fraction for a given density represents the time evolution of the H_2 fraction from when low density gas first enters the spiral shock.

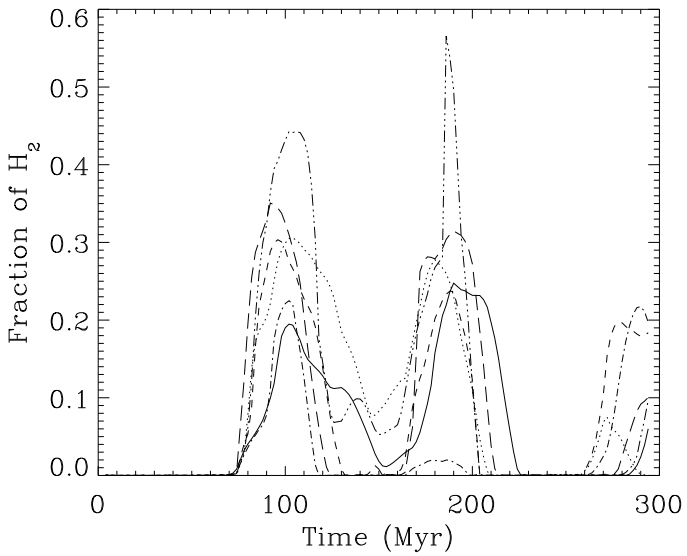

Figure 5.3: The molecular fraction is shown with time for 6 particles from the 50 K simulations. The particles are initially chosen from similar positions in the disk.

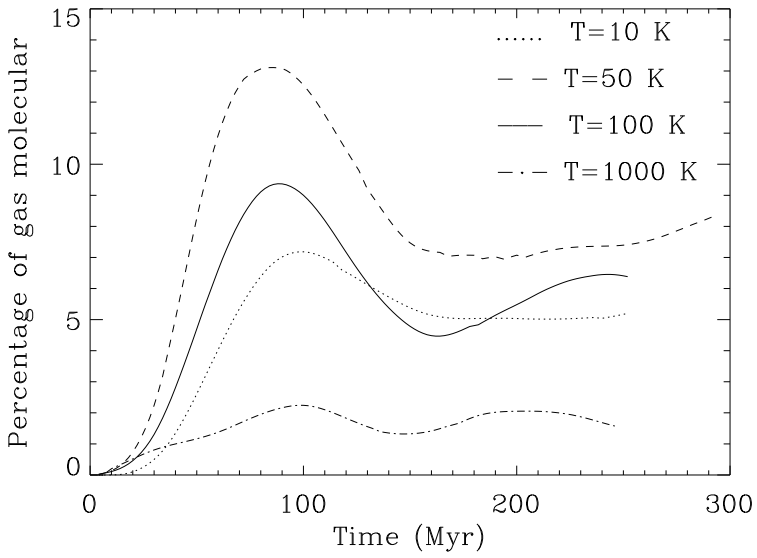

Figure 5.4: The total percentage of H_2 with time is shown for simulations with gas temperatures of 10, 50, 100 and 1000 K. The number of particles in the 10, 100 and 1000 K simulations is 10^6, whilst the 50 K simulation contains 4×10^6 particles.

5.2 Dependence of H_2 formation on temperature

Figure 5.4 shows the total percentage of molecular hydrogen in the disk as a function of time, for gas at 10, 100 and 1000 K with 10^6 particles, and at 50 K with 4×10^6 particles. The highest mass of H_2 forms for the 10, 50 and 100 K gas, when the densities in the shock are much higher, whilst at 10^4 K, almost no molecular gas is present. The location of the molecular gas is shown in Figure 5.5 after 100 Myr for the 10, 100, and 10^3 K simulations, for a quarter of the disk.

With 1 million particles, approximately 6-9 % of gas in the disk is molecular at temperatures of 10-100 K. The fraction of molecular hydrogen increases at higher resolution, the 50 K simulation producing a maximum of 13% H_2, or 6.5×10^7 $M_\odot$. When the temperature is increased to 1000 K, this fraction drops to 1 or 2 % and is negligible for the 10^4 K simulation. When the gas is hot, the shock produced by the spiral potential is weaker, so the density of gas in the spiral arms is reduced. The density in the 10^4 K simulation does not increase above 10^{-24} g cm^{-3} which, as indicated by Figure 5.2, is too low for molecular hydrogen to exist, at least for the timescales gas is situated in the spiral arms. Although the formation of H_2 is still apparent in the calculations, the density of gas in the spiral arms at 10^4 K is insufficient for self-shielding to occur and molecular gas is readily photodissociated. Similar conclusions were reached by Bergin et al. (2004), who require sufficient densities of gas to allow effective self shielding.

There is overall slightly less H_2 at 10 K compared to 100 K formation since at low sound speeds, H_2 does not form efficiently on grains. The rate of formation of H_2 on grains, R_g, is determined by the rate of collisions of atoms (Hollenbach et al., 1971), which decreases with lower temperatures. However, as mentioned in the previous section, the

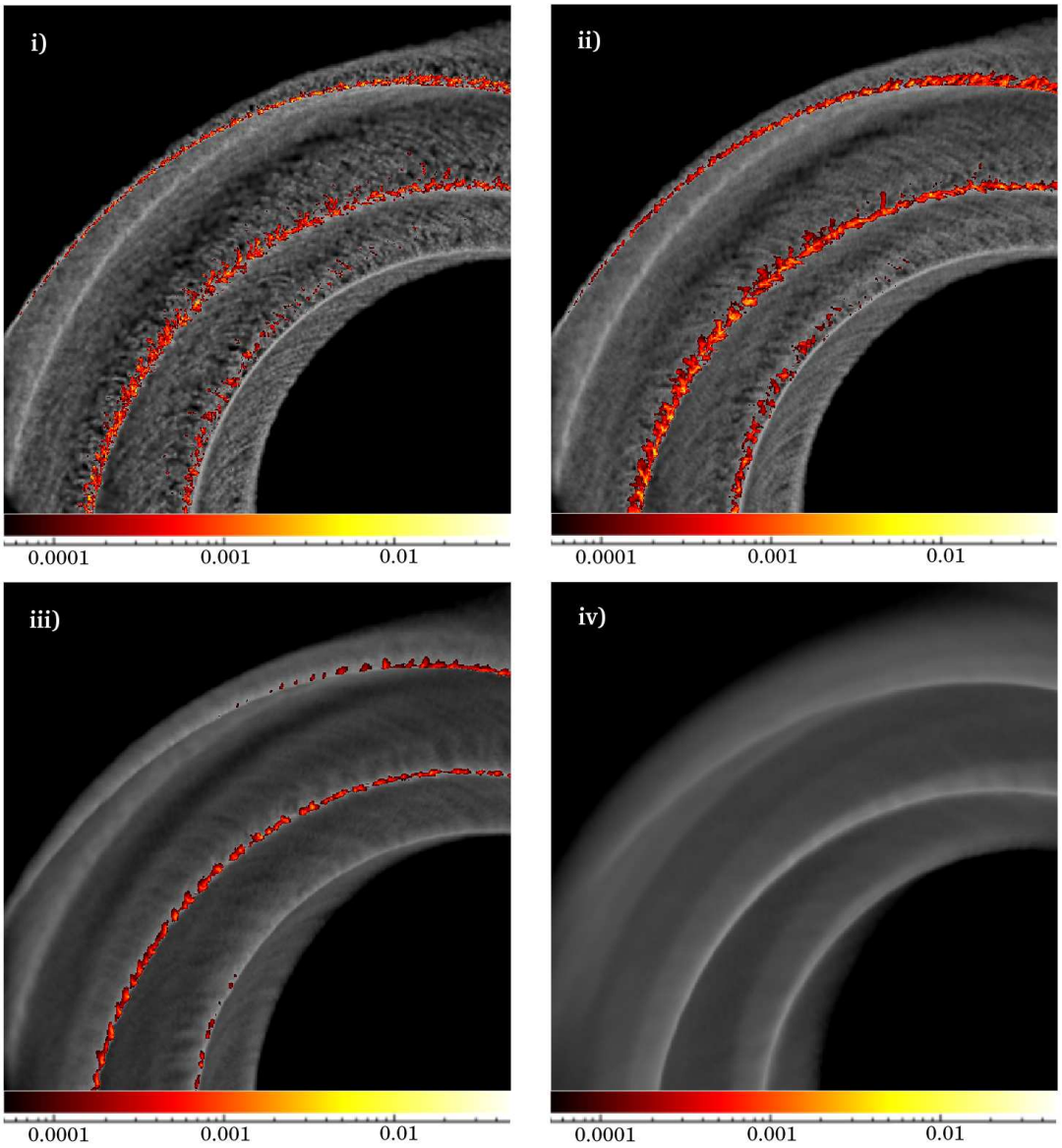

Figure 5.5: Column density plots (g cm^{-2}) showing density of molecular hydrogen (red) against overall density (black and white). The temperature of the disk is i) 10 K, ii) 100 K, iii) 10^3 K, iv) 10^4 K. The xy-coordinates assume a Cartesian grid centred on the midpoint of the disk which remains fixed with time. Gas is flowing clockwise across the disk.

efficiency of grain formation is assumed here to be a constant, S=0.3. This can actually be as high as $S \sim 1$ for $T < 20$ and as low as $S \sim 0.1$ for $T > 100$ K (Cazaux & Tielens, 2004). Thus in reality the recombination efficiency is likely to be higher for lower temperatures ($\sim$ 10 K), and increase the mass of H_2. Furthermore, at higher temperatures, the recombination efficiency and therefore H_2 fraction are overestimated. This only emphasises the conclusion that the hot gas (T$>$ 1000 K) does not form significant H_2, due to the dynamics of the shock.

The isothermal assumption precludes a detailed study of the temperature dependency on H_2 formation, which requires a realistic equation of state. However for strong shocks performed at 10^4 K (Koyama & Inutsuka, 2000) which do include cooling, only a thin layer of molecular hydrogen forms. At higher temperatures, it is unlikely that spiral shocks could produce densities sufficient for significant molecular hydrogen formation, even with cooling of the gas.

5.3 High resolution simulation

The remainder of this chapter focuses on the 50 K highest resolution simulation. The location of H_2 when the ISM temperature is 50 K is shown in Figure 5.6. There are 4×10^6 particles giving a mass resolution of 125 $M_\odot$ per particle. This figure is taken after 100 Myr, and shows the global distribution of molecular gas, and the small scale structure of molecular clouds.

Molecular hydrogen starts to form immediately in the spiral arms, the most dense parts of the disk. H_2 is first situated in a narrow strip, where the shock from the spiral density wave occurs. The density of gas leaving the arms is insufficient to prevent molecular gas quickly becoming photodissociated, hence the molecular gas is solely confined to the shock in the spiral arm. This strip of molecular hydrogen is smooth and continuous along the spiral arm. However, as the simulation progresses, denser structures become apparent in the arms. These break up into separate clumps of molecular gas, which are identified as 'molecular clouds'. As the simulation progresses, dense structures leaving the spiral arms become sheared. Some regions of molecular gas leaving the spiral arms are then dense enough for self shielding to reduce the rate of photodissociation. These molecular clouds survive further into the interarm regions (e.g. those moving away from the inner spiral arm in Figure 5.6).

The formation of these molecular clouds is thus due to the dynamics of the spiral shock, as described in Chapter 4, rather than magnetic or gravitational instabilities. The spiral arm structure is induced by the spiral shock and the transfer of angular momentum between particles travelling through the potential. This produces dense clouds which are predominantly molecular. The molecular clouds in turn have highly irregular structures, also due to the dynamics of the spiral shocks. These structures resemble observations of large scale molecular cloud morphology, although no feedback effects such as stellar winds are included in these simulations.

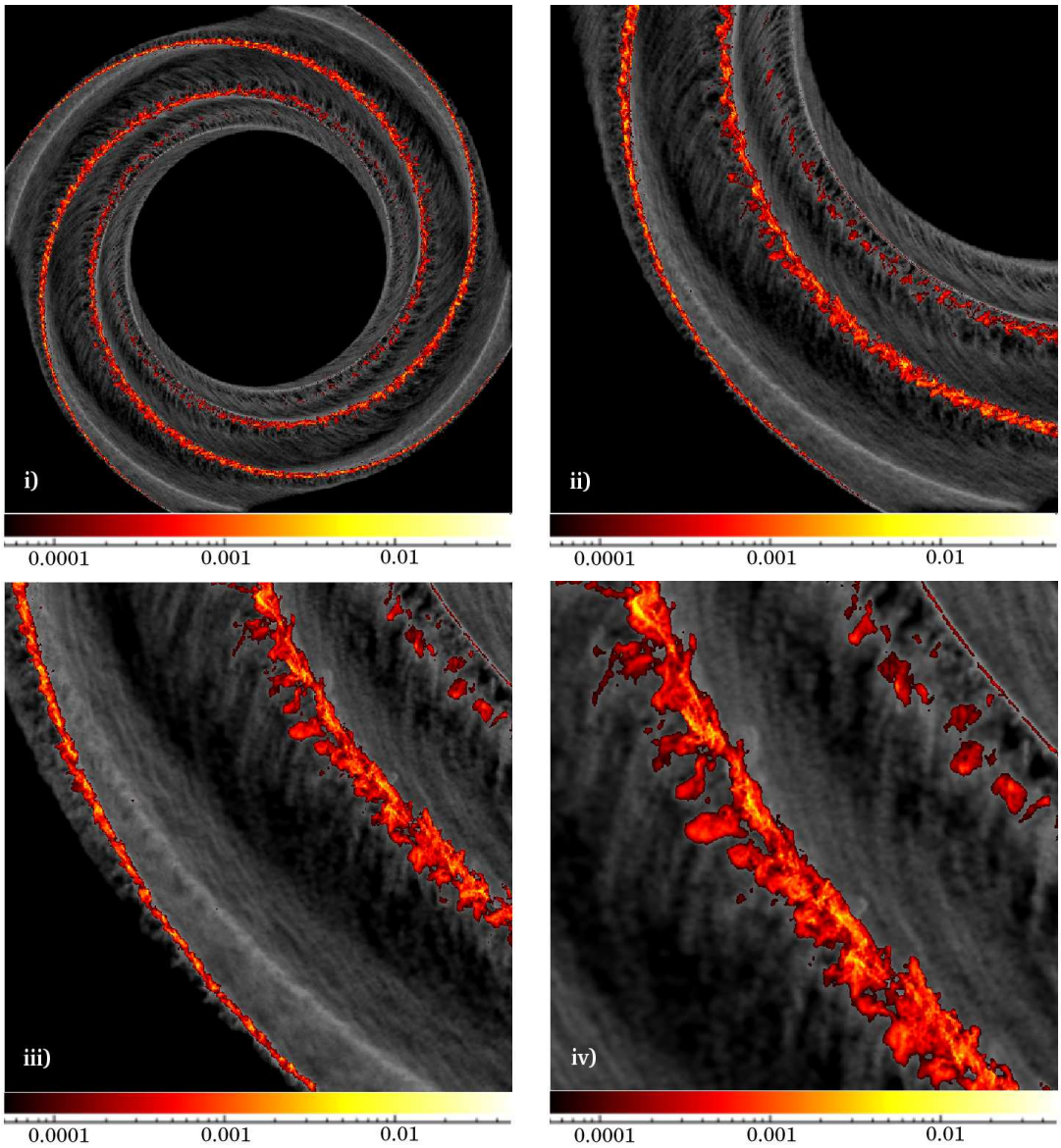

Figure 5.6: Column density plots (g cm^{-2}) showing density of molecular hydrogen (red) against overall density (black and white). Length-scales of plots are i) 20 kpc $\times$ 20 kpc, ii) 10 kpc $\times$ 10 kpc, iii) 5 kpc $\times$ 5 kpc (-8.5 kpc $< x <$ -3.5 kpc, -8.5 kpc $< y <$ -3.5 kpc), iv) 3 kpc $\times$ 3 kpc (-6.5 kpc $< x <$ -3.5 kpc, -6.5 kpc $< y <$ -3.5 kpc). The xy-coordinates assume a Cartesian grid centred on the midpoint of the disk which remains fixed with time. Gas is flowing clockwise across the disk.

5.3.1 Molecular gas and spiral arms

Figure 5.6 shows that molecular gas is largely confined to the denser spiral arms. This is examined further by calculating the variation of the average molecular densities and average total densities as a function of azimuth. The particles are selected from a ring centred at $r = 7.5$ kpc with $\triangle r = 200$ pc, the same as described in Section 4.7.2. The ring is then divided into 100 segments, each of length $r\triangle\theta = 500$ pc and area 9×10^4 pc^2, and the average molecular and total (molecular and atomic) gas densities for each segment calculated. The results are shown in Figure 5.7, after 100 Myr and at the end of the simulation, 290 Myr. This plot only displays the mean molecular and atomic densities - the peak densities are 10-20 times higher. The interarm densities of H_2 are 100-10^3 times smaller than in the spiral arms after 290 Myr, whilst the total densities are ≈ 50 times smaller. After 100 Myr, 13% of the gas in the ring is molecular. Approximately 70% of the total amount of gas is situated in the spiral arms, of which approximately 20% is molecular.

The width of the spiral arm and the time the gas remains in the molecular phase can be estimated from Figure 5.7. Since a circular region was selected, the spiral arms appear disproportionately wide. The width of the spiral arm is approximately $d \sin\alpha$ where d is the width estimated from Figure 5.7 ($\triangle\theta_{arm} r$) and α is the pitch angle (15^o). This gives an estimated spiral arm width of ≈ 1 kpc, which includes both the narrow shock and structure behind the shock. With a velocity perpendicular to the arms of ≈ 10 km s^{-1}, the time to cross this higher density region is around 100 Myr. Only the most dense regions remain significantly molecular over the whole period (as the gas is distributed in clumps rather than uniformly over this region) - typically a particle only exhibits a high molecular ratio for ≈ 20 Myr corresponding to a local width of 200 pc.

5.3.2 Dependence of H_2 formation on total disk mass and photodissociation rate

The mass of H_2 in Equation 5.3 is determined by the density, photodissociation rate and temperature. The cosmic ray ionization rate, $\zeta_{cr} = 6 \times 10^{-18}$ s^{-1}, is found to have a minimal effect on the fraction of molecular to atomic gas. Since the H_2 mass is determined post process, calculations can be repeated with a different disk mass (as there is no self gravity) and/or different photodissociation rate. The effect of altering these values on the total mass of molecular hydrogen is displayed in Figure 5.8. The mass of H_2 increases considerably to over 1.4×10^9 M$_\odot$, 28% of the total gas, when the disk mass increases by a factor of 10. In comparing with the photodissociation rate, the same approximation (Equation 5.4) was applied, but increased or decreased by a constant factor. When the photodissociation rate decreases by a factor of 10, the molecular mass increases to 1.25×10^8 M$_\odot$, 25% of the total gas mass.

In both these cases, with parameters more favourable to H_2 formation, the mass of molecular gas does not stabilise. The total H_2 mass continues to increase and is greatest at the end of the simulation. This suggests that molecular gas does not become fully dissociated in the interarm region. As the disk becomes more disordered with time, more dense clumps emerge from the spiral arms into the interarm regions. With a higher disk mass, or lower photodissociation rate, these clumps exhibit a higher proportion of H_2.

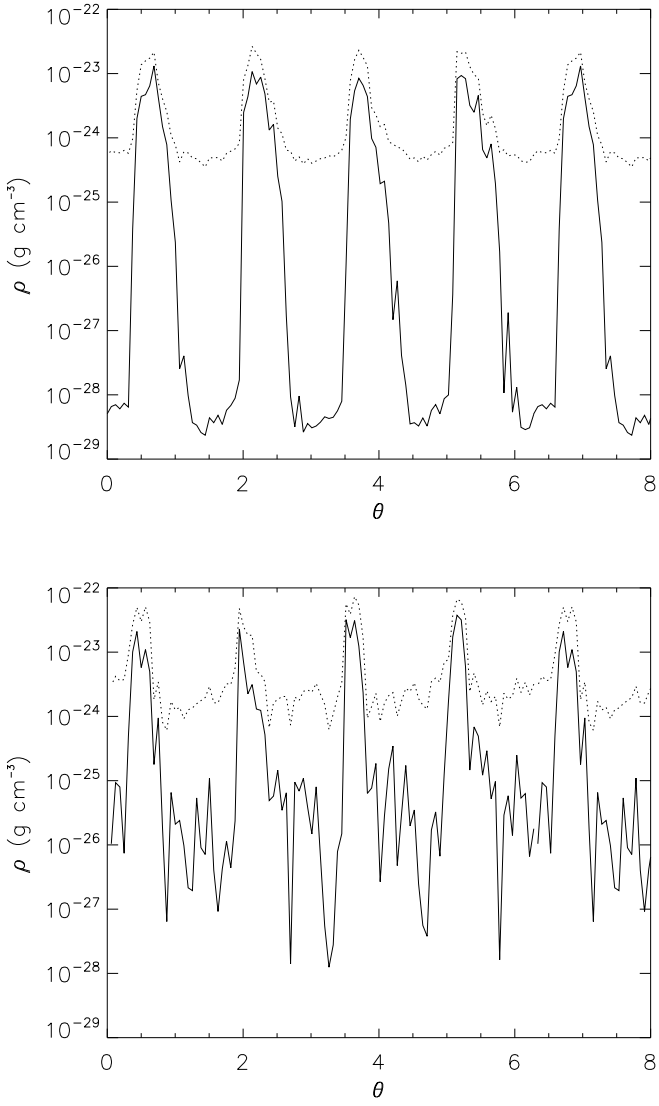

Figure 5.7: Density of molecular gas (solid) and total density (dotted) are plotted against azimuth (θ), where θ is the angle measured in the direction of flow. The density plotted is the average over an annulus centred at r=7.5 kpc with δr=200 pc. The time of the simulation is 100 Myr (top) and 290 Myr (bottom).

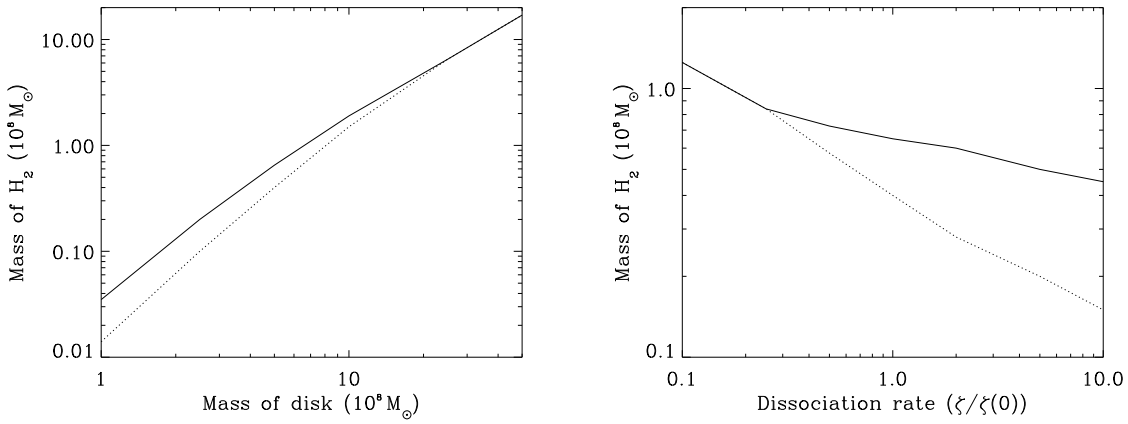

Figure 5.8: Formation of H_2 compared to the total mass of the disk, and rate of photodissociation compared with Draine & Bertoldi (1996) ($\zeta(0)$). Left: Maximum mass of H_2 (solid) and total H_2 mass at the end of the simulation (dotted) versus mass of the disk. The disk mass of 5×10^8 $M_\odot$ corresponds to a surface density of ≈ 2 $M_\odot$ pc^{-2}. Right: Maximum mass of H_2 (solid) and total H_2 mass at the end of the simulation (dotted) versus photodissociation rate.

Figure 5.9 shows the arm and interarm ratios of the H_2 gas density to the total gas density as a function of the disk mass and photodissociation rate. The disk mass has a substantial effect on the fractional abundance of H_2 in the spiral arms. When the mass of the disk increases to 5×10^9 $M_\odot$, nearly all of the gas in the spiral arms is molecular at the end of the simulation. Whilst the interarm ratio of the total density to H_2 density also increases, only 1/10th of the interarm gas is molecular. The increase in both the arm and interarm regions is due to higher densities increasing the formation of H_2.

The photodissociation rate has a more pronounced effect on the interarm ratios. When the photodissociation rate is a tenth of that taken from Draine & Bertoldi (1996), approximately a quarter of the interarm gas is molecular at the end of the simulation. By contrast the amount of H_2 in the spiral arms changes much less. This difference at a lower photodissociation rate arises when the gas is not fully dissociated between the spiral arms. Molecular gas can survive for longer into the interarm regions leading to some molecular structures between the arms. This is illustrated in Figure 5.10, which displays part of the 50 K simulation where the molecular gas density is calculated with the lower photodissociation rate. Clumps of molecular gas are shearing away from the spiral arm. In addition, molecular material is arriving at the spiral arm which has not fully dissociated from the previous spiral arm passage.

The arm to interarm ratio of H_2 is approximately 10^3 applying the original disk mass (5×10^8 $M_\odot$) and photodissociation rate. When the disk mass increases by a factor of 10, this ratio decreases to 100. Decreasing the photodissociation rate by a factor of 10 decreases the arm to interarm ratio to approximately 70.

These results indicate that the molecular gas is strongly confined to the spiral arms. However a more complete treatment of H_2 formation, which includes heating and cooling, will give a more accurate idea of the quantitative analysis of molecular hydrogen (Glover

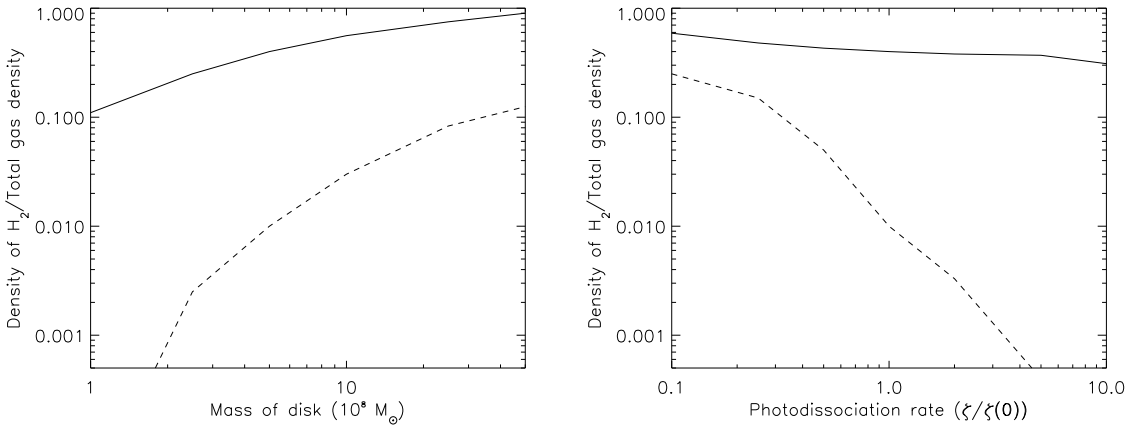

Figure 5.9: Fractional abundance of H_2 in the arm (solid) and interarm regions (dotted) compared to the total disk mass (left) and photodissociation rate (right). These figures are taken from the end of the simulation.

& Mac Low, 2006a,b). Nevertheless the effects of increasing the disk mass or decreasing the level of photodissociation are likely to hold. The possibility that molecular hydrogen is transmitted between spiral arms cannot be ruled out though, e.g. if the photodissociation rate is sufficiently low.

5.4 Observational comparison of molecular cloud properties

One of the objectives of these simulations is to see how well the spiral shocks reproduce the observations of molecular clouds. The results of these simulations can be directly compared with molecular clouds in the Milky Way. The distribution of molecular clouds is considered from a local standard of rest comparable to the Sun, and a further LSR at the edge of the disk. Several surveys of molecular clouds in the Milky Way have been undertaken (e.g. Dame et al. 1986, 2001; Lee et al. 2001). The simulated data is compared with 2 sets of results: i) the FCRAO CO survey of the outer galaxy (Heyer et al., 1998). This survey detected molecular clouds between the Galactic longitudes $102^o.49$ and $141^o.54$ which are located predominantly in the local and Perseus arms; ii) a CO molecular line survey (Yang et al., 2002), which detected cold infrared sources over the northern plane of the Galaxy (longitudes between 0^o and 260^o).

The post-processed calculations provide the fraction of molecular gas for each particle in the galactic disk. Groups of particles are classified into molecular clouds, the location and extent of which are determined from a grid. A section of 1/8 of the disk is selected as a sample, and divided into a 5 pc resolution grid. The total fraction of molecular gas in each cell is calculated and cells which contain over 10 $M_\odot$ of H_2 are retained. All groups of adjacent cells satisfying this threshold are defined as a single molecular cloud. The properties of each 'cloud', including mass, position and velocity are tabulated. The V_{LSR} of each molecular cloud is also determined. The locations of each LSR chosen are shown on Figure 5.11 compared to the overall distribution of molecular clouds.

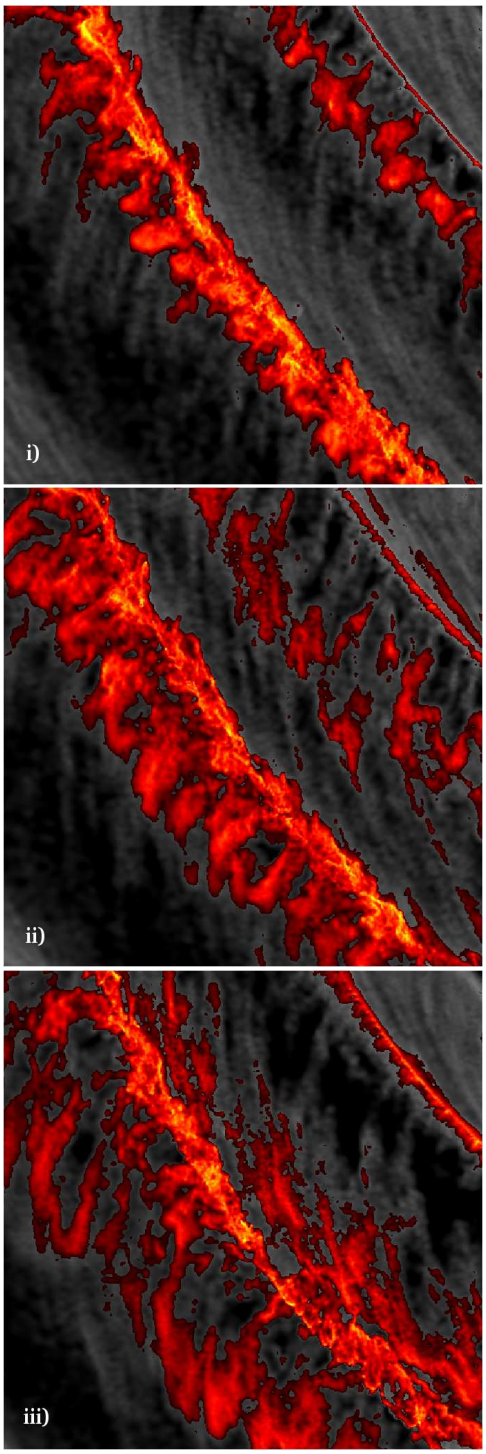

Figure 5.10: A 3 kpc by 3 kpc region of the disk showing the transfer of molecular hydrogen between spiral arms. The photodissociation rate is 1/10 that of Draine & Bertoldi (1996) and as a consequence, there is more molecular hydrogen surviving between the spiral arms. The column density of molecular hydrogen (red) and total density (black and white) are displayed (same scale as Figure 5.5). The times of each plot are i)100 Myr, ii)120 Myr and iii)140 Myr. Plot i) is the same time, region and scale as Figure 5.6(iv), but using a lower photodissociation rate. The increased density of H_2 along the arms leads to molecular structures within the interarm regions which are absent from the simulation in Figure 5.6.

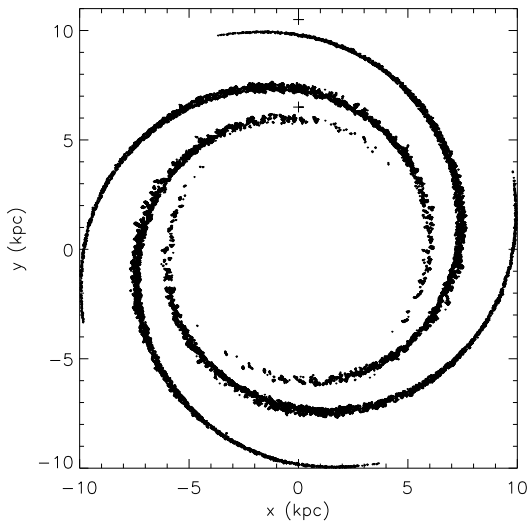

Figure 5.11: The position of each local standard of rest (crosses) is compared to the overall distribution of molecular clouds. The LSR situated at (0,6.5)kpc is comparable with the position of the Sun, in an interarm region in the mid-part of the disk. The second LSR (0,10.5)kpc produces a distribution of clouds as viewed from the edge of the disk.

In Figures 5.12 & 5.13, typical results from these calculations are compared with the FCRAO CO survey and the CO molecular line survey (where the LSR is situated at Cartesian coordinates (0,6.5)kpc). The grid based method gave a total of 5044 objects within the sample criterion. Next to these results, corresponding data from the FCRAO CO survey is shown, where there are 7724 objects and the molecular line survey, where there are 1331 objects. The data from the simulation and the 2 surveys show clear bands, where the molecular clouds have preferential radial velocities due to the spiral arm structure. The molecular clouds in the models are more confined to the spiral arms than in the observational data, particular for the outer arm. We have assumed a co-rotation radius of 11 kpc, which may reduce the spiral arm shock at larger radii.

Figure 5.14 displays the molecular clouds as viewed from outside the disk, at coordinates (0,10.5)kpc. This is more comparable with Stark & Lee (2006), who observe clouds in the inner regions of the Milky Way. However their survey incorporates 5 spiral arms, whereas only 2 are clear in Figure 5.14.

More details of the individual cloud properties are provided in the next chapter, which discusses 2 phase simulations and compares the clouds formed in the 50 K simulation with the 2 phase results. The resolution of these simulations though is not very high for comparing the properties of individual clouds.

5.5 Summary

The last 2 chapters have provided a model for the formation of molecular clouds in the spiral arms of galaxies. These dense clouds of gas form through the dynamics of spiral

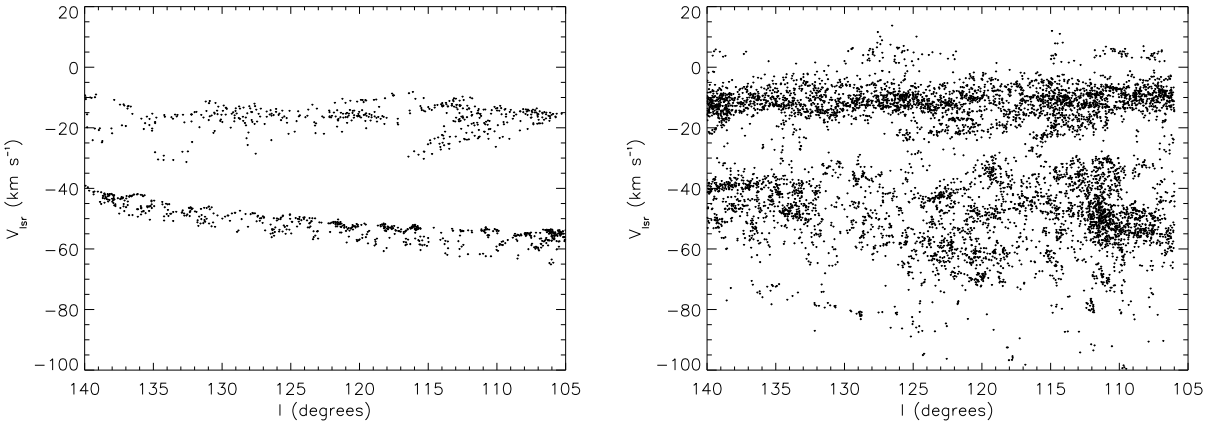

Figure 5.12: V_{lsr} plotted against galactic longitude for molecular clouds from these simulations and the FRCAO CO survey. The left plot shows the simulated data, with a LSR at coordinates (0,6.5)kpc. The right plot uses data from the FCRAO CO survey (Heyer et. al. 1998).

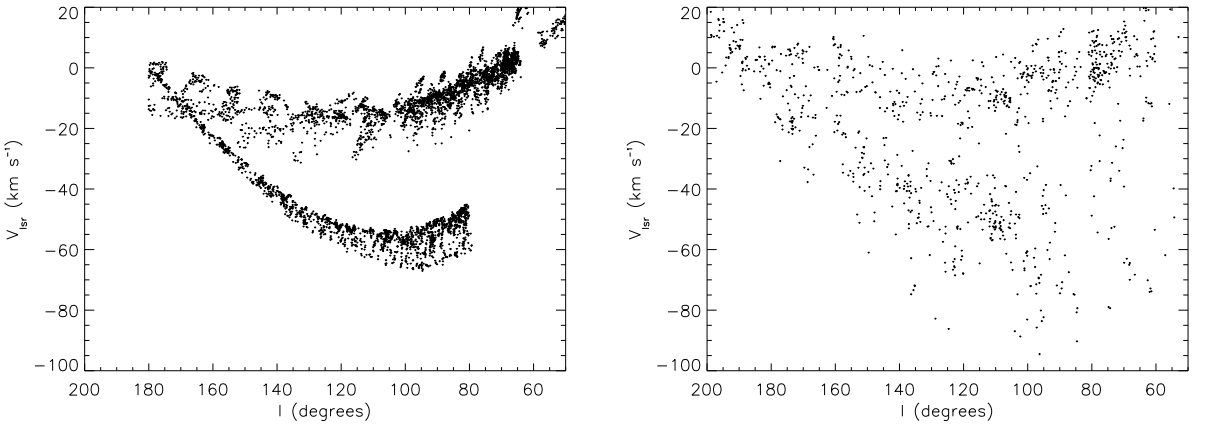

Figure 5.13: V_{lsr} plotted against galactic longitude for molecular clouds from these simulations and the CO molecular line survey. The left plot shows the simulated data, with a LSR at coordinates (0,6.5)kpc. The right plot uses data from (Yang et. al. 2002).

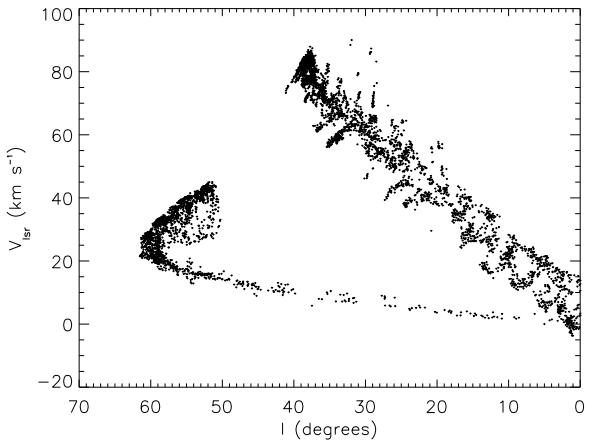

Figure 5.14: V_{rms} plotted against galactic longitude from simulated data. The LSR was chosen at coordinates (0,10.5)kpc

shocks, which also induce a velocity dispersion in the gas comparable with observations. Approximately 10 % of the 5×10^8 $M_\odot$ disk in these simulations is molecular hydrogen, predominantly located in the dense clouds in the spiral arms. Increasing the disk mass or decreasing the photodissociation rate by a factor of 10 roughly doubles this fraction. These figures though are potentially lower limits on the amount of molecular hydrogen formed in these models, since the total percentage of molecular hydrogen increases with resolution. A further caveat is that realistic heating and cooling, and feedback, which are likely to have some effect, are not included.

Since molecular gas formation is determined by density, and the time spent in dense regions, molecular gas is largely confined to the spiral arms. Typically the ratio of arm to interarm molecular hydrogen is 2 or 3 orders of magnitude. However a reduced photodissociation rate allows the survival of molecular gas into the interarm regions, and a ratio of arm to interarm molecular hydrogen of around 5. This leads to the possibility of molecular gas passing from one arm to the other and potentially determining subsequent molecular cloud formation.

This mechanism for forming molecular clouds does not require instabilities from self-gravity or magnetic fields. Instead the prerequisites for both the dynamical formation of clouds, and that they are molecular is that the gas is cold (< 1000 K), so the gas is sufficiently compressed by the spiral shock, and initially inhomogeneous. The assumption of a lower temperature is not inconsistent with observations, since as shown in Chapter 1, a substantial fraction of the ISM is ~ 100 K gas, although this gas occupies only a small filling factor. The ISM is also known to be highly inhomogeneous. The high resolution of these simulations enhances the detailed morphology of these molecular clouds. Furthermore, since previous authors have typically assumed temperatures of order 10^4 K, the degree of structure apparent in these simulations has not previously been observed. However, the main weakness of these results is the simplification of the ISM as an isothermal single phase medium. The next chapter describes a simulation with warm and cold gas, which although still isothermal, with no gas in transition between the 2 phases, shows some notable differences from the single phase calculations presented thus far.

CHAPTER 6

Molecular cloud formation in a multi-phase medium

The previous chapters described isothermal, single phase simulations. As discussed in Chapter 1, the ISM consists of gas over a range of temperatures, traditionally interpreted as a 3 phase medium. This chapter describes a simulation which contains hot (10^4 K) and cold (100 K) gas. The difference in structure, and molecular gas content, is highlighted between this simulation and the single phase cold simulations.

This chapter also includes details of the properties of individual molecular clouds, although this is limited to some degree by the resolution of the simulations. The molecular clouds are identified using 2 different clump-finding algorithms. The cloud radii and mass are determined, and the clump mass spectra shown. The properties of the clouds are compared for the multi-phase simulation and the previously described single phase 50 K simulation. For the multi-phase simulations, clouds in the spiral arm and interarm regions are compared, and their densities related to observational results.

6.1 Details of the multi-phase simulation

The multi-phase simulation is set up the same as described in Chapter 4, except the gas is distributed in 2 phases, a cold component of $T = 100$ K, and a warm component of $T = 10^4$ K. Each phase constitutes half of the gaseous mass of the disk, 5×10^8 $M_\odot$, so the total mass of the disk is 10^9 $M_\odot$. This corresponds to a nominal surface density of ~ 4 $M_\odot$ pc^2. The total HI surface density at the solar radius is ~ 5 $M_\odot$ pc^2 (Wolfire et al., 2003). The SPH particles are initially randomly assigned as hot or cold gas, but the distribution settles into a diffuse warm and dense cold phase as the simulation progresses. The total number of particles used in the simulation is 6 million, again with 3 million distributed in each component. The simulation is isothermal, so there is no heating or cooling of gas between the 2 phases (gas particles remain at the same temperature throughout the simulation).

6.2 Structure of the disk

The column density section of the disk of the multi-phase simulation is shown in Figure 6.1 at different times. The small scale features present at the earliest time are seen to grow into self consistent structures. These column density plots include both the 100 and 10^4 K gas. The 100 K gas is most clearly visible in small clumps whilst the 10^4 K gas provides a diffuse background and the smooth component of the spiral arms. The 2 components are shown explicitly in Figure 6.2, which plots the particles representing the hot and cold gas separately for a section of the disk after 100 Myr. Both figures show that the cold gas is confined by the pressure from the hot component into small dense clumps. The hot gas on the other hand is much more uniform and smooth. Thus each phase shows structure similar to that expected from the single phase results in Chapter 4. Two further differences are apparent for the spiral shock for each component. As can be seen in Figure 6.2, the shock for the cold gas is offset from the shock corresponding to the hot gas. However the shock from the hot component is evidently affecting the cold gas clumps, as can be seen from the elongation of the cold gas clumps as they enter the spiral arm (Figure 6.2). The shock for the hot gas is also much wider, whereas the cold gas forms a very narrow spiral arm. Again this is due to the different strengths of the shock for each component.

Figure 6.3 shows the distribution of mass with density for the multi and single phase simulations after 100 Myr. The greater mass at low densities for the multi-phase simulation corresponds to the hot component of gas. The higher mass at high densities, compared to the single-phase disk is due to the confinement of the cold gas to higher densities by the hot component.

Whilst the distribution of hot gas changes little with time, the structure of the cold gas varies. Until approximately 60 Myr (Figure 6.1a), the cold gas is fairly regularly distributed in small clumps across the section of disk, with an increased concentration in the spiral arms. Unlike the single-phase simulations, where the gas is clumpy due to the particle nature of the code, the warm phase here confines the cold gas into dense clumps. For the single-phase calculations, the clumpiness in the spiral arms is amplified with time by the dynamics of the shock. In these multi-phase calculations however, the spiral shock acts rather to organise these clumps into more coherent structures. These are perhaps more easily visible as the larger features shearing away from the spiral arms in Figures 6.1b and c. By 220 Myr (Figure 6.1c) the 100 K spiral arm clumps have been sheared into thin filaments between the arms, whilst new structures are breaking away from the spiral arm.

Molecular gas density

Column density plots for the simulation are shown after 100 Myr in Figure 6.4. The column density of molecular hydrogen is highlighted in red. Figure 6.4 shows more clearly the difference in structure of the cold gas in the single and multi-phase simulations, in particular by comparing Figure 6.4 iv) and the equivalent frame of the single-phase simulation (Figure 5.6 iv, Chapter 5). The multi-phase gas is much more structured, with many smaller scale clumps visible. There are also small clumps of cold gas strewn across the interarm regions. Gas in the single-phase interarm regions is sheared into spurs and

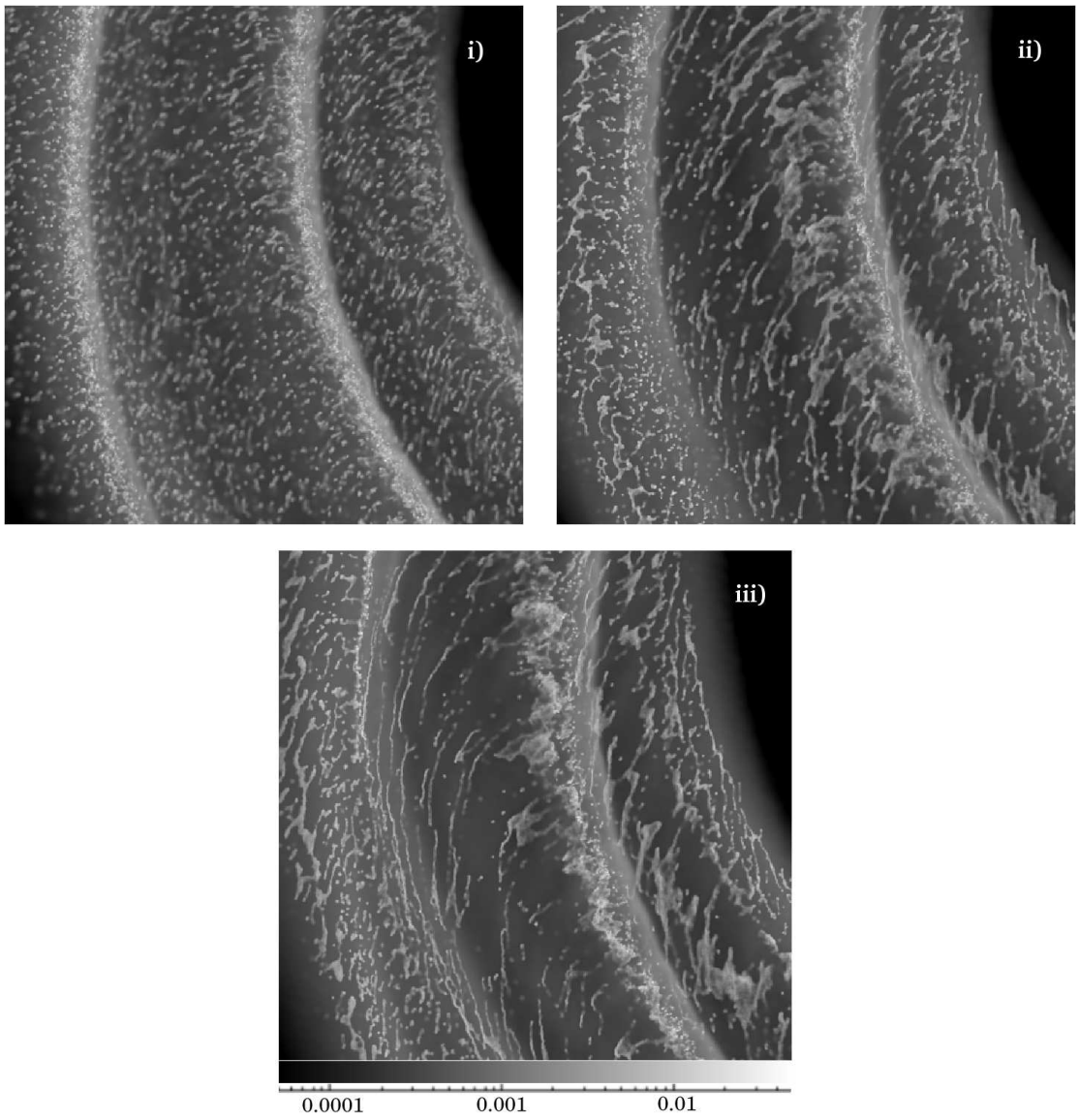

Figure 6.1: Column density plots (g cm^{-2}) showing a 5 kpc by 5 kpc section of the disk (with Cartesian coordinates -9 kpc $< x <$ -4 kpc and -5 kpc $< y <$ 0 kpc. The xy-coordinate grid is centred on the midpoint of the disk and remains fixed with time. Gas is flowing clockwise across the disk, i.e. from bottom to top. The time corresponding to each plot is i) 60 Myr, ii) 140 Myr and iii) 220 Myr. The plots show 100 and 10^4 K gas.

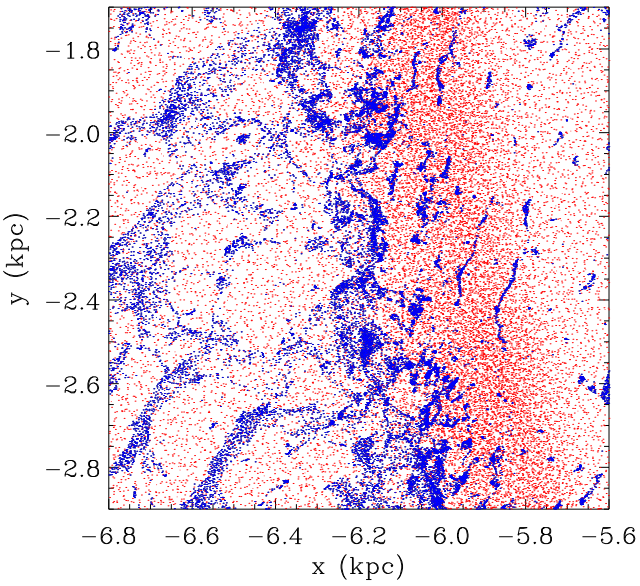

Figure 6.2: The particle positions are shown for a section of the disk, assuming a Cartesian grid centred on the midpoint of the disk. The 2 phases are plotted, 100 K (blue) and 10^4 K (red) after 100 Myr.

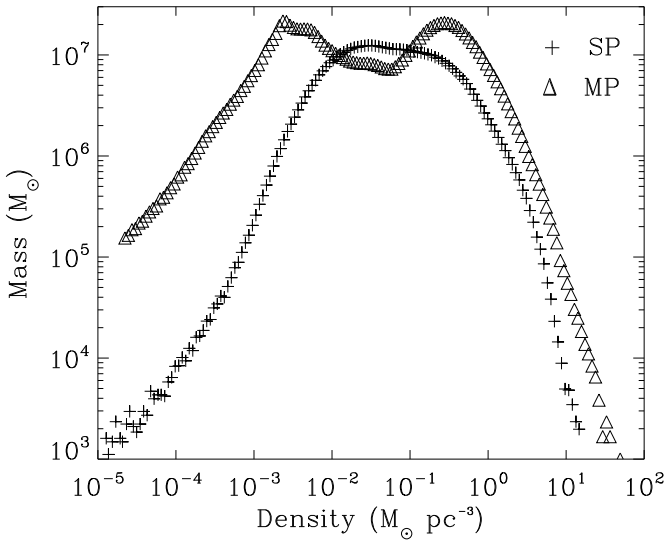

Figure 6.3: The distribution of mass as a function of gas density is shown after 100 Myr for the single and multi-phase simulations. The nominal density for molecular clouds is 2.5 $M_\odot$ pc^{-3}.

feathering, but individual clumps and structures are much more defined in the multi-phase medium. The cold gas assembles into longer, more coherent, very thin spurs in the interarm regions at later times in the multi-phase calculation (Figure 6.1c).

The molecular hydrogen corresponds to 12% of the total mass, i.e. 1.2 $\times 10^8$ $M_\odot$ and 24% of the cold gas. Most of the clumps of cold gas are overplotted with the molecular hydrogen column density. The most striking difference between these results and those of Chapter 5 is the greater amount of molecular gas. The fraction of molecular gas is approximately twice that of the single-phase simulation after 100 Myr. Unlike the single-phase calculations, the cold gas is confined by the pressure from the hot gas and remains more dense in the interarm regions. Consequently there is less photodissociation of H_2, and higher densities of molecular gas are produced between the spiral arms. As seen from Figure 6.4 iii) and iv), the molecular gas does not become fully dissociated between the spiral arms, unlike the single-phase medium. The mass of molecular gas continues to rise throughout the multi-phase simulation, unlike the single-phase results, which peaked after about 100 Myr. As the gas is not fully dissociated between the arms, the total molecular gas density continues to increase after multiple spiral arm passages. By the end of the simulation the fraction of molecular gas appears to be converging to approximately 25 % of the total mass or equivalently 50 % of the 100 K gas (2.5×10^8 $M_\odot$).

Figure 6.5 shows the density of the 100 K gas (total HI and predicted H_2), the predicted H_2 density and the 10^4 K gas density as a function of azimuth. These are the average densities, calculated over a ring centred at 7.5 kpc, of width 200 pc and divided into 100 segments. This figure again shows the much higher density of H_2 in the interarm regions compared to the single-phase medium (Figure 5.11, Chapter 5) with the density of H_2 now 1/10th of the total cold HI + H_2 gas in the interarm regions. The mass of molecular gas is now approximately 1/3 of the total mass of cold gas in the spiral arms, and 1/5 in the interarm regions. Figure 6.5 further shows the difference in location of the shocks, as the density of the hot gas peaks at a lower azimuth than the cold gas.

Figure 6.6 shows the typical timescale gas spends with different fractions of H_2. The average time for each fraction of H_2 is determined from the duration particles exceed that fraction of H_2 during each simulation. The typical time gas contains over 50% molecular hydrogen is around 40 Myr for the single phase simulation and 60 Myr for the multi-phase simulation. These times decrease to approximately 5 and 10 Myr for gas which contains over 90% molecular hydrogen.

6.2.1 Structure in the cold gas

This section considers quantitatively the structure in the cold gas for the multi-phase medium, as well as the gas in the 50 K simulation. The properties of clumps from each simulation are compared, using 2 clump finding algorithms. Both algorithms are grid based, assuming a 2D grid over the galactic disk. The first (hereafter CF1) selects clumps solely using a density threshold, whilst the second (hereafter CF2) uses neighbour lists to assign the most dense grid cells and their neighbours to clumps. For CF1, the density in each grid cell is calculated and all the cells above a certain density threshold are selected. Cells that are adjacent are grouped together and particles within these cells classed as a

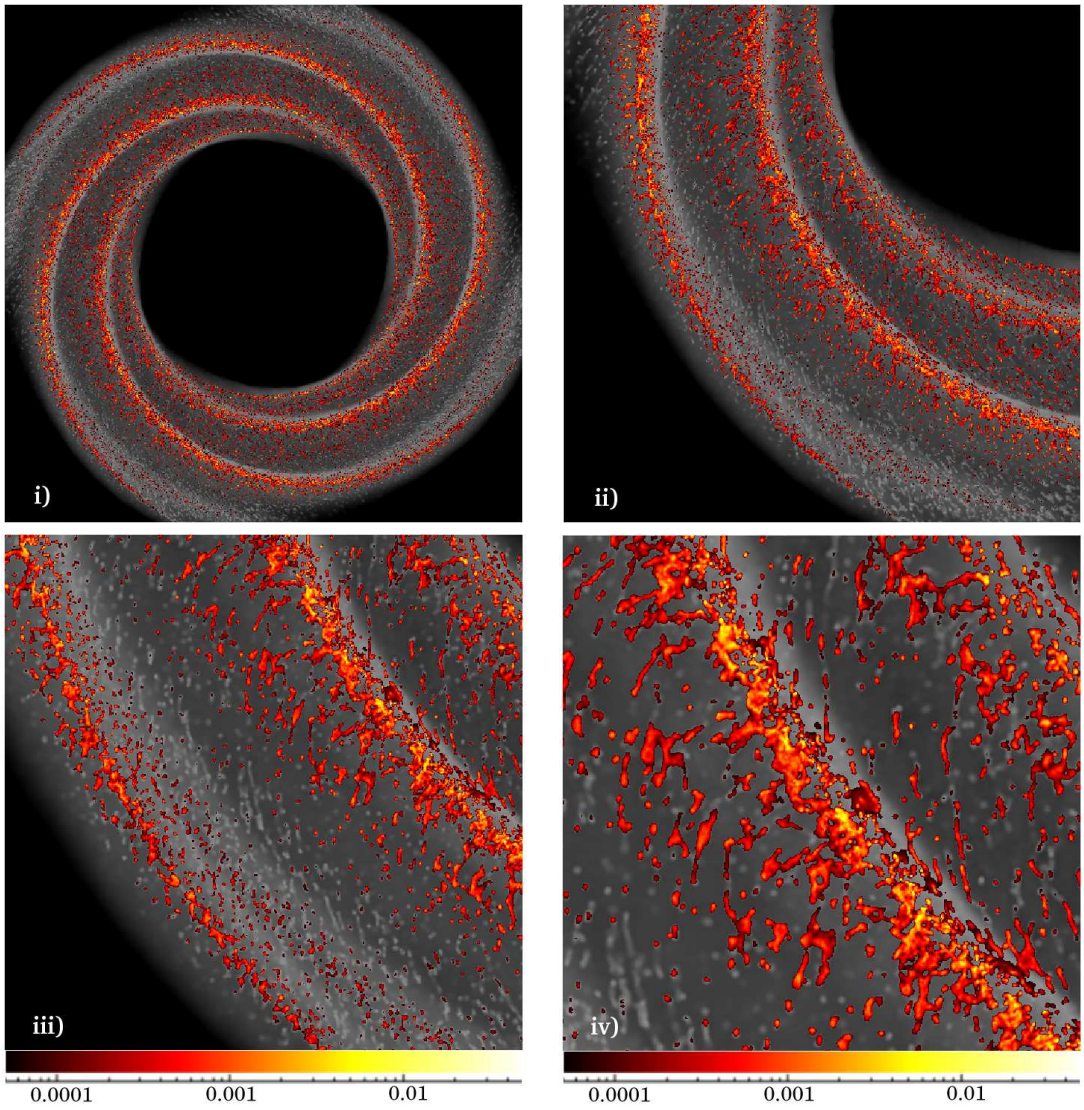

Figure 6.4: Column density plots (g cm^{-2}) showing density of molecular hydrogen (red) against overall density (black and white). Length-scales of plots are i) 20 kpc $\times$ 20 kpc, ii) 10 kpc $\times$ 10 kpc, iii) 5 kpc $\times$ 5 kpc (-8.5 kpc $< x <$ -3.5 kpc, -8.5 kpc $< y <$ -3.5 kpc), iv) 3 kpc $\times$ 3 kpc (-6.5 kpc $< x <$ -3.5 kpc, -6.5 kpc $< y <$ -3.5 kpc). The xy-coordinates assume a Cartesian grid centred on the midpoint of the disk which remains fixed with time. Gas is flowing clockwise across the disk.

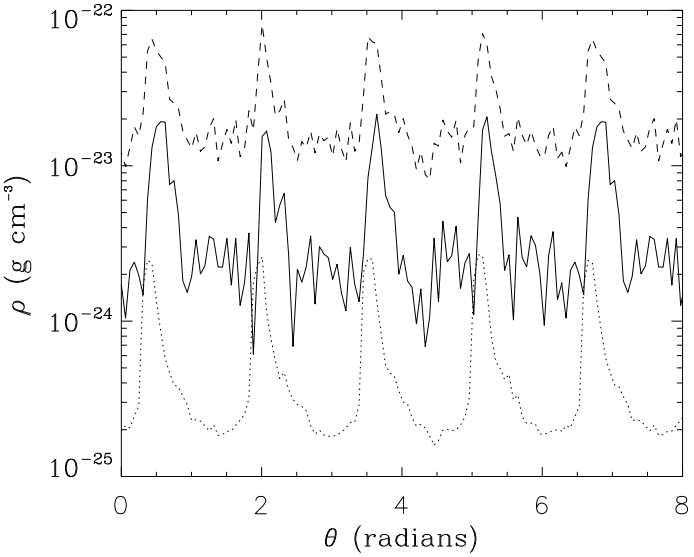

Figure 6.5: The average density is plotted versus azimuth, calculated for a ring centred at 7.5 kpc. The density of the 10^4 K gas (dotted), 100 K (dashed) (including HI and H_2) and H_2 (solid) are shown.

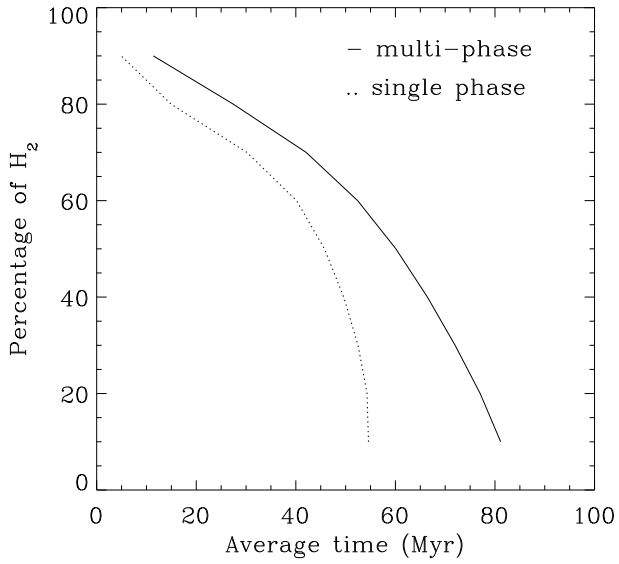

Figure 6.6: The typical time over which gas contains over a certain fraction of H_2 is shown in this figure. For each percentage of H_2, the average time is calculated from all particles which exceed that fraction of H_2 during each simulation.

clump. CF2 was provided by Paul Clark and is based on the clumpfind method of Williams et al. (1994). The SPH densities are first smoothed onto a 2D grid. The grid cells are then ordered by decreasing density. For each cell in turn, the cell and its neighbours (subsequently removed from the list) are identified as a clump, or assigned to a previously defined clump. Again a density threshold was set which removed low density clumps. The properties of each clump are then calculated from the grid cells rather than the actual SPH particles. In both cases the density is for the molecular gas, which as seen from Figure 6.4 largely reflects the underlying structure. The properties of these clumps can then be compare with observed molecular clouds.

The clumps found using CF1 are displayed for the multi-phase (Figure 6.7) and the single-phase medium (Figure 6.8) for a subsection of the disk (the same section is shown in Figure 6.2). Both these figures are taken after 100 Myr. The resolution of the grid for the algorithm is 5 pc, and the density threshold for each cell is 100 $M_\odot$, i.e. equivalent to a surface density of 4 $M_\odot$ pc^{-2}. Each clump consists of the SPH particles which lie within cells above the density threshold. For Figures 6.7 and 6.8, only clumps with more than 30 particles (corresponding to a total hydrogen mass of 5000 $M_\odot$) are shown. The corresponding column density plots indicating the molecular gas column density are also shown (Figures 6.7 and 6.8, right).

There is a clear difference in structure of this section of the disk for the single and multi-phase gas. The multi-phase case shows many smaller clumps along the spiral arm, whilst the single-phase plot consists of 3 large clumps and several smaller clumps. There are 88 clumps consisting of over 30 particles for the multi-phase distribution compared to 23 for the single-phase case. The clump finding algorithm also picks out several clumps in the interarm regions in the multi-phase simulation, whereas there are none for the single-phase results. These figures further show the general distribution of cold gas. In the multi-phase simulation, the cold gas occupies a much smaller filling factor, located in small dense clumps, particularly in the interarm regions. By contrast, in the single-phase case, the cold gas is much more uniform in the interarm regions. The second algorithm, CF2, generally produced smaller clumps, but with similar results.

6.2.2 Properties of molecular gas clumps

The properties of the clumps from the single and multi-phase simulations are now examined. The results shown use CF1, but differences with the second clump-finding algorithm are discussed. The clump properties are determined atfer 100 Myr. The mass and radii for the clumps from the 2 simulations are shown in Figure 6.9. At later times the clump masses increase for the multi-phase simulation, as there is a higher fraction of H_2, while those of the single phase simulation are similar.

For both clump-finding algorithms, the column density threshold is ~ 4 $M_\odot$ pc^{-2}. For CF1, this corresponded to taking a grid of resolution 5 pc and requiring that each cell contains at least 100 $M_\odot$ (of H_2). For CF2, the same grid resolution is used with a minimum column density of 0.001 g cm^{-2} of H_2. With CF1, each clump corresponds to a group of SPH particles. The radii shown in Figure 6.9 are determined by calculating the radius which contains 3/4 of the total clump mass, and thus the mass plotted is 3/4

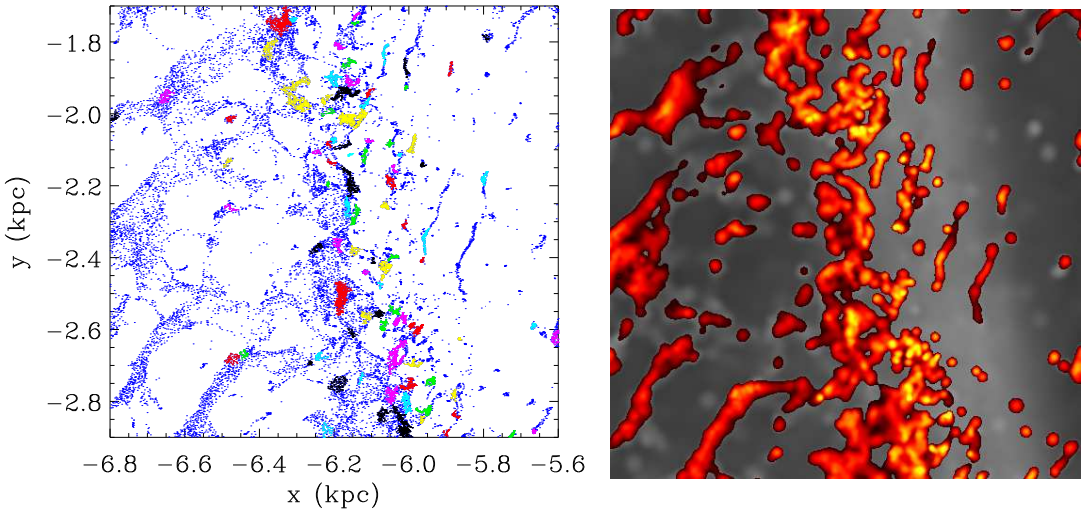

Figure 6.7: The left panel shows the distribution of clumps found using the clump-finding algorithm CF1 for a 1.2 by 1.2 kpc subsection of the disk after 100 Myr. The particles corresponding to the 100 K gas are plotted in dark blue, the 10^4 gas is not shown. The particles in each clump are overplotted in a different colour. The right panel shows the corresponding column density image, using the same scale as Figure 6.4 with molecular hydrogen overplotted in red.

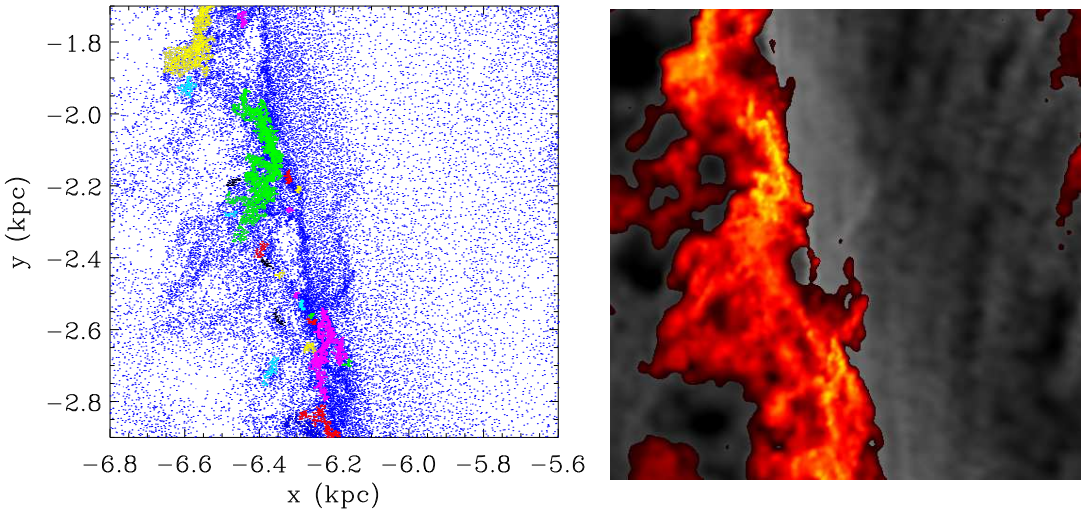

Figure 6.8: The left panel shows the distribution of clumps found using the clump-finding algorithm CF1 for a 1.2 by 1.2 kpc subsection of the disk after 100 Myr. This is taken from the single-phase (50 K) simulation. The dark blue points show all the particles in the simulation, but the particles in clumps are overplotted in different colours. The right panel shows the corresponding column density image, using the same scale as Figure 6.4.

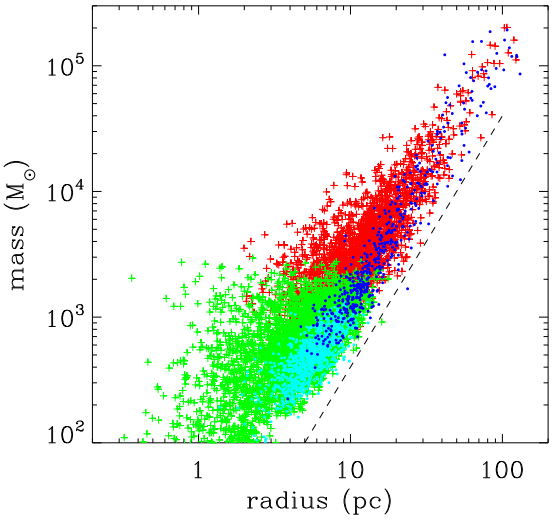

Figure 6.9: The mass and radius of the clumps are plotted using CF1 over a quarter of the disk. The clumps are selected at 100 Myr from the multi-phase (crosses) and single-phase (circles) simulations. The clumps contain > 30 particles (red/dark blue) or 10-30 particles (green/cyan). The dashed line indicates $\Sigma = 4$ M$_\odot$ pc^{-2}.

of the total clump mass assigned by the particles. Using the full or 1/2 clump radii and masses merely shifts the distribution of clumps to higher or lower masses and radii. For CF2, the effective radius is determined from the grid cells which make up each clump, i.e. $r_{eff} = \sqrt{Area/\pi}$ using the maximum extent of the x and y coordinates to calculate the area.

Figure 6.9 shows the mass versus radii from the clumps found in the multi and single phase simulations from a quarter of the disk. Clumps with > 30 particles and 10-30 particles are indicated. The resolution of the clumps is generally low and in particular the properties of the 10-30 particle clumps are unreliable. They appear to continue the trends of the larger clumps though, and emphasise that there will be a large number of lower mass clouds in these simulations as well. There are far fewer clumps in the single-phase simulation - less than 1/3 of the multi-phase simulation. However there are comparatively more larger clouds, as also indicated by Figures 6.7 and 6.8. The total mass of the clumps in Figure 6.9 for the single-phase simulation is 5.7×10^6 M$_\odot$ compared to 1.4×10^7 M$_\odot$ for the multi-phase simulation, over a quarter of the disk. The most massive clump after 100 Myr in both simulations was $\sim 3 \times 10^5$ M$_\odot$, with a radius of 150 pc. For the multi-phase simulation, the fraction of molecular hydrogen increases with time, so after 200 Myr, the maximum cloud mass is $\sim 6 \times 10^5$ M$_\odot$.

The clumps found using the second algorithm, CF2, follow a similar distribution to that shown on Figure 6.9. However there is less scatter and fewer more massive clouds. The clumps from both simulations, and from both algorithms follow a $M \propto r^2$ dependence, implying the clouds have constant surface densities of ~ 8 M$_\odot$ pc^{-2}. For comparison, the density criterion of 4 M$_\odot$ pc^{-2} is also shown. The apparent constant surface density of the clumps is likely to be a consequence of the density threshold applied to find the clumps. Increasing the threshold 10 times moves the distribution of clumps to correspondingly

smaller radii. The surface densities of molecular clouds from observational results (e.g. Heyer et al. 1998; Blitz et al. 2006) could similarly represent a selection effect based on the threshold antenna radiation temperature, T_R^*.

The resolution of most of the clumps was insufficient to calculate a velocity dispersion. However the better resolved clumps (with > 100 particles) contain velocity dispersions of a few km s^{-1}. The virial parameter

$$\alpha_G = \frac{5\sigma^2 r}{GM}. \tag{6.1}$$

was also calculated for the clumps. In both simulations, most of the clumps are unbound. However the more massive clumps tend to be more bound, with α_G typically < 10.

Figure 6.10 shows the mass spectrum from the 2 simulations, for the total number of clouds found over the whole of the disk (of > 30 particles) with CF1. Taking a mass spectrum $dN/dM \propto M^{-\alpha}$, $\alpha \sim 2.35$ for the multi-phase simulation. The clumps from the single-phase simulation produce a much shallower spectrum, of $\alpha \sim 1.6$. At later times, the spectrum for the single-phase simulation is similar, although the spectrum for the multi-phase simulation becomes shallower, with $\alpha \sim 2.15$ after 200 Myr, since there are more larger clouds at later times. Using CF2, the larger clumps divide into smaller clumps which truncates the clump masses at 1.5×10^5 M$_\odot$. Consequently the value of α increases to $\alpha \sim 3.3$ and $\alpha \sim 2.6$ for the multi and single-phase simulations respectively. The form of the power spectrum thereby appears to depend on the details of the clump-finding algorithm. What can be concluded however is that the multi-phase medium produces a steeper mass spectrum and fewer high mass clouds. Observations indicate that α lies in the range $\alpha = 1.5 - 1.8$ (Solomon et al., 1987; Heyer et al., 1998) for the Galaxy and up to $\alpha = 2.5$ for external galaxies (Blitz et al., 2006).

6.2.3 Interarm and spiral arm molecular gas

As mentioned previously, the multi-phase simulation produces a much greater degree of interarm molecular gas and a few of the clumps in Figure 6.7 are located in the interarm regions. The distribution molecular clouds (with > 30 particles) over the whole of the disk is shown in Figure 6.11. Again the clumps are found using CF1. There are a significant number of clouds in the interarm regions, especially in the inner regions of the disk where the spiral arms are closer together. For the outer parts of the disk, the interarm clouds tend to be situated on the edge of spiral arms. The ratio of interarm to arm clouds is approximately 1:7. The distribution of clouds and the interarm ratio was very similar for the second clump-finding algorithm. By contrast, for the single phase simulation, the clouds all lie along the spiral arms. The number of interarm clouds is sensitive to the photodissociation rate, so these figures only provide a rough indication. The photodissociation rate may be lower in the interarm regions, increasing the number of interarm clouds. On the other hand, the photodissociation rate will be higher where massive star formation occurs, which with the effects of feedback may disrupt molecular gas clouds before they enter the interarm regions.

The number of more massive clouds in the interarm and arm regions is also compared. Approximately 3% of interarm clouds were $> 10^4$ M$_\odot$ compared to 6% of clouds in

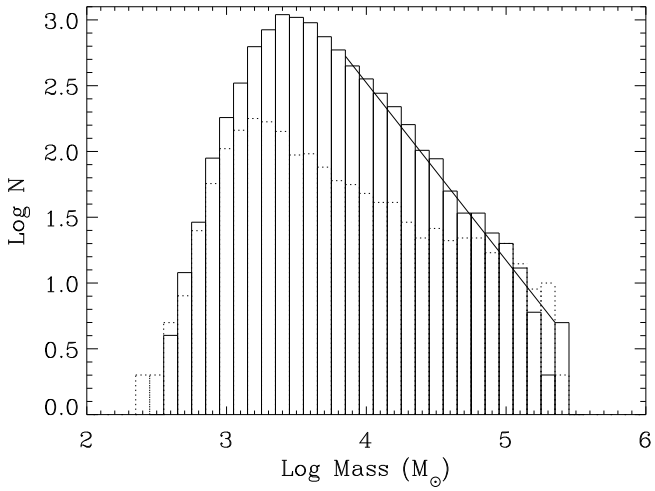

Figure 6.10: The clump mass spectrum is shown for all clumps from the multi-phase simulation (solid) and the 50 K simulation (dotted). Both are determined after 100 Myr and use CF1. A slope corresponding to $dN/dM \propto M^{-2.35}$ is also indicated.

the spiral arms. The cloud mass spectra for clouds located in the spiral arms and interarm regions are displayed in Figure 6.12. The spectrum for the spiral arm clouds is very similar to the spectrum for the total number of clouds, although slightly shallower with $\alpha \sim 2.25$. The spectrum for the interarm clouds however is much steeper with $\alpha \sim 2.9$, and a cut off in mass at around 3×10^4 M$_\odot$.

Much of the interarm molecular gas is not included in the clouds shown in Figure 6.11. Figure 6.7 indicates that the column density of this interarm molecular gas is between $5 \times 10^{-4} - 10^{-3}$ g cm^{-2}. This is slightly less than the H_2 column density estimated for HI self absorption (HISA) clouds (Klaassen et al., 2005). The HISA survey indicates features with little or no ^{12}CO emission, rather the H_2 column density requires determining from PDR models. The clouds located in the spiral arms obtain molecular gas column densities between $5 \times 10^{-3} - 10^{-2}$ g cm^{-2}, comparable with the lower values of mean column densities in molecular clouds (e.g. Heyer et al. 1998; Kawamura et al. 1998). Including self gravity and possibly higher resolution will produce denser regions in the spiral arms.

The density of the 100 K gas (inclusive of H_2) is on average 7×10^{-23} g cm^{-3} and $1 - 2 \times 10^{-23}$ g cm^{-3} for the spiral arm and interarm regions respectively (Figure 6.5). It is found from PDR models that CO (1-0) emission is applicable for determining H_2 densities when the total gas density is > 10 cm^{-3} (Allen, 2004). Most of the molecular gas in the spiral arms will therefore lie within this regime, whilst only the dense interarm H_2 is likely to correspond with CO measurements. Kaufman et al. (1999) previously showed the variation of the CO to H_2 conversion factor with column density. This factor is roughly constant for a 100 cm^{-3} cloud in a low UV field, providing the column density is $\gtrsim 4 \times 10^{21}$ cm^{-2}. This is comparable with the column density threshold used for our clump finding algorithms. Below these densities, or with a higher UV field, H_2 would be significantly underestimated from CO observations. However, neither an accurate temperature or UV flux are known for the gas in these models, which for these calculations are kept constant.

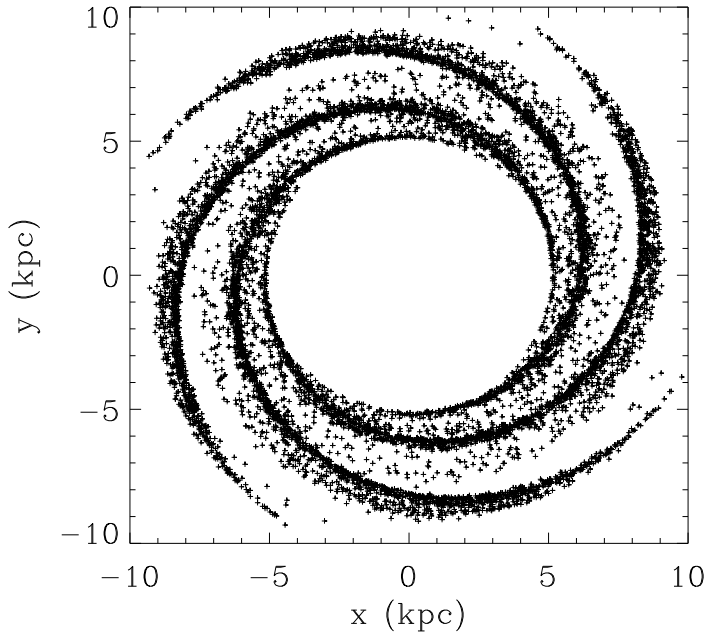

Figure 6.11: The distribution of clumps across the disk is displayed for the multi-phase simulation, using CF1 after 100 Myr.

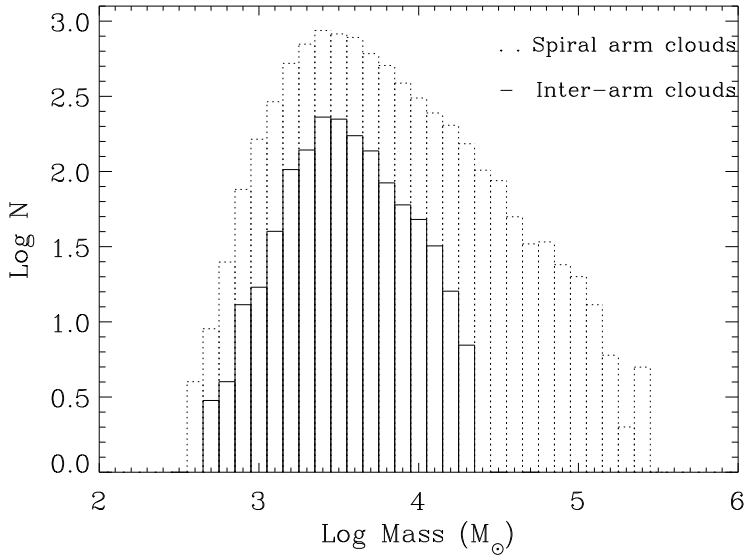

Figure 6.12: The clump mass spectrum is shown for the clumps from the multi-phase simulation. The clumps are located in the spiral arms (dotted) or the interarm regions (solid).

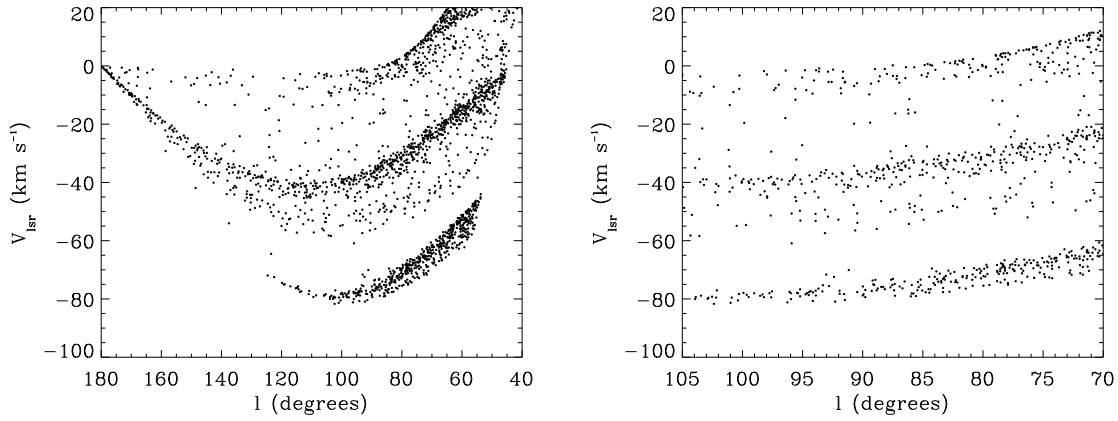

Figure 6.13: Figures showing V_{lsr} plotted against galactic longitude for molecular clouds from the multi-phase simulation.

Figure 6.13 lastly shows observational style plots comparable to Figures 5.12 and 5.13, for the multi-phase simulation. There are clearly more clouds between the spiral arms, as expected from the observed data shown in Chapter 5.

6.3 Summary

The simulations of a multi-phase medium subject to a spiral potential show that including hot gas in addition to cold significantly increases the amount of molecular gas in the disk. After 100 Myr, 1/4 of the cold gas is molecular, approximately double that of corresponding single phase calculations. This fraction increases with time during the simulation. The increase in H_2 is most striking in the interarm regions, with molecular clouds surviving into the interarm regions without being destroyed by photodissociation, although this neglects heating and cooling, and feedback. The spiral arm H_2 densities increase to values comparable with average GMC densities, whilst the typical interarm densities are similar to those expected from HISA observations, and are mostly too low for CO detection. For the whole disk, approximately 1/7 of the molecular clouds lie in the interarm regions, but this ratio decreases with radius as the separation of the spiral arms increases. The multi-phase simulations also show more structure in the cold gas, with smaller clumps present compared to the single phase calculations. Consequently the mass power spectrum is steeper for the multi-phase clouds, although the value of the exponent is found to depend on the clump-finding method.

The main factor which will affect these results is the inclusion of feedback, particularly in determining how much molecular gas is retained in the ISM following star formation. This may lead to less interarm molecular gas, but would also introduce the possibility of triggered molecular cloud formation in the interarm regions. Furthermore heating and cooling of the different phases are not included, rather a fixed composition of the ISM is assumed which approximately agrees with observations and previous simulations (Wada & Norman, 2001; Piontek & Ostriker, 2005; Audit & Hennebelle, 2005).

CHAPTER 7

Conclusions and Future Work

7.1 Conclusions

This thesis has investigated the formation of molecular clouds in spiral galaxies through numerical simulations. The results presented show the effects of spiral shocks on the gas dynamics over local (Chapter 3) and galactic scales (Chapters 4,5,6). The global simulations effectively test the hypothesis put forward by Roberts that spiral shocks trigger star formation. These simulations show not only that spiral shocks induce high densities in the gas, but they also play an active role in organising structure in the spiral arms. When the gas is cold, the interaction of the gas during the spiral arm passage leads to discretised clouds, without requiring gravitational or magnetic instabilities. The gas forms clouds which attain densities comparable with observed GMCs. With the inclusion of self gravity, localised regions will collapse to form stars. Chapter 5 showed that the gas must be cold in order for the shock to be dense enough for molecular hydrogen to form, supporting the scenario suggested by Pringle et al. (2001) that molecular clouds form from cold atomic or molecular gas. This simple model, where clouds form by the dynamics of the gas and the spiral potential can explain many of the observed properties of molecular clouds in spiral galaxies.

Firstly, the gas dynamics in the spiral potential evidently results in the formation of molecular clouds in the spiral arms, where most star formation is known to take place. In fact for the single phase calculations it is difficult to account for molecular clouds in the interarm regions, where there is very little molecular gas and no molecular clouds. This is because the molecular clouds are destroyed by photodissociation as they leave the spiral arms. Chapter 6 shows that for a multiphase medium, the cold gas is confined to higher densities by the pressure of the hot phase. There is much more molecular gas in the interarm regions and some molecular clouds. The ratio of interarm to spiral arm molecular clouds is comparable with those discussed in Chapter 1 and naturally decreases with radius as the spiral arms become further apart. Two caveats with these results are that neither feedback or heating and cooling of the gas are included. However previous simulations (Wada & Norman, 2001; Audit & Hennebelle, 2005; Piontek & Ostriker, 2005) show that a stable distribution of hot and cold gas is maintained in the ISM, with similar proportions to those assumed in Chapter 6.

The morphology of the molecular clouds, as shown in the global simulations, are

highly irregular and structured, similar to observations of molecular clouds. This structure is enhanced further in the multi-phase simulations. The morphology of the clouds is thus dependent on the temperature of the components of the ISM. The amount of molecular hydrogen in these simulations further depends on the mass of the disk, and the photodissociation rate. The masses of the clouds from the single and multi-phase distributions were shown in Chapter 6. The cloud mass spectra are consistent with observations. A physical basis for the form of the mass spectrum has not been explored though, but may correspond to models of cloud coagulation (Field, 1965; Silk & Takahashi, 1979; Hausman, 1982; Lejeune & Bastien, 1986; Das & Jog, 1996). The maximum cloud mass from these results is $\sim 6 \times 10^5$ $M_\odot$, less than typically found in galaxies. The disk mass can be increased, but self gravity and/or higher resolution simulations may be required to produce the highest (10^7 $M_\odot$) mass GMCs.

The analysis of Chapter 3 shows that spiral shocks can induce a velocity dispersion size-scale dependence in the ISM. The form of the velocity dispersion relation is interpreted in terms of mass loading, i.e. the amount of mass entering the shock at different densities, and is found to depend on the filling factor of the gas. The velocity dispersion relation was calculated analytically for simple gas distributions, and determined numerically for more complicated distributions. For distributions comparable to the ISM, the velocity dispersion scales with size in a similar way to the observed $\sigma \propto r^{0.5}$ law. The galactic simulations further reveal a large increase in the velocity dispersion in the gas in the spiral shock. This mechanism can therefore explain the supersonic velocities in molecular clouds, and unlike supernovae, is also applicable in regions without massive star formation. The velocities are induced in the clouds as they form, and with the current viewpoint that molecular clouds are short-lived (Elmegreen, 2000; Hartmann et al., 2001; Pringle et al., 2001), there is no need for the velocities to be sustained over more than several Myr. However, the possibility of inducing such motions in the other components of the ISM, which are also believed to be turbulent, has not been investigated. It is also unclear whether the model is relevant for galaxies e.g. the LMC, without spiral arms, which also show turbulence. These galaxies may exhibit large scale motions which would also incur shocks, and the analysis of Chapter 3 would still be relevant where supernovae shock waves interact with the ISM.

In addition to the formation and properties of molecular clouds, these simulations can also explain the development of interarm structures. Spurs, a common feature of spiral galaxies, are prominent in the cold gas simulations. The formation of spurs are a direct consequence of the shearing of the spiral arm clouds. The conditions for their formation are thus the same as those for the molecular clouds, that the gas is cold ($\leq$ 1000 K) and clumpy. The degree of structure revealed here, both in the spiral arms and in the form of spurs, has not been shown in previous simulations. This is due to the lower temperatures used, and the higher resolution of the simulations.

7.2 Future Work

The results shown in this thesis represent one of the first attempts to numerically model the formation of molecular clouds in spiral galaxies. This is potentially the start of an

extensive area of research. There are essentially 3 ways to further investigate molecular cloud formation numerically:

Additional physics

The simulations described include a very limited degree of physics. Self gravity, magnetic fields, thermal processes and feedback from star formation have so far been neglected. Self gravity is readily incorporated into the SPH code and some simulations with self gravity have been performed. When the Toomre criterion is satisfied, gas reaches sufficient densities in the spiral arms for gravitational collapse. The disadvantage with including self gravity is that the calculations become computationally expensive even with the addition of sink particles. Hence it is difficult to model multiple passages of gas through the spiral arms. Simulations have been carried out with self gravity, where the gas is stable against gravitational collapse, but the large scale structure of the galaxy does not change significantly (Figure 7.1) (Gittins (2004) also finds that self gravity has a negligible effect on the disk in SPH simulations). The addition of self gravity may be most important for modelling local regions or galaxies which are not dominated by spiral density waves..

The influence of magnetic fields on molecular cloud formation is not well understood, although as discussed in Chapter 1, Parker instabilities have long been proposed to explain their formation. The recent addition of magnetic fields in SPH (Price & Monaghan, 2005) will allow this problem to be further addressed. Previous grid code simulations (Kim et al., 2002; Shetty & Ostriker, 2006) show density perturbations produced by magnetic and gravitational instabilities in spiral shocks. Fragmentation of the spiral arms to form clouds is much less extensive than for the simulations shown here, so presumably cooling instabilities would also be required (they take a gas temperature of 10^4 K). The density perturbations are sufficient though to produce spurs which are not prominent in their purely hydrodynamical simulations (Shetty & Ostriker, 2006).

One of the potential problems with the results of this thesis is the initial conditions assumed, particularly for the single phase results. For molecular gas to form, the gas needs to be cold. Implicitly, it has been assumed either that there is a reservoir of cold hydrogen available in the ISM, or that cooling of the gas at higher densities in the spiral arms is nearly instantaneous (as suggested by Glover & Mac Low 2006a). For the latter, self gravity may also be required for gas to reach sufficient densities to cool effectively. Observationally, there appears to be a substantial fraction of the mass in the ISM in cold HI. Cold HI is often already associated with molecular hydrogen (i.e. on the periphery of or forming molecular clouds), but is unclear how much is distributed elsewhere. The results from Chapter 6, which are more applicable to modelling the ISM, show that pressure from the hot phase confines the cold clumps and increases the amount of molecular hydrogen. Numerical simulations are needed to verify whether this distribution of hot and cold gas is stable with heating and cooling. The location of the shock (Chapter 4) may constrain the thermal properties of gas entering the spiral arms.

The distribution of the ISM and cooling and heating processes are further regulated by feedback. The lifetimes of molecular clouds are thought to be less than ~ 30 Myr (Bash et al., 1977; Blitz & Shu, 1980) and potentially < 5 Myr (Hartmann et al., 2001), before dispersal by supernovae in high mass star-forming regions, or outflows from low-mass stars. However, as mentioned in Chapter 1, supernovae could also compress the ISM

to form new molecular clouds. The degree of massive star formation will also determine the local photodissociation rate, rather than using a fixed global value.

Different types of galaxy

These simulations are limited to grand design type galaxies. Furthermore the application of a time-independent spiral potential produces a spiral pattern more regular and symmetric than observed in any actual galaxies, save perhaps the central regions of M51. An alternative is to use an N-body calculation of the evolution of a spiral galaxy, and extract a time-dependent potential. An image from an SPH simulation, which uses a galactic potential from an N-body calculation by Sellwood & Carlberg (1984) is shown in Figure 7.2. The disk still shows fairly long, regular spiral arms, but the structure is more typical of spiral galaxies. To be more consistent, both stars and gas should be included. Gravitational instabilities will produce spiral arms in the stellar distribution which then influence the gas dynamics. Simulations with both a stellar and gaseous component have been performed for flocculent spiral galaxies (Elmegreen & Thomasson, 1993; Li et al., 2005). These results show that rate of star formation increases as the Q parameter for the disk decreases.

There are many more dwarf and irregular galaxies than spiral galaxies, where molecular cloud formation is likely to be determined primarily by gravitational instabilities and possibly triggering by multiple supernovae (most evident for the LMC). Wada et al. (2000) model the LMC, finding the structure and dynamics dominated by gravitational and thermal instabilities. Recently, similar simulations to those presented here have been performed to investigate dwarf galaxies (Pelupessy et al., 2006). The molecular clouds in the dwarf galaxy simulations appear to be distributed randomly, and the molecular gas fractions tend to be lower than for the spiral arm molecular clouds shown here, except at high metallicities.

Higher resolution simulations

Chapter 6 included a discussion of the properties of molecular clouds determined from these simulations. However, these results were limited by the resolution of the clouds. With a mass resolution of ~ 100 $M_\odot$, many clouds contain less than 100 particles. Higher resolution simulations will allow a more accurate comparison with the observed velocity dispersion relation and cloud mass spectra. Furthermore, they will give a good indication of whether GMCs are likely to be unbound or bound. Figure 7.3 shows a section of the 50 K simulation which has been re-run at 80 times the resolution. Taking a section of a global model and repeating at higher resolution in this way will enable a more detailed analysis of the internal properties of molecular clouds, such as their density profiles.

Finally, the results of these simulations can be compared with the observational data described in Chapter 1. The comparisons made so far have neglected the fact that the observational results are determined from measurements of CO rather than H_2. Incorporating CO formation into the simulations is likely to be useful in this respect.

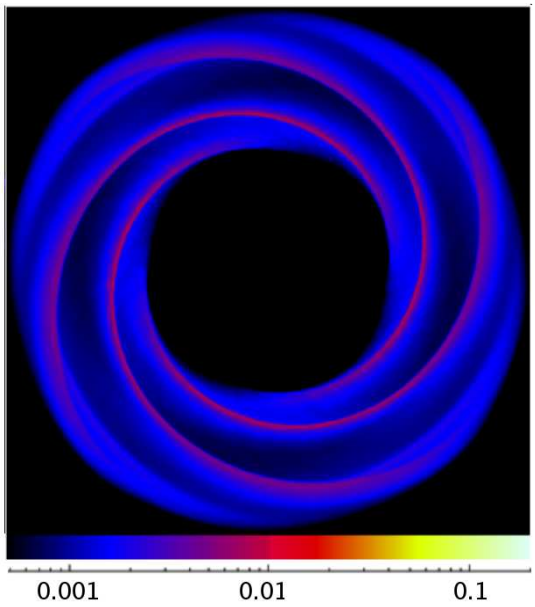

Figure 7.1: The column density plot (g cm^{-2}) shows a disk of 2×10^9 $M_\odot$, with gas temperature 10^4 K, where self gravity is included. The structure is very similar to Figure 4.4d. For a disk mass of 5×10^9 $M_\odot$, (surface density of 20 $M_\odot$ pc^{-2}), the gas collapses rapidly in the spiral arms.

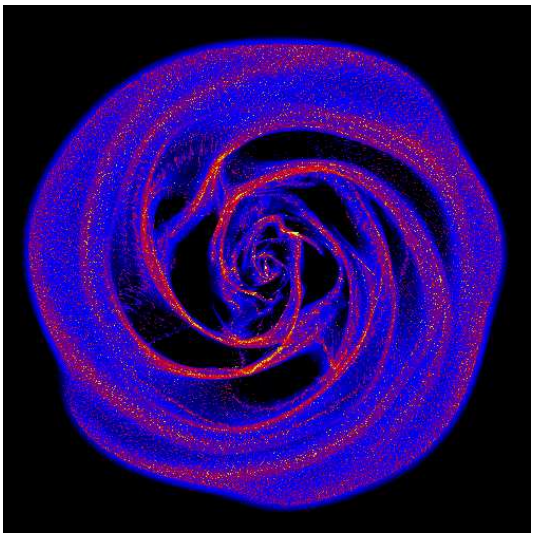

Figure 7.2: The spiral structure is displayed for a disk where a time-dependent spiral potential taken from an N-body calculation has been applied. The gas is distributed in a multiphase medium, with 50% at 100 K and 50% at 10^4 K. The scaling is the same as Figure 4.4.

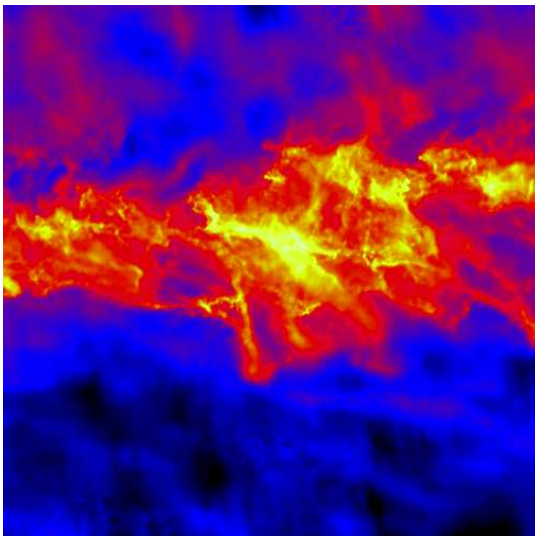

Figure 7.3: A section of spiral arm (300 pc x 300 pc) is shown from the 50 K simulation, where part of the disk has been re-run with 80 times the resolution of the original calculation. The scaling is the same as for Figure 4.4

Aalto S., Huettemeister S., Das M., Wall W. F., 1998, in IAU Symp. 184: The Central Regions of the Galaxy and Galaxies, Sofue Y., ed., pp. 251–+

Aalto S., Hüttemeister S., Scoville N. Z., Thaddeus P., 1999, ApJ, 522, 165

Aannestad P. A., 1973, ApJS, 25, 223

Adler D. S., Lo K. Y., Wright M. C. H., Rydbeck G., Plante R. L., Allen R. J., 1992, ApJ, 392, 497

Allen R. J., 2004, in Penetrating Bars Through Masks of Cosmic Dust, Block D. L., Puerari I., Freeman K. C., Groess R., Block E. K., eds., pp. 731–+

Allen R. J., Heaton H. I., Kaufman M. J., 2004, ApJ, 608, 314

Allen R. J., Lequeux J., 1993, ApJL, 410, L15

Alves J., Lada C. J., Lada E. A., Kenyon S. J., Phelps R., 1998, ApJ, 506, 292

Alves J. F., Lada C. J., Lada E. A., 2001, Nature, 409, 159

Audit E., Hennebelle P., 2005, A&A, 433, 1

Baade W., Gaposchkin C. H. P., 1963, Evolution of stars and galaxies. Cambridge, Harvard University Press, 1963.

Balbus S. A., 1988, ApJ, 324, 60

Balbus S. A., Cowie L. L., 1985, ApJ, 297, 61

Ballesteros-Paredes J., 2004, Ap&SS, 289, 243

Ballesteros-Paredes J., Hartmann L., Vázquez-Semadeni E., 1999, ApJ, 527, 285

Ballesteros-Paredes J., Vazquez-Semadeni E., 1995, in Revista Mexicana de Astronomia y Astrofisica Conference Series, Pena M., Kurtz S., eds., pp. 105–+

Bash F. N., Green E., Peters III W. L., 1977, ApJ, 217, 464

Bate M. R., 1985, Ph.D. Thesis, Cambridge University

—, 1998, ApJL, 508, L95

Bate M. R., Bonnell I. A., Bromm V., 2003, MNRAS, 339, 577

Benz W., 1990, in Numerical Modelling of Nonlinear Stellar Pulsations Problems and Prospects, pp. 269–+

Benz W., Cameron A. G. W., Press W. H., Bowers R. L., 1990, ApJ, 348, 647

Bergin E. A., Hartmann L. W., Raymond J. C., Ballesteros-Paredes J., 2004, ApJ, 612, 921

Binney J., Tremaine S., 1987, Galactic dynamics. Princeton, NJ, Princeton University Press, 1987, 747 p.

Blitz L., 1993, in Protostars and Planets III, Levy E. H., Lunine J. I., eds., pp. 125–161

Blitz L., Bazell D., Desert F. X., 1990, ApJL, 352, L13

Blitz L., Fukui Y., Kawamura A., Leroy A., Mizuno N., Rosolowsky E., 2006, ArXiv Astrophysics e-prints

Blitz L., Rosolowsky E., 2004, ApJL, 612, L29

Blitz L., Shu F. H., 1980, ApJ, 238, 148

Blitz L., Stark A. A., 1986, ApJL, 300, L89

Blitz L., Williams J. P., 1999, in NATO ASIC Proc. 540: The Origin of Stars and Planetary Systems, Lada C. J., Kylafis N. D., eds., pp. 3–+

Block D. L., Elmegreen B. G., Wainscoat R. J., 1996, Nature, 381, 674

Bloemen J. B. G. M., Caraveo P. A., Hermsen W., Lebrun F., Maddalena R. J., Strong A. W., Thaddeus P., 1984, A&A, 139, 37

Boissier S., Prantzos N., Boselli A., Gavazzi G., 2003, MNRAS, 346, 1215

Bok B. J., 1956, AJ, 61, 309

—, 1959, The Observatory, 79, 58

Boldyrev S., 2002, ApJ, 569, 841

Boldyrev S., Nordlund Å., Padoan P., 2002, ApJ, 573, 678

Bonnell I. A., Dobbs C. L., Robitaille T. P., Pringle J. E., 2006, MNRAS, 365, 37

Bottema R., 2003, MNRAS, 344, 358

Boulares A., Cox D. P., 1990, ApJ, 365, 544

Bronfman L., Casassus S., May J., Nyman L.-Å., 2000, A&A, 358, 521

Brouillet N., Baudry A., Combes F., Kaufman M., Bash F., 1991, A&A, 242, 35

Brouillet N., Kaufman M., Combes F., Baudry A., Bash F., 1998, A&A, 333, 92

Brunt C. M., 2003, ApJ, 583, 280

Byrd G. G., 1983, ApJ, 264, 464

Caldwell J. A. R., Ostriker J. P., 1981, ApJ, 251, 61

Cazaux S., Tielens A. G. G. M., 2002, ApJL, 575, L29

—, 2004, ApJ, 604, 222

Cedrés B., Cepa J., Tomita A., 2005, ApJ, 634, 1043

Cepa J., Beckman J. E., 1990, ApJ, 349, 497

Chakrabarti S., Laughlin G., Shu F. H., 2003, ApJ, 596, 220

Clark P. C., Bonnell I. A., 2004, MNRAS, 347, L36

—, 2006, MNRAS, 368, 1787

Clarke C., Gittins D., 2006, MNRAS, 371, 530

Cohen R. S., Dame T. M., Thaddeus P., 1986, ApJS, 60, 695

Cowie L. L., 1980, ApJ, 236, 868

—, 1981, ApJ, 245, 66

Cox D. P., 2005, ARA&A, 43, 337

Cox D. P., Gómez G. C., 2002, ApJS, 142, 261

Dame T. M., 1993, in AIP Conf. Proc. 278: Back to the Galaxy, Holt S. S., Verter F., eds., pp. 267–278

Dame T. M., Elmegreen B. G., Cohen R. S., Thaddeus P., 1986, ApJ, 305, 892

Dame T. M., Hartmann D., Thaddeus P., 2001, ApJ, 547, 792

Das M., Jog C. J., 1996, ApJ, 462, 309

de Avillez M. A., Breitschwerdt D., 2005, A&A, 436, 585

Deharveng L., Zavagno A., Salas L., Porras A., Caplan J., Cruz-González I., 2003, A&A, 399, 1135

Dib S., Bell E., Burkert A., 2006, ApJ, 638, 797

Dickey J. M., Lockman F. J., 1990, ARA&A, 28, 215

Dickman R. L., 1978a, AJ, 83, 363

—, 1978b, ApJS, 37, 407

Digel S. W., Lyder D. A., Philbrick A. J., Puche D., Thaddeus P., 1996, ApJ, 458, 561

Dobbs C. L., Bonnell I. A., Clark P. C., 2005, MNRAS, 360, 2

Dopita M. A., Mathewson D. S., Ford V. L., 1985, ApJ, 297, 599

Draine B. T., Bertoldi F., 1996, ApJ, 468, 269

Dwarkadas V. V., Balbus S. A., 1996, ApJ, 467, 87

Efremov Y. N., Elmegreen B. G., 1998, MNRAS, 299, 643

Elmegreen B. G., 1979, ApJ, 231, 372

—, 1982, ApJ, 253, 655

—, 1989, ApJ, 344, 306

—, 1990, in Blitz, L., ed., ASP Conf. Ser. 12: The Evolution of the Interstellar Medium. San Fracisco, p247.

—, 1994a, ApJ, 427, 384

—, 1994b, ApJ, 433, 39

—, 1996, in IAU Symp. 169: Unsolved Problems of the Milky Way, Blitz L., Teuben P. J., eds., pp. 551–+

—, 1997, ApJ, 477, 196

—, 1998, in ASP Conf. Ser. 148: Origins, Woodward C. E., Shull J. M., Thronson Jr. H. A., eds., pp. 150–+

—, 2000, ApJ, 530, 277

—, 2002, ApJ, 577, 206

Elmegreen B. G., Elmegreen D. M., 1983, MNRAS, 203, 31

—, 1986, ApJ, 311, 554

Elmegreen B. G., Elmegreen D. M., Leitner S. N., 2003, ApJ, 590, 271

Elmegreen B. G., Lada C. J., 1977, ApJ, 214, 725

Elmegreen B. G., Scalo J., 2004, ARA&A, 42, 211

Elmegreen B. G., Thomasson M., 1993, A&A, 272, 37

Elmegreen D. M., 1980, ApJ, 242, 528

Elmegreen D. M., Elmegreen B. G., 1982, MNRAS, 201, 1021

Encrenaz P. J., Falgarone E., Lucas R., 1975, A&A, 44, 73

Engargiola G., Plambeck R. L., Rosolowsky E., Blitz L., 2003, ApJS, 149, 343

Falgarone E., Hily-Blant P., Pineau Des Forêts G., 2005, in The Dusty and Molecular Universe: A Prelude to Herschel and ALMA, Wilson A., ed., pp. 75–80

Falgarone E., Phillips T. G., 1990, ApJ, 359, 344

Falgarone E., Phillips T. G., Walker C. K., 1991, ApJ, 378, 186

Field G. B., 1965, ApJ, 142, 531

Field G. B., Hutchins J., 1968, ApJ, 153, 737

Field G. B., Saslaw W. C., 1965, ApJ, 142, 568

Fuller G. A., Myers P. C., 1992, ApJ, 384, 523

Garcia-Burillo S., Guelin M., Cernicharo J., 1993, A&A, 274, 123

Gerola H., Seiden P. E., 1978, ApJ, 223, 129

Gibson S. J., Taylor A. R., Higgs L. A., Brunt C. M., Dewdney P. E., 2005, ApJ, 626, 195

Gibson S. J., Taylor A. R., Higgs L. A., Dewdney P. E., 2000, ApJ, 540, 851

Gingold R. A., Monaghan J. J., 1977, MNRAS, 181, 375

Gittins D. M., 2004, Ph.D. Thesis, Cambridge University

Gittins D. M., Clarke C. J., 2004, MNRAS, 349, 909

Gittins D. M., Clarke C. J., Bate M. R., 2003, MNRAS, 340, 841

Glover S. C. O., Mac Low M. ., 2006a, ArXiv Astrophysics e-prints

—, 2006b, ArXiv Astrophysics e-prints

Goldreich P., Lynden-Bell D., 1965, MNRAS, 130, 125

Gómez G. C., Cox D. P., 2002, ApJ, 580, 235

Goodman A. A., Barranco J. A., Wilner D. J., Heyer M. H., 1998, ApJ, 504, 223

Gould R. J., Salpeter E. E., 1963, ApJ, 138, 393

Grabelsky D. A., Cohen R. S., Bronfman L., Thaddeus P., 1988, ApJ, 331, 181

Grabelsky D. A., Cohen R. S., Bronfman L., Thaddeus P., May J., 1987, ApJ, 315, 122

Greaves J. S., Williams P. G., 1994, A&A, 290, 259

Grosbøl P., Dottori H., Gredel R., 2006, A&A, 453, L25

Hanawa T., Matsumoto R., Shibata K., 1992, ApJL, 393, L71

Handbury M. J., Simons S., Williams I. P., 1977, A&A, 61, 443

Hartmann L., Ballesteros-Paredes J., Bergin E. A., 2001, ApJ, 562, 852

Hausman M. A., 1982, ApJ, 261, 532

Hayashi M., Kobayashi H., Hasegawa T., 1989, ApJ, 340, 298

Heitsch F., Burkert A., Hartmann L. W., Slyz A. D., Devriendt J. E. G., 2005, ApJL, 633, L113

Heyer M. H., Brunt C., Snell R. L., Howe J. E., Schloerb F. P., Carpenter J. M., 1998, ApJS, 115, 241

Heyer M. H., Brunt C. M., 2004, ApJL, 615, L45

Heyer M. H., Carpenter J. M., Snell R. L., 2001, ApJ, 551, 852

Heyer M. H., Corbelli E., Schneider S. E., Young J. S., 2004, ApJ, 602, 723

Heyer M. H., Schloerb F. P., 1997, ApJ, 475, 173

Heyer M. H., Terebey S., 1998, ApJ, 502, 265

Hollenbach D., McKee C. F., 1979, ApJS, 41, 555

Hollenbach D. J., Werner M. W., Salpeter E. E., 1971, ApJ, 163, 165

Jackson J. M., Rathborne J. M., Shah R. Y., Simon R., Bania T. M., Clemens D. P., Chambers E. T., Johnson A. M., Dormody M., Lavoie R., Heyer M. H., 2006, ApJS, 163, 145

Kaufman M., Bash F. N., Hine B., Rots A. H., Elmegreen D. M., Hodge P. W., 1989, ApJ, 345, 674

Kaufman M. J., Wolfire M. G., Hollenbach D. J., Luhman M. L., 1999, ApJ, 527, 795

Kavars D. W., Dickey J. M., McClure-Griffiths N. M., Gaensler B. M., Green A. J., 2005, ApJ, 626, 887

Kawamura A., Onishi T., Yonekura Y., Dobashi K., Mizuno A., Ogawa H., Fukui Y., 1998, ApJS, 117, 387

Kennicutt Jr. R. C., 1989, ApJ, 344, 685

Kim J., Ryu D., Jones T. W., 2001, ApJ, 557, 464

Kim W., Ostriker E. C., 2002, ApJ, 570, 132

Kim W.-T., Ostriker E. C., 2006, ApJ, 646, 213

Kim W.-T., Ostriker E. C., Stone J. M., 2002, ApJ, 581, 1080

Kimura T., Tosa M., 1996, A&A, 308, 979

Klaassen P. D., Plume R., Gibson S. J., Taylor A. R., Brunt C. M., 2005, ApJ, 631, 1001

Klessen R. S., Burkert A., 2001, ApJ, 549, 386

Koda J., Sawada T., Hasegawa T., Scoville N. Z., 2006, ApJ, 638, 191

Kornreich P., Scalo J., 2000, ApJ, 531, 366

Kothes R., Reich W., Foster T., Byun D.-Y., 2003, ApJ, 588, 852

Koyama H., Inutsuka S., 2000, ApJ, 532, 980

Krumholz M. R., McKee C. F., 2005, ApJ, 630, 250

Kwan J., 1979, ApJ, 229, 567

La Vigne M. A., Vogel S. N., Ostriker E. C., 2006, ArXiv Astrophysics e-prints

Lada C. J., Alves J. F., Lombardi M. F., 2006, in press

Lada C. J., Lada E. A., Clemens D. P., Bally J., 1994, ApJ, 429, 694

Larson R. B., 1981, MNRAS, 194, 809

Lattanzio J. C., Monaghan J. J., Pongracic H., Schwarz M. P., 1985, MNRAS, 215, 125

Lee Y., Stark A. A., Kim H.-G., Moon D.-S., 2001, ApJS, 136, 137

Lejeune C., Bastien P., 1986, ApJ, 309, 167

Lequeux J., Allen R. J., Guilloteau S., 1993, A&A, 280, L23

Li Y., Mac Low M.-M., Klessen R. S., 2005, ApJ, 626, 823

Lin C. C., Shu F. H., 1964, ApJ, 140, 646

Lipshtat A., Biham O., 2005, MNRAS, 362, 666

Loinard L., Dame T. M., Heyer M. H., Lequeux J., Thaddeus P., 1999, A&A, 351, 1087

Lombardi M., Alves J., Lada C. J., 2006, ArXiv Astrophysics e-prints

Lucy L. B., 1977, AJ, 82, 1013

Lundgren A. A., Wiklind T., Olofsson H., Rydbeck G., 2004, A&A, 413, 505

Lynds B. T., 1970, in IAU Symp. 38: The Spiral Structure of our Galaxy, pp. 26–+

Mac Low M.-M., Klessen R. S., 2004, Reviews of Modern Physics, 76, 125

Maddalena R. J., Thaddeus P., 1985, ApJ, 294, 231

Martin C. L., Kennicutt Jr. R. C., 2001, ApJ, 555, 301

McCray R., Kafatos M., 1987, ApJ, 317, 190

McKee C. F., Ostriker J. P., 1977, ApJ, 218, 148

Merrifield M. R., Rand R. J., Meidt S. E., 2006, MNRAS, 366, L17

Miniati F., Jones T. W., Ferrara A., Ryu D., 1997, ApJ, 491, 216

Mishurov Y. N., Zenina I. A., 1999, A&A, 341, 81

Monaghan J. J., 1982, SIAM. J. Sci. Statist. Comput., 3, 422

—, 1989, Journal of Computational Physics, 82, 1

—, 1992, ARA&A, 30, 543

—, 2002, MNRAS, 335, 843

Monaghan J. J., Gingold R. A., 1983, J. Comput. Phys., 52, 374

Monaghan J. J., Lattanzio J. C., 1985, A&A, 149, 135

Morris J. P., Monaghan J. J., 1997, J. Comput. Phys., 136, 41

Mouschovias T. C., Shu F. H., Woodward P. R., 1974, A&A, 33, 73

Mueller M. W., Arnett W. D., 1976, ApJ, 210, 670

Myers P. C., 1983, ApJ, 270, 105

Normandeau M., 1999, AJ, 117, 2440

Oey M. S., Massey P., 1995, ApJ, 452, 210

Oey M. S., Watson A. M., Kern K., Walth G. L., 2005, AJ, 129, 393

Oort J. H., 1954, Bull. Astr. Neth., 12, 177

Ossenkopf V., Mac Low M.-M., 2002, A&A, 390, 307

Parker E. N., 1966, ApJ, 145, 811

Parravano A., 1987, A&A, 172, 280

Passot T., Pouquet A., Woodward P., 1988, A&A, 197, 228

Passot T., Vazquez-Semadeni E., Pouquet A., 1995, ApJ, 455, 536

Patsis P. A., Grosbol P., Hiotelis N., 1997, A&A, 323, 762

Patsis P. A., Hiotelis N., Contopoulos G., Grosbol P., 1994, A&A, 286, 46

Pelupessy F. I., Papadopoulos P. P., van der Werf P., 2006, ApJ, 645, 1024

Perault M., Falgarone E., Puget J. L., 1985, A&A, 152, 371

Piontek R. A., Ostriker E. C., 2005, ApJ, 629, 849

Pirronello V., Liu C., Roser J. E., Vidali G., 1999, A&A, 344, 681

Plambeck R. L., Williams D. R. W., 1979, ApJL, 227, L43

Price D. J., Monaghan J. J., 2004, Ap&SS, 292, 279

—, 2005, MNRAS, 364, 384

Pringle J. E., Allen R. J., Lubow S. H., 2001, MNRAS, 327, 663

Rand R. J., Kulkarni S. R., 1990, ApJL, 349, L43

Reuter H.-P., Sievers A. W., Pohl M., Lesch H., Wielebinski R., 1996, A&A, 306, 721

Roberts W. W., 1969, ApJ, 158, 123

Roberts Jr. W. W., Hausman M. A., 1984, ApJ, 277, 744

Roberts Jr. W. W., Roberts M. S., Shu F. H., 1975, ApJ, 196, 381

Romanishin W., 1985, ApJ, 289, 570

Rosen A., Bregman J. N., 1995, ApJ, 440, 634

Rots A. H., 1975, A&A, 45, 43

Russell W. S., Roberts W. W., 1992, ApJ, 398, 94

Scalo J., Vazquez-Semadeni E., Chappell D., Passot T., 1998, ApJ, 504, 835

Scoville N. Z., Hersh K., 1979, ApJ, 229, 578

Scoville N. Z., Polletta M., Ewald S., Stolovy S. R., Thompson R., Rieke M., 2001, AJ, 122, 3017

Scoville N. Z., Sanders D. B., Clemens D. P., 1986, ApJL, 310, L77

Scoville N. Z., Solomon P. M., 1973, ApJ, 180, 31

Seigar M. S., Block D. L., Puerari I., Chorney N. E., James P. A., 2005, MNRAS, 359, 1065

Seigar M. S., James P. A., 2002, MNRAS, 337, 1113

Sellwood J. A., Balbus S. A., 1999, ApJ, 511, 660

Sellwood J. A., Carlberg R. G., 1984, ApJ, 282, 61

She Z.-S., Leveque E., 1994, Physical Review Letters, 72, 336

Shetty R., Ostriker E. C., 2006, ApJ, 647, 997

Shu F. H., 1974, A&A, 33, 55

Shu F. H., Milione V., Gebel W., Yuan C., Goldsmith D. W., Roberts W. W., 1972, ApJ, 173, 557

Shu F. H., Milione V., Roberts W. W., 1973, ApJ, 183, 819

Silk J., Takahashi T., 1979, ApJ, 229, 242

Slyz A. D., Kranz T., Rix H.-W., 2003, MNRAS, 346, 1162

Solomon P. M., Rivolo A. R., 1989, ApJ, 339, 919

Solomon P. M., Rivolo A. R., Barrett J., Yahil A., 1987, ApJ, 319, 730

Solomon P. M., Sanders D. B., Rivolo A. R., 1985, ApJL, 292, L19

Solomon P. M., Scoville N. Z., Penzias A. A., Wilson R. W., Jefferts K. B., 1972, ApJ, 178, 125

Stamatellos D., Whitworth A. P., 2005, A&A, 439, 153

Stark A. A., Elmegreen B. G., Chance D., 1987, ApJ, 322, 64

Stark A. A., Lee Y., 2006, ApJL, 641, L113

Stone J. M., Ostriker E. C., Gammie C. F., 1998, ApJL, 508, L99

Strong A. W., Bloemen J. B. G. M., Dame T. M., Grenier I. A., Hermsen W., Lebrun F., Nyman L.-A., Pollock A. M. T., Thaddeus P., 1988, A&A, 207, 1

Taff L. G., Savedoff M. P., 1972, MNRAS, 160, 89

Tasker E. J., Bryan G. L., 2006, ApJ, 641, 878

Taylor A. R., Gibson S. J., Peracaula M., Martin P. G., Landecker T. L., Brunt C. M., Dewdney P. E., Dougherty S. M., Gray A. D., Higgs L. A., Kerton C. R., Knee L. B. G., Kothes R., Purton C. R., Uyaniker B., Wallace B. J., Willis A. G., Durand D., 2003, AJ, 125, 3145

Tenorio-Tagle G., Bodenheimer P., 1988, ARA&A, 26, 145

Testi L., Sargent A. I., 1998, ApJL, 508, L91

Thornley M. D., Mundy L. G., 1997, ApJ, 484, 202

Tilanus R. P. J., Allen R. J., 1989, ApJL, 339, L57

—, 1991, A&A, 244, 8

—, 1993, A&A, 274, 707

Toomre A., 1964, ApJ, 139, 1217

Tully R. B., 1974, ApJS, 27, 449

Vallée J. P., 2005, AJ, 130, 569

van Dishoeck E. F., Black J. H., 1988, ApJ, 334, 771

Vázquez-Semadeni E., 2002, in ASP Conf. Ser. 276: Seeing Through the Dust: The Detection of HI and the Exploration of the ISM in Galaxies, Taylor A. R., Landecker T. L., Willis A. G., eds., pp. 155–+

Vazquez-Semadeni E., Passot T., Pouquet A., 1995, ApJ, 441, 702

Viau S., Bastien P., Cha S.-H., 2006, ApJ, 639, 559

Vidali G., Roser J. E., Manicó G., Pirronello V., 2004, Journal of Geophysical Research (Planets), 109, 7

Visser H. C. D., 1980a, A&A, 88, 159

—, 1980b, A&A, 88, 149

Vogel S. N., Kulkarni S. R., Scoville N. Z., 1988, Nature, 334, 402

Wada K., Koda J., 2004, MNRAS, 349, 270

Wada K., Meurer G., Norman C. A., 2002, ApJ, 577, 197

Wada K., Norman C. A., 1999, ApJL, 516, L13

—, 2001, ApJ, 547, 172

Wada K., Spaans M., Kim S., 2000, ApJ, 540, 797

Weaver H. F., 1970, in IAU Symp. 39: Interstellar Gas Dynamics, pp. 22–+

Whitehouse S. C., Bate M. R., 2006, MNRAS, 367, 32

Whitehouse S. C., Bate M. S., 2004, MNRAS, 353, 1078

Whitworth A. P., Bhattal A. S., Chapman S. J., Disney M. J., Turner J. A., 1994, A&A, 290, 421

Williams J. P., Blitz L., McKee C. F., 2000, Protostars and Planets IV, 97

Williams J. P., Blitz L., Stark A. A., 1995, ApJ, 451, 252

Williams J. P., de Geus E. J., Blitz L., 1994, ApJ, 428, 693

Wolfire M. G., McKee C. F., Hollenbach D., Tielens A. G. G. M., 2003, ApJ, 587, 278

Wong T., Blitz L., 2002, ApJ, 569, 157

Woodward P. R., 1978, ARA&A, 16, 555

Yang J., Jiang Z., Wang M., Ju B., Wang H., 2002, ApJS, 141, 157

Yun J. L., Moreira M. C., Afonso J. M., Clemens D. P., 1999, AJ, 118, 990

Zel'dovich Y. B., Raizer Y. P., 1966, Physics of Shock Waves and High-Temperature Hydrodynamic Phenomena. Academic Press

Zhang X., Lee Y., Bolatto A., Stark A. A., 2001, ApJ, 553, 274

Zuckerman B., Evans II N. J., 1974, ApJL, 192, L149

Zweibel E. G., Kulsrud R. M., 1975, ApJ, 201, 63